Influence of Pulsed Heat Load on the Performance of Diamond Bragg Mirrors for an XFEL-Oscillator

Dissertation

zur Erlangung des Doktorgrades
an der Fakultät für Mathematik, Informatik und
Naturwissenschaften
Fachbereich Physik
der Universität Hamburg

vorgelegt von
Christoph Maag

Hamburg
2018

Gutachter/innen der Dissertation:	Prof. Dr. Jörg Roßbach Prof. Dr. Ralf Röhlsberger
Zusammensetzung der Prüfungskommission:	Prof. Dr. Robin Santra Prof. Dr. Jörg Roßbach Prof. Dr. Ralf Röhlsberger Prof. Dr. Wolfgang Hillert Dr. Harald Sinn
Vorsitzende/r der Prüfungskommission:	Prof. Dr. Robin Santra
Datum der Disputation:	03.08.2018
Vorsitzender Fach-Promotionsausschusses PHYSIK:	Prof. Dr. Wolfgang Hansen
Leiter des Fachbereichs PHYSIK:	Prof. Dr. Michael Potthoff
Dekan der Fakultät MIN:	Prof. Dr. Heinrich Graener

Abstract

In this thesis, different aspects of an x-ray free electron laser oscillator (XFELO) are considered. The focus, however, is clearly on the investigation of the influence of absorbed x-ray power on the Bragg reflection of diamond crystals. Due to its unique combination of superb thermo-mechanical and optical properties, diamond is the most promising material for high power x-ray Bragg mirrors as required to build an XFELO cavity. Because the Bragg reflection is sensitive to strain in the crystal structure, a numerical study is performed to obtain the strain field in a diamond crystal caused by the heat load expected to be deposited by a typical XFELO pulse. Furthermore, the effect of the strain in the diamond crystal on its Bragg reflectivity is studied as well. Due to the even more outstanding thermal conductivity and thermal expansion of diamond at cryogenic temperatures it appears favorable to operate the Bragg mirrors at those temperatures. However, at low temperatures and the spatial dimensions of an XFELO Bragg mirror, ballistic heat conduction effects, which are difficult to predict theoretically, set in. These ballistic heat conduction effects question the applicability of the classical heat conduction equation. For that reason a pump-probe experimental setup has been designed and realized, capable of simulating the heat load expected to be deposited by an XFELO pulse and measuring the resulting temperature decay. Additionally, by means of an appropriate data analysis, the validity of the classical heat equation and the hyperbolic heat equation at cryogenic temperatures is evaluated.

Zusammenfassung

In dieser Arbeit werden verschiedene Aspekte eines Röntgen-Freie-Elektronen-Laser-Oszillators (XFELO) betrachtet. Dabei liegt der Fokus jedoch klar auf der Untersuchung des Einflusses von absorbierter Röntgenstrahlung auf die Bragg-Reflexion von Diamantkristallen. Aufgrund der einzigartigen Kombination seiner hervorragenden thermo-mechanischen und optischen Eigenschaften ist Diamant das vielversprechendste Material für Hochleistungs-Bragg-Spiegel, wie sie zum Aufbau einer XFELO Kavität benötigt werden. Da die Bragg-Reflexion empfindlich auf Dehnungen der Kristallstruktur reagiert, wurde eine numerische Studie durchgeführt, um so das Dehnungsfeld innerhalb des Diamantkristalls zu erhalten, welches durch die Wärmelast verursacht wird, die erwartungsgemäß von einem typischen XFELO Puls deponiert wird. Außerdem wird die Auswirkung der Dehnung innerhalb des Kristalls auf die Bragg-Reflektivität untersucht. Aufgrund der sogar noch günstigeren thermischen Leitfähigkeit und thermischen Ausdehnung von Diamant bei kryogenen Temperaturen erscheint es vorteilhaft, die Bragg-Spiegel bei solchen Temperaturen zu betreiben. Bei niedrigen Temperaturen und den geringen räumlichen Ausmaßen der XFELO-Bragg-Spiegel treten jedoch ballistische Wärmeleitungseffekte auf, die theoretisch schwer vorhersagbar sind. Diese ballistischen Wärmeleitungseffekte stellen die Anwendbarkeit der klassischen Wärmeleitungsgleichung in Frage. Aus diesem Grund wird in dieser Arbeit die Entwicklung und Realisierung eines experimentellen Aufbaus beschrieben, mit dem die erwartete Wärmelast, die in einem XFELO- Spiegel deponiert wird, simuliert und der anschließende Abkühlvorgang gemessen werden kann. Zusätzlich wird anhand geeigneter Datenanalyse die Gültigkeit der klassischen Wärmeleitungsgleichung und der hyperbolischen Wärmeleitungsgleichung überprüft.

Contents

List of Figures

1 Introduction

Visible light interacting with matter is the predominant interaction whereby we perceive our environment. Even though the visible part of the electromagnetic spectrum is the most familiar for us, other ranges of this spectrum are also suitable for revealing information about nature. Since the electromagnetic waves in different wavelength ranges interact differently with matter, they can be utilized complementary. One important wavelength range is the x-ray regime. X-radiation has unique properties and is therefore widely used in science, industry, security and health care. The major application of x-rays, due to their ability to penetrate matter, is to image the inside of objects. Other important applications which are mainly used in science are x-ray spectroscopy and x-ray diffraction. With x-ray diffraction the structure of solids and molecules can be investigated on the atomic scale.

For scientific applications the major figure of merit of an x-ray source is the brilliance – a measure for the photon flux normalized to the solid angle of emission, the source size and the bandwidth. In order to increase the brilliance, accelerator based x-ray sources have been developed over more than half a century since the discovery of synchrotron radiation in 1946. Over that period, the brilliance of the synchrotron radiation sources could be increased by about 3 orders of magnitude per decade. About two decades ago, it became clear that Free-Electron Lasers[1] (FELs), which were invented by John Madey in 1971 [Madey, 1971], can be used as x-ray sources. With x-ray FELs (XFELs) the peak brilliance was increased by further eight orders of magnitude compared to storage ring facilities. The first soft x-ray FEL FLASH was built at DESY in Hamburg and started operation for users in 2005 [Ayvazyan et al., 2005]. In the hard x-ray regime, the Linear Coherent Light Source (LCLS) at Stanford was the first operational FEL, beginning in 2009 [Emma et al., 2010]. Both FELs are based on the SASE (self-amplified spontaneous emission) principle[2], which enables short pulses with a high peak brilliance and a high degree of spatial coherence [Kondratenko and Saldin, 1980]. The drawback of the SASE principle is its relatively broad emission bandwidth and thus its low temporal coherence and its poor pulse to pulse stability. In the hard x-ray regime

[1] See chapter 2 for more details about FELs.
[2] See section 2.1.2 for details about the SASE principle.

two different schemes have been proposed to overcome these drawbacks. The proposed schemes are the "self-seeding" scheme[3] and the "oscillator" scheme, which is considered in this work. Both schemes utilize Bragg-reflecting diamond mirrors to narrow the bandwidth of the emitted radiation and use that narrow bandwidth radiation to initiate (seed) the subsequent radiation generation. Bragg mirrors are used because in the x-ray regime no conventional mirrors are available, which reflect over a wide angle and with a sufficient reflectance. Because of its unique combination of superb thermo-mechanical and optical properties, diamond is the best known material for high power x-ray optics. These outstanding material properties include a high mechanical and radiation hardness, a high thermal diffusivity, a low thermal expansion and a high Bragg reflectivity of x-rays [Shvyd'ko et al., 2011].

1.1 Motivation

The recently proposed concept of an XFELO (x-ray free electron laser oscillator) described in [Kim et al., 2008; Lindberg et al., 2011] potentially offers performance complementary to a SASE (self-amplified spontaneous emission) based FEL.[4] The proposed XFELO uses a crystal cavity to provide narrow band feedback of the SASE radiation and has the potential to produce hard x-rays with energies between 5 and 20 keV. Due to the feedback of the radiation the XFELO only requires an undulator of about 5 - 20 m length, which is an order of magnitude less than the undulator length required by a SASE or self-seeded FEL. While the outcoupled peak power of such an XFELO (about 50 MW) is predicted to be lower by about 3 orders of magnitude compared to SASE-XFELs, the bandwidth will be of the order of $\Delta\nu/\nu \approx 10^{-5}$ - 10^{-7} which is 2 - 4 orders of magnitude narrower than the bandwidth of a SASE-XFEL ($\Delta\nu/\nu \approx 10^{-3}$). The peak brilliance of an XFELO is predicted to be about $7 \cdot 10^{34}$ photons/(s mm^2 mrad^2 0.5% BW), which is about one order of magnitude more than the peak brilliance of a SASE based XFEL [Zemella et al., 2011].

Compared to a self-seeded XFEL the peak power of an XFELO is lower by about two orders of magnitude and the bandwidth is more narrow by 0.5 - 2 orders of magnitude than the bandwidth of a self-seeded XFEL ($\Delta\nu/\nu \approx 5 \cdot 10^{-5}$). The pulses of an XFELO will have a significantly larger longitudinal coherence than SASE-XFELs up to full longitudinal coherence along the photon pulse and a higher pulse to pulse stability than self-seeded XFELs and SASE-XFELs. Due to these unique properties an XFELO

[3] See section 2.1.2 for more details about self-seeding.
[4] See sections 1.2 and 2.1.3 and figures 1.1 and 1.2 for more details about the concept of an XFELO.

is a powerful x-ray source for various experiments like high resolution spectroscopy, Mössbauer spectroscopy, x-ray photoemission spectroscopy and x-ray imaging with nm resolution. With an appropriate cavity stabilization an XFELO even offers inter-pulse coherence which would increase the coherence length from picoseconds to microseconds or longer. This would result in novel experimental techniques in x-ray quantum optics as well as time and length standards of greatly enhanced precision [Adams and Kim, 2015].

In order to keep the cavity within a manageable size, the electron bunch repetition rate has to be about 1 MHz or higher. This constraint of a MHz reppetition rate together with the expected x-ray pulses of about 300 µJ with a beam radius at the mirrors of about 50 µm impose a high heat load to the mirrors [Zemella et al., 2012]. The heat load on Bragg mirrors is a major issue because an undistorted Bragg reflection relies on a constant spacing in the atomic lattice. Due to the thermal expansion of the lattice the heat load in the mirrors can shift and distort the wavelength range which can be reflected. Those shifts and distortions inhibit the feedback of the radiation to the undulator and thus inhibit the whole XFELO process.

In order to increase the tolerable heat load on the mirrors, it was suggested [Sinn, 2007] to operate the mirrors at cryogenic temperatures. Cryogenic temperatures are expected to be favorable because at those temperatures, the thermal diffusivity of diamond is significantly higher and the thermal expansion significantly lower. Both properties are expected to result in a greatly reduced shift and distortion of the Bragg reflectivity curve of the mirrors. The thermal expansion of diamond at cryogenic temperatures has recently been measured with a high precision [Stoupin and Shvyd'ko, 2011]. The thermal diffusivity – the ratio between the thermal conductivity and the volumetric heat capacity – is known for diamond at cryogenic temperatures but the prediction of the actual temperature evolution of a mirror is based on a heat transfer equation. The usually applied classical heat equation (HE) assumes the mean free path (MFP) of the heat carriers (phonons in the case of diamond as an insulating material) to be small compared to the characteristic length scale of the considered system. Since the MFP of the phonons increases when the temperature is decreased the MFP reaches the characteristic length scale of the mirrors at cryogenic temperatures. Thus the HE is expected to fail at cryogenic temperatures. This failure is hard to predict without the knowledge of the temperature dependent MFP spectrum of the phonons, which is unknown for diamond. Due to this issues the temperature evolution of a diamond Bragg mirror for an XFELO at cryogenic temperatures is hard to predict as well.

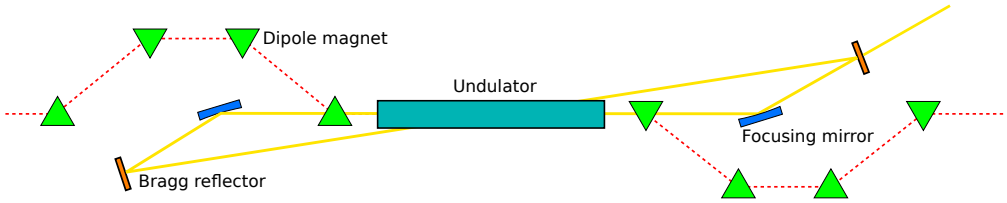

Figure 1.1: Scheme of an XFELO. The red dashed line represents the path of the electron beam, which comes from the left and is deflected by the dipole magnets (green triangles) to bypass the focusing mirrors (blue rectangles) of the x-ray cavity. The yellow line represents the path of the x-ray beam, which traverses the undulator in the same direction as the electron beam. At the Bragg reflector (orange rectangle) on the right, a fraction of the x-ray beam is coupled out of the cavity.

Because the temperature evolution of a Bragg mirror determines its stain, and thus the wavelength, which can be reflected, this work focuses on the influence of the absorbed fraction of incident radiation pulses on the condition of diamond crystals used as Bragg mirrors. A pump-probe experimental setup is developed, capable of simulating the heat load expected to be deposited by an XFELO pulse and measuring the resulting temperature decay. Furthermore, numerical studies are presented which reveal the expected strain generated by the absorbed radiation power and the associated change in Bragg reflectivity.

1.2 Scheme of an XFELO

An XFELO consists of four major components:

1. The electron accelerator, which provides high brightness electron bunches of several GeV with a MHz repetition rate.

2. The electron optics, which matches the electron and x-ray beam.

3. The undulator, where the matched electron and x-ray beam interact.

4. The x-ray cavity, in which the generated x-ray pulse circulates.

In figure 1.1, a scheme of an XFELO is shown in which components 2-4 of the list above are illustrated. The electron optics are illustrated without focusing elements[5], which would be placed before the first dipole magnet on the left of the figure. The

[5]See section 4.1 and figure 4.1 for more details about the appropriate electron optics.

electron beam comes from the left and gets focused into the middle of the undulator. In order to bypass the x-ray focusing elements (elliptical grazing incidence mirrors) the electron beam passes a chicane. In the undulator, the electron beam starts to generate spontaneous undulator radiation.[6] During the passage of the undulator the undulator radiation starts to interact with the electron bunch and FEL radiation is generated.[7] At the undulator exit, the FEL radiation is collimated by the first grazing incidence mirror and directed to the outcoupling mirror. Here, the majority (typically about 90-98%) of the generated radiation which fulfills the Bragg condition is reflected and the rest of the radiation is coupled out of the cavity or is absorbed by the Bragg mirror.[8] The reflected radiation is directed to the second Bragg mirror and then to the second grazing incidence mirror where the radiation is focused into the middle of the undulator. At the entrance of the undulator, the x-ray pulse is matched to the next electron bunch and initiates (seeds) the FEL process. Over many cycles, this leads to a strong increase in radiation power and because only that fraction of the radiation which fulfills the Bragg condition is fed back into the undulator, the generated radiation has a very narrow bandwidth.

In order to utilize the principle ability of an FELO to tune the wavelength of the generated radiation continuously over a wide range, the Bragg angle of of the mirrors has to be changed to maintain the Bragg condition (eq. (1.1)). The cavity shown in figure 1.1 and 1.2 (top) does not allow practically interesting tuning ranges because the incidence angle of the focusing grazing incidence mirrors has to be below their critical angle of about 1 mrad for 10 keV x-rays. This requirement results in a tuning range of the wavelength of $\Delta\lambda/\lambda \approx 10^{-6}$. Larger tuning ranges can be achieved with a cavity consisting of four Bragg crystals and two focusing elements shown in figure 1.2 (bottom). In this cavity the incidence angle on the grazing incidence mirrors is kept constant while the incidence angle on the Bragg mirrors can be changed. The tuning is done by shifting the two additional Bragg mirrors in the direction indicated by the black arrow in figure 1.2 (bottom) while the Bragg angle of the mirrors is adjusted [Kim and Shvyd'ko, 2009]. Installed in an accelerator tunnel of the European XFEL where about 4 m for shifting the mirrors are available, a tuning range of up to 0.5% can be achieved [Zemella, 2013].

[6] See section 2.2.1 and figure 2.1 for details about undulators and its radiation.
[7] This process is called SASE (self-amplified spontaneous emission). More derails about SASE can be found in section 2.1.2.
[8] See figure 1.4 for the reflectivity curves of different diamond crystals.

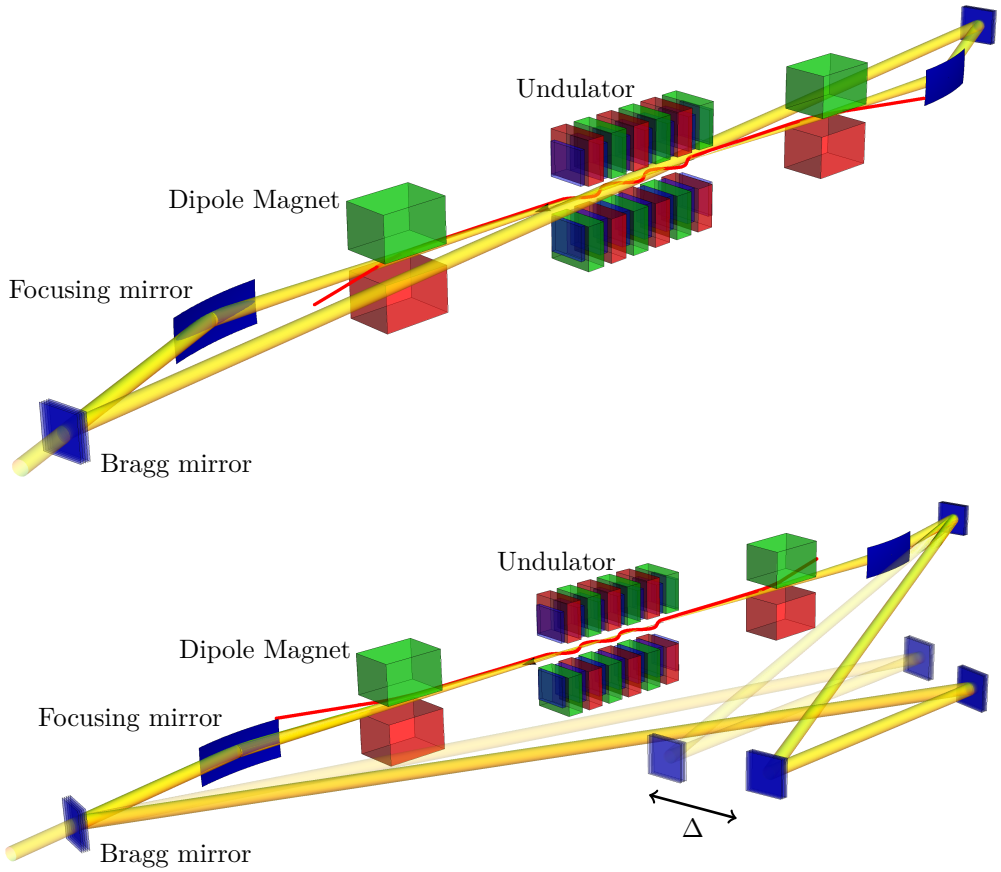

Figure 1.2: Comparison of two different XFELO cavities. The red lines represent the path of the electron beam which comes from the right and is deflected by the dipole magnets to bypass the focusing mirrors of the x-ray cavity. The path of the the x-ray beam is shown in yellow. The top cavity is identical to the cavity shown in figure 1.1. The bottom cavity consists of four Bragg mirrors and two grazing incidence mirrors and can be tuned over a wide wavelength range. The tuning of the cavity is done by shifting the additional Bragg mirrors in the direction indicated by the black arrow, which is indicated by the transparent drawn Bragg mirrors and x-ray beam. In the bottom figure, the color code for the polarity of the dipole magnets is inverted. The figure is modified from [Zemella, 2013].

1.2.1 Principle and Characteristics of Bragg Reflection

Bragg diffraction – a special case of Laue diffraction – originates from scattering of x-rays at a periodic crystal structure. In figure 1.3 the scheme of the Bragg reflection is shown. The reflection takes place when waves scattered at the different planes of the periodic crystal structure interfere constructively. This is the case when the so called Bragg condition

$$n\lambda_{\mathrm{B}} = 2d_{\mathrm{H}}(T)\sin(\theta_{\mathrm{B}}) \tag{1.1}$$

is fulfilled, where n is an integer determining the diffraction order, λ_{B} is the radiation wavelength at which the reflection occurs, d_{H} is the distance between the periodic lattice planes, T the temperature and θ_{B} is the angle at which the reflection occurs. The periodic lattice planes can be determined by three integers (hkl) – the Miller indices. However, only reflections with a non-vanishing structure factor can actually be observed [Kittel, 2004, p. 39]. In a cubic lattice like a diamond crystal with a lattice constant $a = 3.567\,\text{Å}$ [Kittel, 2004, p. 17], the spacing between the lattice planes is given by

$$d_{\mathrm{H}}(T) = \frac{a(T)}{\sqrt{h^2 + k^2 + l^2}}. \tag{1.2}$$

Higher order diffractions $n > 1$ are often denoted by $n(hkl)$.[9] Due to the thermal expansion of a crystal the lattice constant and thus the Bragg condition is dependent on temperature. For that reason the temperature of the XFELO Bragg mirrors should be kept as constant as possible to ensure stable XFELO operation. Equation (1.1) does not yield any information about the angular or wavelength range in which the reflection occurs and no value for the actual reflectivity can be obtained. In order to obtain the actual reflectivity curves, the dynamical theory of x-ray diffraction has to be applied [Authier, 2001]. This theory is complex and therefore only the resulting reflectivity curve for a diamond (444) reflection is shown in figure 1.4.[10] The plot on the left shows the reflectivity and field phase over the change in photon energy of a (444) reflection for an infinitely thick diamond crystal in backscattering geometry. The plot on the right shows the reflectivity and transmissivity of a 42 µm thick diamond crystal in the same scattering geometry. The plot on the left corresponds to a standard cavity mirror while the plot on the right corresponds to an outcoupling mirror, where the fraction of outcoupled radiation is determined by the crystal thickness. In both cases the relative spectral width of the Bragg reflection is very narrow, which means that only a very

[9] For example a (1 1 1) reflex of the order $n = 4$ can be denoted as (4 4 4).
[10] The applied theory assumes a perfect unstrained crystal structure.

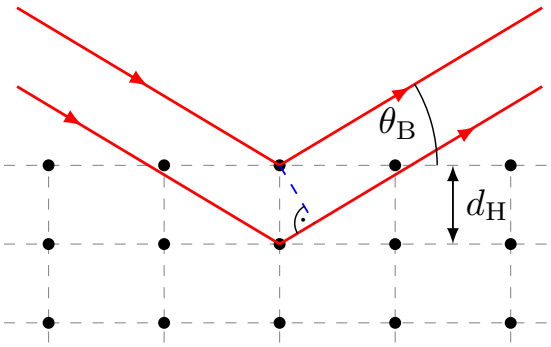

Figure 1.3: Scheme of the Bragg reflection. The red lines represent the incident and reflected radiation. The black dots connected by the black dashed lines represent the lattice of the crystal. The radiation at the Bragg wavelength λ_B is scattered at the different lattice planes and it interferes constructively at the Bragg angle θ_B, which causes the Bragg reflection. The figure is taken from [Zemella, 2013].

narrow part of the undulator and SASE radiation is reflected. The reflection curve of the 42 µm thick crystal on the right shows fringes (local maxima of lower reflectivity) on both sides of the principal maximum of the curve. These fringes are caused by the finite thickness of the crystal and thus the finite number of lattice planes involved in the scattering process. For the same reason the 42 µm thick crystal transmits only a fraction of the radiation at the Bragg wavelength. The distance over which the electric field in the crystal decays by e^{-1} or the field intensity decays by e^{-2} is called the extinction length of the radiation. From the dynamical theory of x-ray diffraction, a relation between the relative spectral width of the Bragg reflection ϵ_B and the extinction length of the radiation l_ext can be derived, which yields [Shvyd'ko, 2004, p. 77]

$$l_\mathrm{ext} \approx \frac{d_\mathrm{H}}{\epsilon_\mathrm{B}\pi}. \tag{1.3}$$

The extinction length of the radiation is an important property because it determines the distance over which the heat load caused by the absorbed fraction of the radiation is deposited. According to equation (1.3) and given a relative spectral width of the Bragg reflection $\epsilon_\mathrm{B} \approx 1.6 \cdot 10^{-6}$, the extinction length yields about 41 µm.[11] Thus, the absorbed fraction of the incident x-ray pulses causes an initial temperature change of exponential shape in the cross-plane direction, where the surface temperature change decays by e^{-2}

[11] This extinction length is calculated from equation (1.3), which is derived from the dynamical theory of x-ray diffraction of unstrained perfect crystals. For the calculation of the extinction length of strained or imperfect crystals a more sophisticated theory has to be applied (cf. sec. 4.3).

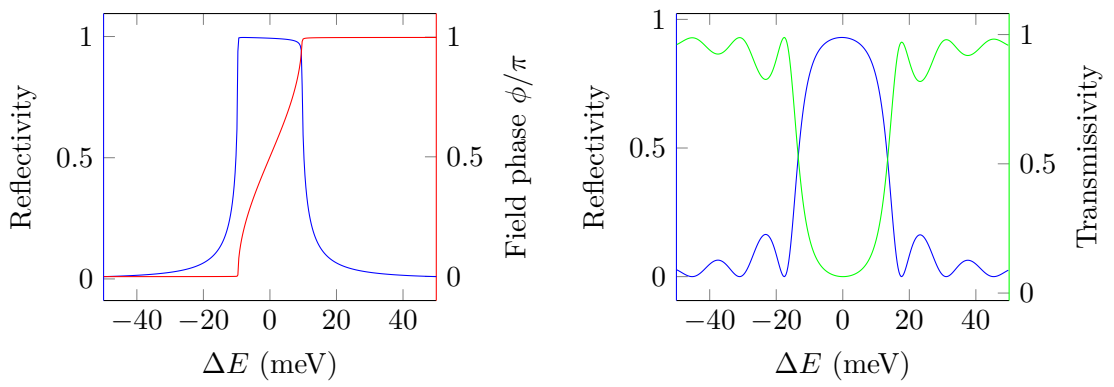

Figure 1.4: Bragg reflection (4 4 4) curve of an infinitely thick and a 42 µm thick diamond crystal in backscattering geometry ($\theta_B = 90°$). The 42 µm crystal can be used to couple a fraction of the XFELO pulse out of the cavity. The energy in the center of the peaks is about 12067 eV.

within 41 µm. Then the heat starts to diffuse into the crystal on a ns time scale.[12] The influence of a certain temperature change ΔT on the Bragg reflection can be estimated by means of the simple relation

$$\eta \approx \beta \Delta T \approx \frac{\Delta \lambda_B}{\lambda_B}, \tag{1.4}$$

where η is the strain of the material and β is the coefficient of thermal expansion.[13] When comparing the relative wavelength change of the Bragg reflection $\Delta\lambda_B/\lambda_B$ with the relative spectral width of the Bragg reflection ϵ_B, the influence of strain is negligible for $\Delta\lambda_B/\lambda_B \ll \epsilon_B$, otherwise it has to be taken into account. Figure 3.2 shows the temperature dependence of the coefficient of thermal expansion. The comparison of the coefficients of thermal expansion at 300 K ($1.1 \cdot 10^{-6}\,\mathrm{K}^{-1}$) and 50 K ($5.4 \cdot 10^{-9}\,\mathrm{K}^{-1}$) shows that the relative wavelength change per degree Kelvin at 50 K is lower by more than two orders of magnitude.

Because the XFELO pulses are temporally too short to affect their own Bragg condition, the crystal heating acts only on the subsequent pulses. Therefore, the crystal temperature upon arrival of the subsequent x-ray pulse is crucial. Figure 5.4 shows the

[12] See figures 5.4 and 5.5 for the temporal and spatial evolution of the temperature generated by absorbed radiation for two different heat transfer models. In section 3.4 a detailed description of the heat transfer in insulators and semiconductors is given.

[13] See section 3.2 for more details about thermal expansion of crystals and section 3.3 for more details about thermally induced strain in solids.

surface temperature evolution of a diamond crystal heated by a laser pulse at room temperature and at a cryogenic temperature. Because of the smaller heat capacity at cryogenic temperatures, the initial temperature jump at those base temperatures is much higher but due to the higher thermal diffusivity the cooling is much faster and after some time, the temperature change even falls below the temperature change of the room temperature crystal. The curves in figure 5.4 are based on the classical heat equation (based on Fourier's law) and the hyperbolic heat equation (cf. sec. 3.4.3.1). To what extent these equations describe the heat transport at cryogenic temperatures is shown in the course of this work. However, even under the conservative assumption that the temperature change upon arrival of the subsequent x-ray pulse was identical for both crystal base temperatures, the shift in the relative Bragg wavelength would be orders of magnitude lower for the cryogenic cooled crystal because of the considerably lower coefficient of thermal expansion at those temperatures. This property caused by the strongly decreased thermal expansion and the strongly increased thermal diffusivity at cryogenic temperatures call for the operation of the Bragg mirrors at cryogenic temperatures.

2 Free-Electron Lasers

A free electron laser (FEL) is a coherent light source which is based on the interaction of relativistic electrons with electromagnetic radiation in vacuum. FELs can generate radiation at any wavelength from the microwave to the x-ray regime. Due to their operating principle FELs are related to conventional vacuum tube devices which are capable of generating coherent radiation continuously from the km to the mm wavelength range. The operating principle of the FEL was invented by John Madey [Madey, 1971] and experimentally demonstrated [Deacon et al., 1977] with an infrared FEL by his group in the 1970s. Since then, tremendous progress has been made in the FEL development and today, FELs are firmly established among other light sources. The merits of FEL radiation are their high degree of polarization, their transverse coherence, a high efficiency for the conversion from electron beam power to radiation power, their wavelength tunability and their high level of average output power.

2.1 Types of Free-Electron Lasers

When a relativistic electron is deflected in the dipole magnet of a synchrotron, the particle emits the so called synchrotron radiation. The spectrum of synchrotron radiation ranges from zero to frequencies beyond the critical frequency

$$\omega_\mathrm{c} = \frac{3c\gamma}{2R}, \tag{2.1}$$

which is a measure to characterize the emitted spectrum.[14] Here c represents the speed of light, γ the Lorentz factor and R represents the bending radius of the magnet. Most of the power radiated by a relativistic electron is contained in a cone with the opening angle [Wille, 1992, p. 42]

$$\theta_\mathrm{cone} \approx \frac{2}{\gamma}. \tag{2.2}$$

The core component of all FELs is the undulator. An undulator consists of an arrangement of short dipole magnets with alternating polarity. This arrangement, shown in

[14] The critical frequency separates the emitted spectrum in two parts of equal size.

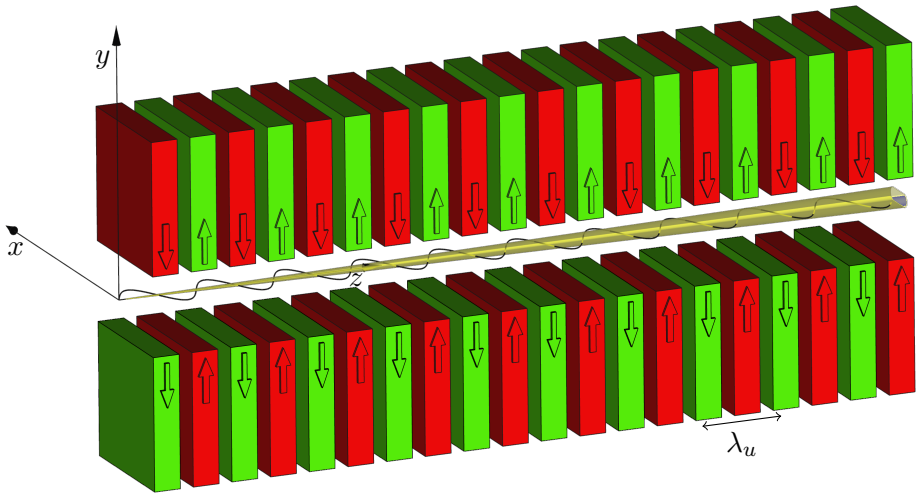

Figure 2.1: Scheme of a planar undulator and the associated electron trajectory. The amplitude of the sinusoidal trajectory (black line) is exaggerated and is only some µm in real undulators. The arrows indicate the direction of the magnetization. The generated radiation is represented by the yellowish cone on the undulator axis. While the opening angle of the cone in the y-direction is $2/\gamma$, the opening angle in the x-direction depends additionally on the undulator parameter K (cf. equation (2.7)) and for $K > 1$ the opening angle is given by $2K/\gamma$. If the opening angles are almost equal, which is the case for $K \lesssim 1$, this kind of magnet arrangement is called undulator, otherwise it is called wiggler.

figure 2.1, creates a field which forces a traversing electron on a sinusoidal trajectory around the undulator axis. After traversing an even number of dipole magnets the electrons have not gained any overall deflection. Due to the sinusoidal trajectory the electrons perform oscillations perpendicular to the undulator axis which leads to the emission of the so called undulator radiation. Compared to the radiation emitted at a single bending magnet, undulator radiation is much more useful for experiments because it has a much narrower bandwidth and a lower divergence within this bandwidth. The wavelength of undulator radiation can be tuned to any desired value by changing the electron energy. The electrons in an undulator usually radiate independently of each other which makes the radiation incoherent[15] and therefore the intensity of the emitted radiation is proportional to the number of radiating electrons. To increase the number of photons per second and decrease the divergence and bandwidth of these photons, an undulator can be utilized to set up an FEL. In an FEL, the electrons traverse the undulator on the same path as for ordinary undulator radiation but under certain conditions, the electrons start to interact with the light wave and transfer energy to it. This interaction leads to a correlated motion of the electrons on the length scale of the radiation wavelength, which in turn leads to an exponential growth of the radiation field. The initial light wave for the FEL process – also called seed radiation – can either be an external source or the spontaneous undulator radiation, which is always present in an FEL as a background. Depending on how the seed radiation is provided, FELs can be grouped into three categories, which are schematically shown in figure 2.2: The FEL amplifier (2.2 a), the SASE (self-amplified spontaneous emission) FEL (2.2 b) and the FEL Oscillator (2.2 c).

2.1.1 FEL Amplifier

In an FEL amplifier, an external light source is used to initiate (seed) the FEL process. The FEL amplifier is a single pass device which usually works in the high gain regime (cf. sec. 2.2.3). A major feature of the FEL amplifier is that the output signal can be controlled by the seed radiation (input signal) – as in an electronic amplifier. FEL amplifiers can, in principle, cover all wavelength ranges where appropriate seed sources are available. Operation of a conventional FEL amplifier has been demonstrated for wavelengths down to 266 nm, which corresponds to the fourth harmonic of a Nd:YAG Laser [Murphy and Wang, 2008] and with higher harmonic generation in an argon gas cell seeding at

[15] Undulator radiation could only be coherent if the electron bunch wold be shorter than radiation wavelength. From the optical to the x-ray regime this condition can not be fulfilled by today's accelerator technology.

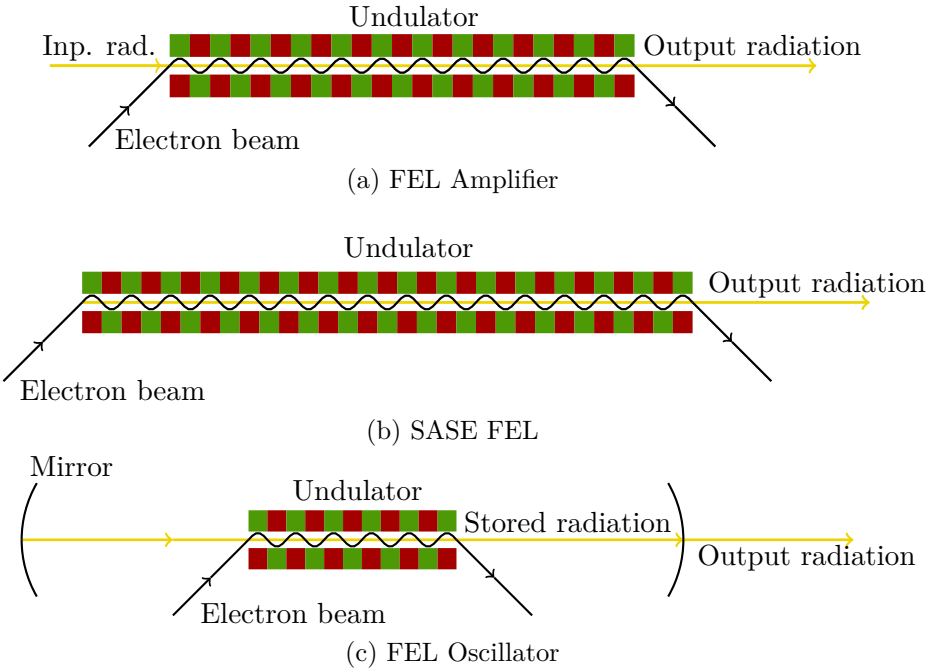

(a) FEL Amplifier

(b) SASE FEL

(c) FEL Oscillator

Figure 2.2: Schemes of the different FEL principles. The figure (a) shows an FEL amplifier, figure (b) a SASE FEL and figure (c) an FEL oscillator. The figure is modified from [Zemella, 2013].

38 nm could be demonstrated [Ackermann et al., 2013]. An alternative way to reach even shorter wavelengths is to combine the FEL amplifier with a harmonic-generation scheme. With the so called high-gain harmonic generation (HGHG) 20 nm radiation with unprecedented shot-to-shot wavelength stability and low-intensity fluctuations was generated [Allaria et al., 2012].

2.1.2 SASE FEL

Another FEL type, shown in figure 2.2 b, is the SASE (self-amplified spontaneous emission) FEL. A SASE FEL is in principle an FEL amplifier with no external input signal and – as in an electronic amplifier – without an input signal, only noise is amplified. In the case of the SASE FEL the noise is generated by the spontaneous undulator radiation, which is always present in an FEL. The amplification of the noise within the amplification bandwidth of the FEL requires no external seed radiation and therefore, they can in principle operate at any wavelength. For that reason, SASE FELs are today used as light sources from wavelengths of about 100 nm to below 1 Å[Emma et al., 2010]. Because the input signal of a SASE FEL is the longitudinally incoherent undulator radi-

ation, the output exhibits a lack of longitudinal coherence, too. In addition, the resulting spectrum is relatively broad[16] and noisy. To overcome this lack in longitudinal coherence and spectral width, significant effort has been made which led to the combination of a SASE FEL with an FEL amplifier separated by a monochromator. This setup is called a self seeded FEL. For FELs in the hard x-ray range no conventional optical elements are available and the monochromator is represented by a Bragg-crystal. With this setup near Fourier-transform-limited x-ray pulses with 0.4-0.5 eV bandwidth at 8-9 keV have been achieved [Amann et al., 2012]. These results correspond to a reduction in relative bandwidth of about 40-50 times compared to a SASE FEL at this wavelength.

2.1.3 FEL Oscillator

In an FEL oscillator (FELO) the spontaneous undulator radiation[17] of an initiating electron bunch is trapped in an optical cavity where it circulates with an integer multiple of the electron bunch repetition rate. With this timing the subsequent radiation pulses and the electron bunches are matched at the beginning of the undulator and traverse it in this state. This leads to a seeding of those electron bunches, and if the condition

$$(1 + G_0)R > 1 \tag{2.3}$$

is satisfied, it leads to a gain of the radiation stored in the undulator. Here G_0 is the initial gain and R is the overall reflectivity of the optical cavity. The losses in the cavity include absorption in the mirrors, losses due to scattering and the fraction of the radiation which is coupled out of the cavity for experiments. The FELO will reach saturation, when

$$(1 + G)R = 1, \tag{2.4}$$

where G is the intensity dependent gain. Today FELOs exist emitting in the IR to the near UV (ultra violet) spectral region. A storage ring FEL currently achieved wavelengths below 190 nm [Curbis et al., 2005] and many FELs based on pulsed copper RF accelerators operate as productive IR user facilities [Van der Wiel and Van Amersfoort, 1993]. In the x-ray region no FELOs exist because no conventional mirrors are available for this wavelength, which reflect over a wide angle and with a sufficient reflectance. To overcome this limitation for the hard x-ray region, a cavity, composed of Bragg crystals and some focusing elements, has already been proposed decades ago [Colella and

[16] It spans over the whole amplification bandwidth of the FEL.
[17] If the lasing process is seeded by an external source the FEL is called regenerative amplifier.

Luccio, 1984] but could not be realized until today. Another technical challenge has been the accelerator development. In order to keep the cavity length in a technically handable range, the bunch repetition of the accelerator has to be in the MHz range while the bunch trains have to be long (hundreds of µs) to reach FEL saturation. Those inter-bunch time structures are not challenging for circular machines or in the case of a LINAC (linear accelerator) driving an IR FELO, where only electron energies of 20-60 MeV are needed [Li et al., 2017] but for FELOs operating in the x-ray regime several GeV high brightness electron beams are required. With today's understanding of accelerator physics such bright electron beams required to run an XFEL can only be produced with a LINAC. The required time structure and electron energy in turn are difficult to achieve with a conventional copper LINAC at a reasonable acceleration gradient because of the heat load deposited by the RF power. In order to keep an XFELO (X-ray free electron laser oscillator) driving LINAC to a manageable size, the constraints of a MHz repetition rate and long bunch trains impose the requirement for SRF (superconducting radio frequency) accelerator technology. With the commissioning of the European XFEL, such an accelerator is now available for the first time [Decking and Weise, 2017]. Due to the technological progress in the development of x-ray optics (among other progresses) today nearly perfect diamond Bragg crystals with over 99% reflectivity are available [Shvyd'ko et al., 2011]. Therefore, it seems as if the time has come for the realization of an XFELO [Kim et al., 2008].

2.2 Basic Physics of Free Electron Lasers

2.2.1 Undulator Radiation

Undulator radiation is a phenomenon that always takes place when an electron with a high kinetic energy traverses an undulator. In FEL radiation, it is always present as a background and in a SASE FEL, it is even utilized for seeding the FEL. Therefore, in the FEL context undulator radiation can be considered an analogon to spontaneous emission in conventional Lasers. In the following section, a brief overview over the most important relations regarding undulator radiation is given. This overview only treats planar undulators as shown in figure 2.1, which produce linearly polarized light. Helical undulators, which produce circular polarized light, are not considered. The magnetic field on the undulator axis at $y = 0$ is

$$\boldsymbol{B} = -B_0 \sin(k_\mathrm{u} z)\boldsymbol{e}_y, \tag{2.5}$$

where B_0 is the peak magnetic field of the undulator, k_u is the undulator wave number and $\boldsymbol{e}_y$ is the unit vector in y direction. When an electron enters the undulator, its magnetic field causes, to second order, the trajectory [Schmueser et al., 2014, p. 14]

$$x(t) = \frac{K}{\gamma k_\mathrm{u}} \sin(\omega_\mathrm{u} t), \tag{2.6a}$$

$$z(t) = \bar{v}_z t - \frac{K^2}{8\gamma^2 k_\mathrm{u}} \sin(2\omega_\mathrm{u} t), \tag{2.6b}$$

where γ is the Lorentz factor, K the undulator parameter and $\bar{v}_z$ the average velocity of the electron in the z direction and $\omega_\mathrm{u}$is the angular frequency of the electron in the undulator defined by $\omega_\mathrm{u} = \bar{v} k_\mathrm{u} \approx c k_\mathrm{u}$. The undulator parameter is an important parameter which is often used. It is defined as:

$$K = \frac{e B_0}{m_\mathrm{e} c k_\mathrm{u}} \approx 0.934 \cdot B_0[\mathrm{T}] \cdot \lambda_\mathrm{u}[\mathrm{cm}]. \tag{2.7}$$

The average velocity $\bar{v}$ used in equation (2.6b) is given by

$$\bar{v}_z = \left(1 - \frac{1}{2\gamma^2}\left(1 + \frac{K^2}{2}\right)\right). \tag{2.8}$$

The periodic oscillation of the electrons represented by equation (2.6) leads to the emission of radiation [Wille, 1992, p. 262] with the central wavelength

$$\lambda_\mathrm{l} = \frac{\lambda_\mathrm{u}}{2\gamma^2}\left(1 + \frac{K^2}{2} + \gamma^2\theta^2\right), \tag{2.9}$$

where λ_u is the undulator period and θ the emission angle relative to the beam axis. The overall radiation power of the spontaneous undulator radiation is given by

$$P_\mathrm{sp} = \frac{e^2 c \gamma^2 K^2 k_\mathrm{u}^2}{12\pi\epsilon_0}, \tag{2.10}$$

where e represents the elementary charge, c the speed of light and ϵ_0 the vacuum permittivity. The line width of the undulator radiation can be estimated as

$$\Delta\omega \approx \frac{\omega_\mathrm{l}}{N_\mathrm{u}}, \tag{2.11}$$

where ω_l is the center wavelength. The radiation within this bandwidth is emitted in a cone which has an RMS opening angle of [Wiedemann, 2007, p. 850]

$$\sigma_\theta \approx \frac{1}{\gamma}\sqrt{\frac{1+K^2/2}{2N_\mathrm{u}}} \approx \frac{1}{\gamma}\frac{1}{\sqrt{N_\mathrm{u}}} \text{ for } K \approx 1. \tag{2.12}$$

These radiation characteristics make undulator radiation itself a useful tool – far more useful than traditional synchrotron radiation from bending magnets.

2.2.2 Low Gain FEL

Since an FEL is, in principle, an amplifier for electromagnetic radiation with a low bandwidth some radiation is required to initiate the FEL process. As already mentioned in section 2.1, the seed for the FEL can either be an external light wave, which is typically a laser pule, or, as will be shown below, by spontaneous undulator radiation. For the following discussion an external plane wave

$$E_x(z,t) = E_0 \cos(k_\mathrm{l} z - \omega_\mathrm{l} t + \psi_0) \tag{2.13}$$

is assumed as the seed. Here, the amplitude E_0 of the light wave is assumed to be constant during the undulator passage. This approximation is the characteristic feature of the low gain theory, which decouples the electron motion from the light wave. The assumption of a constant amplitude is justified in the FELO case as long as the amplitude only grows by a few percent per undulator passage and usually at the beginning of an FEL amplifier within the so called lethargy regime, when the amplitude growth is only about a few percent. A single electron travelling in the field of a plane electromagnetic wave through an undulator changes its energy according to

$$\begin{aligned}\frac{\mathrm{d}W}{\mathrm{d}t} &= \boldsymbol{v}\cdot\boldsymbol{F} = -ev_x(t)E_x(t) = -e\frac{cK}{\gamma}\cos(k_\mathrm{u} z)E_0\cos(k_\mathrm{l} z - \omega_\mathrm{l} t + \psi_0)\\ &= -\frac{ecKE_0}{2\gamma}\left[\cos((k_\mathrm{l}+k_\mathrm{u})z - \omega_\mathrm{l} t + \psi_0) + \cos((k_\mathrm{l}-k_\mathrm{u})z - \omega_\mathrm{l} t + \psi_0)\right]\\ &= -\frac{ecKE_0}{2\gamma}\cos(\psi) - \frac{ecKE_0}{2\gamma}\cos(\chi),\end{aligned} \tag{2.14}$$

where v_x is obtained by the time derivative of equation (2.6)a using $\omega_\mathrm{u} = \bar{\beta} c k_\mathrm{u} \approx c k_\mathrm{u}$. The phases ψ and χ can be written with $z(t) = \bar{v}_z t$ as a function of the single variable t as

$$\psi(t) = (k_\mathrm{l} + k_\mathrm{u}) z(t) - \omega_\mathrm{l} t + \psi_0 \tag{2.15a}$$

$$\chi(t) = (k_\mathrm{l} - k_\mathrm{u}) z(t) - \omega_\mathrm{l} t + \psi_0, \tag{2.15b}$$

where ψ is called the ponderomotive phase. To maintain a continuous energy transfer from the electron to the light wave ψ must be constant and therefore the condition

$$\frac{\mathrm{d}\psi}{\mathrm{d}t} = (k_\mathrm{l} + k_\mathrm{u}) \bar{v}_z - k_\mathrm{l} c = 0 \tag{2.16}$$

has to be fulfilled [Wille, 1992, p. 271]. In this case, it can be shown that the $\cos(\chi)$-term in equation (2.14) carries out two oscillations per undulator period and thus cancels out. In equation (2.16) the relation $z(t) = \bar{v} t$ was used, which neglects the longitudinal oscillations of the electrons indicated by equation (2.6b). Combining equation (2.8) with the condition for sustained energy transfer (eq. (2.16)) leads to the light amplification wavelength [Madey, 1971; Huang and Kim, 2007]

$$\lambda_\mathrm{l} = \frac{\lambda_\mathrm{u}}{2{\gamma_\mathrm{r}}^2} \left(1 + \frac{K^2}{2}\right) \implies \gamma_\mathrm{r} = \sqrt{\frac{\lambda_\mathrm{u}}{2{\lambda_\mathrm{l}}^2} \left(1 + \frac{K^2}{2}\right)}, \tag{2.17}$$

which is equivalent to the on axis undulator radiation wavelength (cf. eq. (2.9)). For that reason, the spontaneous undulator radiation can be used as seed radiation for the FEL. The γ_r in equation (2.17) is the Lorentz factor of the resonance electron energy W_r interconnected by $W_\mathrm{r} = \gamma_\mathrm{r} m_\mathrm{e} c^2$. With this resonance electron energy a relative energy deviation η can be defined as

$$\eta = \frac{W - W_\mathrm{r}}{W_\mathrm{r}} = \frac{\gamma - \gamma_\mathrm{r}}{\gamma_\mathrm{r}} \qquad |\eta| \ll 1. \tag{2.18}$$

When $\eta \neq 0$, the condition (2.16) is not fulfilled any more and can be written in good approximation as

$$\frac{\mathrm{d}\psi}{\mathrm{d}t} = 2 k_\mathrm{u} c\, \eta \tag{2.19}$$

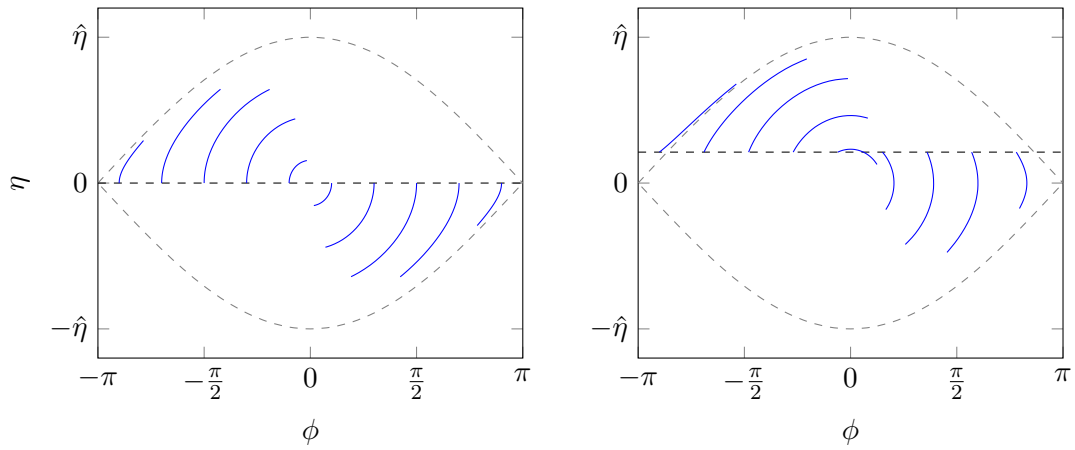

(a) Phase space motion for $\eta = 0$

(b) Phase space motion for $\eta > 0$

Figure 2.3: Solution of the FEL pendulum equations for $\eta = 0$ and $\eta > 0$ respectively. In both plots, all electrons are uniformly distributed in the initial ψ coordinate and all possess the same initial η coordinate. The dashed lines represent the separatrix. In figure (a) it can be seen from the symmetry of the system that the energy transfer from the electrons to the light wave is zero. In figure (b) more electrons lose energy to the light wave than gain energy from the light wave. The comparison between both plots shows that only for initial $\eta > 0$ energy transfer from the electrons to the light wave takes place.

For this approximation the fact is used that γ differs only slightly from γ_r. The change of η with time can be obtained from equation (2.14) and yields

$$\frac{\mathrm{d}\eta}{\mathrm{d}t} = -\frac{eKE_0}{2m_\mathrm{e}c\gamma_\mathrm{r}^2}\cos(\psi). \tag{2.20}$$

The equations (2.19) and (2.20) [Martellucci and Chester, 1983, p. 98] are called the FEL pendulum equations and they are fundamental in FEL physics. Figure 2.3 shows the solution of the pendulum equations in the (ϕ, η) phase space for several electrons with different initial phases ϕ, where $\phi = \psi + \pi/2$. In figure 2.3a the phase space motion of electrons with initial energy deviation $\eta = 0$ is shown and can be compared to 2.3b, where the phase space motion for electrons with an initial $\eta > 0$ is shown. It can be seen in figure 2.3a that there is no energy exchange between electrons and light wave in average because the same number of electrons spend energy to the light wave than gain energy from the light wave. In figure 2.3b it can be seen that the situation is not symmetric any more when $\eta > 0$. In this case, an energy transfer from the electrons to

the light wave takes place. Almost all electrons shown in figure 2.3 are bounded by the field of the light wave resulting in oscillatory motion. The so called separatrix (dashed lines in figure 2.3) divides the phase space area of bounded from the area of unbounded motion. All electrons outside the separatrix fulfill translations instead of oscillations. The equation for the separatrix is given by

$$\eta_{\mathrm{sep}}(\phi) = \pm\sqrt{\frac{eE_0K}{k_{\mathrm{u}}m_{\mathrm{e}}c^2\gamma_{\mathrm{r}}^2}}\cos\left(\frac{\phi}{2}\right) = \pm\hat{\eta}\cos\left(\frac{\phi}{2}\right). \tag{2.21}$$

The area enclosed by this separatrix is called, in analogy to the RF buckets in a storage ring, FEL bucket. A measure for the amount of energy transferred from the electron beam to the light wave is the gain. The gain G of a low gain FEL is defined as the relative radiation energy increase during an undulator pass ($G = \Delta W_{\mathrm{l}}/W_{\mathrm{l}}$) and it is given by [Madey, 1979]

$$G(\xi) = -\frac{\pi e^2\hat{K}^2N_{\mathrm{u}}^2\lambda_{\mathrm{u}}^2\,n_{\mathrm{e}}}{4\epsilon_0m_{\mathrm{e}}c^2\gamma_{\mathrm{r}}^3}\cdot\frac{\mathrm{d}}{\mathrm{d}\xi}\left(\frac{\sin^2\xi}{\xi^2}\right) \tag{2.22}$$

where ξ can be written as

$$\xi = \pi N_{\mathrm{u}}\frac{\omega_{\mathrm{l}}-\omega}{\omega_{\mathrm{l}}} \approx 2\pi N_{\mathrm{u}}\frac{\gamma-\gamma_{\mathrm{r}}}{\gamma_{\mathrm{r}}} = 2\pi N_{\mathrm{u}}\eta \tag{2.23}$$

and $\hat{K}$ is the modified undulator parameter defined by

$$\hat{K} = K\left[J_0\left(\frac{K^2}{4+2K^2}\right) - J_1\left(\frac{K^2}{4+2K^2}\right)\right] \tag{2.24}$$

Here the J_n are the Bessel functions. Equation (2.22) is the so called Madey theorem, which shows the proportionality between the FEL gain curve and the negative derivative of the undulator radiation line shape curve. Equation (2.23) shows that the variable ξ can either be interpreted a variation of the seed wavelength or as a variation of the electron energy. Figure 2.4 illustrates the Madey theorem. Because of the proportionality of ξ and η figure 2.4b can be considered as a quantitative description of figure 2.3. For negative η the light wave transfers energy to the electron beam and vice versa.

2.2.3 High Gain FEL

In the previous section (sec. 2.2.2) the essential physics of the 1D low gain approximation were presented. Since the low gain FEL theory assumes a constant electric field during

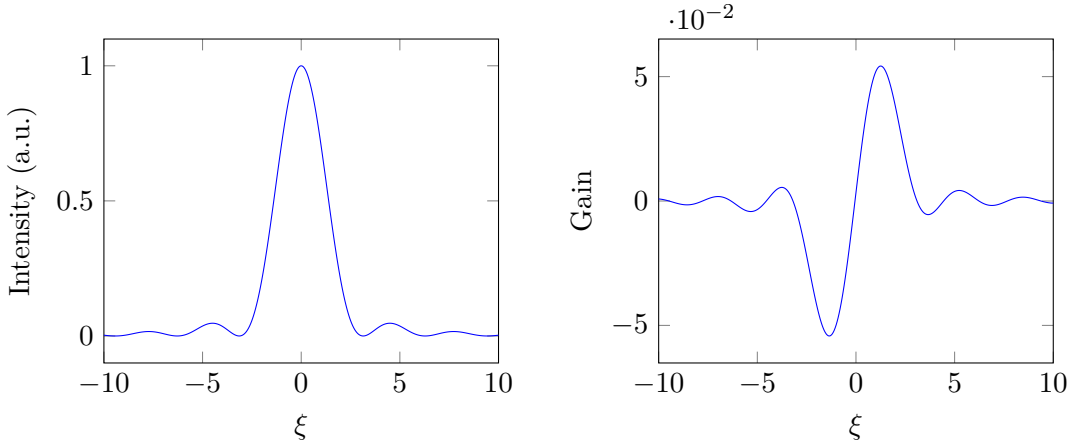

(a) Linewidth (b) Gain function

Figure 2.4: Depiction of the Madey theorem. (a) The line shape curve of undulator radiation. (b) Gain curve of a low gain FEL. See text for further explanation.

one undulator passage and neglects space charge forces generated by the electrons, all effects caused by electron-electron or electron-light wave interaction are not accessible by this theory. In this section, a brief introduction to the 1D high gain FEL theory shall be given. In the high gain theory, the coupled pendulum equations (2.19) and (2.20) are derived considering a variable electric field and the influence of a variable space charge distribution on the phase space motion of the electrons. Therefore, the inhomogeneous wave equation for an electromagnetic field is coupled to the modulation current in the electron bunch which in turn is coupled to the ponderomotive phases of all electrons in the bunch. In the periodic model[18] this treatment leads to a system of first order differential equations [Schmueser et al., 2014, p. 51] of the form

$$\frac{\mathrm{d}\psi_n}{\mathrm{d}z} = 2k_\mathrm{u}\eta_n, \tag{2.25a}$$

$$\frac{\mathrm{d}\eta_n}{\mathrm{d}z} = -\frac{e}{m_\mathrm{e}c^2\gamma_\mathrm{r}}\Re\left\{\left(\frac{\hat{K}\tilde{E}_x}{2\gamma_\mathrm{r}} - \frac{\mathrm{i}\mu_0 c^2}{\omega_\mathrm{l}}\cdot\tilde{j}_1\right)\exp(\mathrm{i}\psi_n)\right\}, \tag{2.25b}$$

$$\frac{\mathrm{d}\tilde{E}_x}{\mathrm{d}z} = -\frac{\mu_0 c\hat{K}}{4\gamma_\mathrm{r}}\cdot\tilde{j}_1, \tag{2.25c}$$

$$\tilde{j}_1 = j_0\frac{2}{N}\sum_{n=1}^{N}\exp(-\mathrm{i}\psi_n), \tag{2.25d}$$

[18] The periodic model assumes an infinitely long bunch with a periodic initial electron distribution, which includes a uniform initial electron distribution. The period of the electron distribution is given by the light wavelength λ_l.

where μ_0 is the vacuum permeability, n is the index of a single electron and N the total number of electrons which are initially contained in an interval of one radiation wavelength. Here, j_0 is the DC component of the current density, $\tilde{j}_1$ is the complex amplitude of the modulation current density and $\tilde{E}_x$ is the complex amplitude of the electric field in x-direction[19]. This set of $2N + 2$ coupled differential and algebraic equations describe the evolution of the ponderomotive phase ψ and energy deviation η of each electron as well as the amplitudes of the modulation current density $\tilde{j}_1$ and the electric field $\tilde{E}_x$ during one undulator passage. Essentially, the equations (2.25) describe a system of many interacting charged particles. This represents a classical many body problem which is well known not to be solveable analytically. By means of the numerical solution of equation (2.25) the gain process in an FEL amplifier seeded by a monochromatic wave including the saturation regime can be studied. This includes the phase space motion of the electrons and the evolution of the light wave amplitude. In figure 2.5 a numerical solution of the equations (2.25) is shown. In figure (a) the motion of ten electrons (blue lines) and the motion of the bucket center (red line) are shown in the (η, ϕ)-phase space. As in figure 2.3 the ponderomotive phase ψ is replaced by $\phi = \psi + \pi/2$. In figure (b) the evolution of the complex electric field amplitude is plotted as a function of the undulator length in measures of the power gain length L_{g0}, which is defined in equation (2.28). It can be seen on 2.5 (b) that after a certain distance the gain increases exponentially with the undulator length and finally saturates. This behavior can only be explained by the development of so called micro bunches, which are formed due to the interaction with the light wave [Huang and Kim, 2007] and they are slightly visible in figure 2.5 (a). They are shorter than a light wavelength and hence are able to radiate coherently like a single point charge. The time it takes to initiate the micro bunch structure is called the lethargy regime ($0 \leq z \lesssim 3L_{\mathrm{g0}}$). The saturation of the gain process in turn can be explained by an overbunching of the electrons, which means that after the bunching reaches a peak, it starts to be diminished by enduring interaction with the light wave. In the phase space plot 2.5 (a) the micro bunching effect can hardly be recognized since the growth of light wave amplitude makes the phase space motion nonuniform and in order to represent the whole phase space motion the trajectories are quite long. To understand the effect of micro bunching figure 2.3 might be more helpful.

Under the assumption that the periodic density modulation (micro bunching) remains small, the equations (2.25) can be simplified to a single third order equation which can be solved analytically. Because of the assumption of only a small periodic density

[19]The polarization direction of the light wave. See figure 2.1 for the definition of the coordinate system

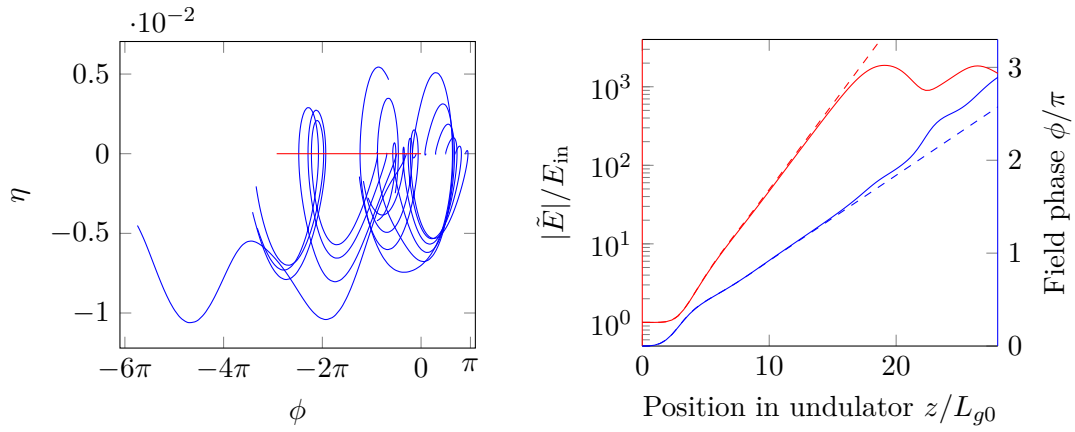

(a) Phase space motion

(b) Field evolution

Figure 2.5: Results of the high gain theory. Plot (a) shows the phase space motion of ten electrons (blue lines) and the motion of the FEL bucket (red line). The phase space motion was obtained from numerical solution of equation (2.25). Plot (b) shows the evolution of the complex field amplitude predicted from the analytic solution of equation (2.26) (dashed lines) and from the numerical solution of equation (2.25) (solid lines).

modulation, this equation does not cover the FEL saturation regime. For the special case of an initial $\eta = 0$ and neglecting space charge forces, which can be done in case of a low electron density modulation or electron density and a large electron energy, the solution to the third order equation yields [Schmueser et al., 2014, p. 59]

$$\tilde{E}_x(z) = \frac{E_{\mathrm{in}}}{3}\left[\exp\left(\left(\mathrm{i}+\sqrt{3}\right)\frac{\Gamma}{2}z\right) + \exp\left(\left(\mathrm{i}-\sqrt{3}\right)\frac{\Gamma}{2}z\right) + \exp\left(-\mathrm{i}\Gamma z\right)\right], \tag{2.26}$$

where E_{in} is the amplitude of the seeding light wave. This initial amplitude is a real value because the phase of the light wave at the beginning of the undulator is set to zero. The Γ is the so called gain parameter, which is defined as

$$\Gamma = \sqrt[3]{\frac{\mu_0 \hat{K}^2 e^2 k_{\mathrm{u}} n_{\mathrm{e}}}{4\gamma_{\mathrm{r}}^3 m_{\mathrm{e}}}}. \tag{2.27}$$

In figure 2.5 (b) this analytic solution is compared to the numeric solution of the equations (2.25). It can be seen that the analytic solution reproduces the results of the coupled first order equations (2.25) for $0 < z < 15L_{\mathrm{g0}}$. Beyond $15L_{\mathrm{g0}}$ the FEL saturation sets in and the assumptions made to obtain the analytic solution start to lose their

justification. With the gain parameter (2.27) another important quantity – the idealized 1D power gain length – can be defined as

$$L_{\mathrm{g0}} = \frac{1}{\sqrt{3}\Gamma} \tag{2.28}$$

The 1D power gain length characterizes the gain process in the regime of exponential growth, where the FEL radiation power increases with

$$P(z) \propto \exp\left(\sqrt{3}\Gamma z\right) \equiv \exp\left(\frac{z}{L_{\mathrm{g0}}}\right) \tag{2.29}$$

In the case shown in figure 2.5, this exponential regime is in the range of $3L_{\mathrm{g0}} < z < 15L_{\mathrm{g0}}$. The power gain length L_{g0} is just in idealization for the case of $\eta = 0$, negligible space charge forces and no electron beam energy spread. In addition, 3D effects like betatron oscillations and diffraction of the light wave are disregarded in this parameter. All these effects usually lead to an increase of the gain length. While the effects of $\eta \neq 0$, space charge forces and electron energy spread can be investigated within 1D FEL theory, the effects of betatron oscillations and light beam diffraction are not accessible by the 1D FEL theory. As a rule of thumb the 1D FEL theory is applicable if the electron beam radius $r_{\mathrm{b}} \gg \sqrt{L_{\mathrm{g0}}\lambda_{\mathrm{l}}}$. If this is not the case, the more general and more complex 3D FEL theory must be used, which has no analytic solution.

3 Laser Irradiated Solids

The interaction between the FEL radiation and the Bragg mirrors is the fundamental limitation in the realization of a cavity for an XFELO. This is because the requirements for the angular and spatial stability [Stoupin et al., 2010; Maag et al., 2015] of the crystals as well as for the stability of its lattice constants are very high while the expected brilliance of an XFELO is also very high. Therefore, light-matter interaction effects which are generally small or even negligible have to be considered. The effects which are directly associated with the laser irradiation are:

1. Radiation damage due to ionization [Als-Nielsen et al., 1994]
2. Vibration of the crystal in its mount due to thermal expansion or radiation pressure.
3. Change of the lattice constant due to thermal expansion [Zemella et al., 2012], whereby a homogeneous change of the lattice constant might be compensable by changing the Bragg angle.
4. Generation of ultrasonic pulses due to the thermal expansion or radiation pressure [Thomsen et al., 1986; Stoupin et al., 2012].

In this thesis only effects associated with thermal expansion are investigated. Therefore, in this chapter a good understanding of the processes which perturb the original thermal equilibrium (before laser irradiation) is to be developed.

3.1 Absorption of Photons in Insulators and Semiconductors

For photons from the visible to the x-ray regime (1.5 - 50000 eV) the major absorption process is the photoelectric effect [Leo, 2012]. This effect can be divided into the inner and the outer photoelectric effect. The inner photoelectric effect is the excitation of electrons by photons from the valence to the conduction band or in case of sufficiently high photon energies from the atomic inner shells to the conduction band. Figure 3.1 illustrates the carrier dynamics associated with the inner photoelectric effect. Depending

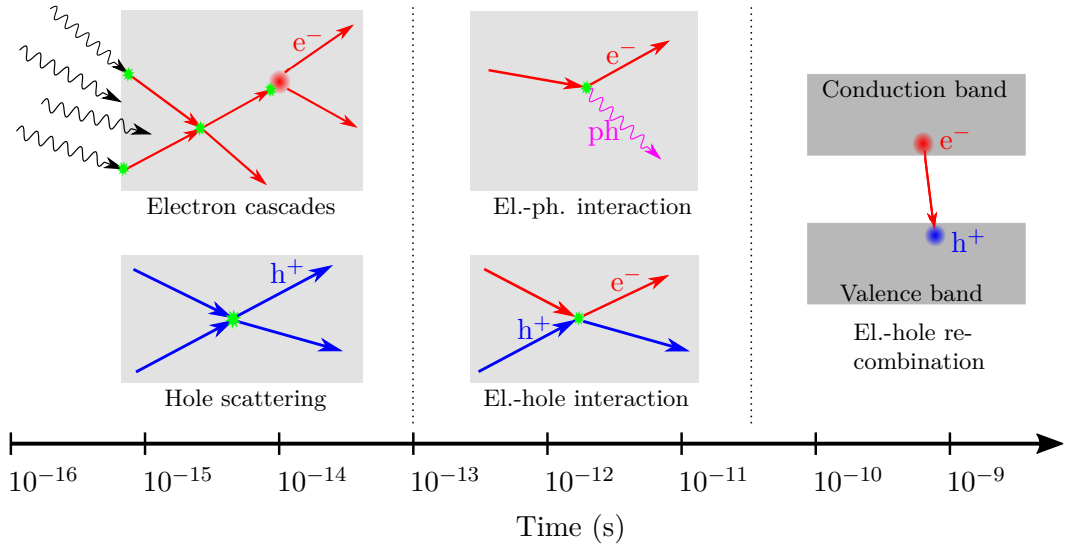

Figure 3.1: Time evolution of photon absorption and heat generation. The time line illustrates, on which time scale the different processes (in the gray boxes) dominate. The green stars indicate the interaction between particles and the arrows indicate moving particles whereas the blurred dots indicate static particles (particles with a relatively low kinetic energy). Electrons are depicted in red and holes in blue both with a straight arrow shaft. Photons are depicted in black and phonons in pink both with a sine shaped arrow shaft. Modified from [Ziaja et al., 2015]

on the excess energy of the electrons after the transition, secondary processes like the Auger effect (only for inner shell excitations of light elements [Ziaja et al., 2015]), electron impact ionization, electron-electron or electron-phonon scattering lead – possibly over several stages – to a thermalization of the primary electron in the conduction band. The thermalization dynamics in the conduction band can be divided into two time scales. On the first time scale the electron-electron thermalization which occurs typically within 10 to 100 fs takes place and on the second time scale the electron-lattice thermalization which occurs typically within tens of ps takes place.

When an electron reaches the surface of the solid with more energy than the work function, it is able to escape. This case is referred to as the outer photoelectric effect, in contrast to the inner photoelectric effect when the electron remains in the solid. In case of the inner photoelectric effect the electronic states in the conduction band possess a certain lifetime. Depending on the kind of band gap – direct or indirect – the electrons recombine after their lifetime primarily by radiative or thermal recombination.

In indirect band gap materials, like diamond, the so called trap-assisted recombination is the major recombination process. Here, the electrons recombine through a localized state (lattice defect) via the emission of a phonon to allow for the conservation of energy and crystal momentum. Therefore, the carrier lifetime of indirect band gap materials strongly depends on the concentration of recombination centers. In diamond, nitrogen is believed to play an important role as a recombination center. Depending on the nitrogen content the carrier lifetime in diamond is between 30 ps and 1000 ps [Konorova et al., 1966]. This implies (assuming a similar electron phonon thermalization time as in the conduction band) that a diamond crystal reaches a local thermal equilibrium about 0.1 to 1 ns after the irradiation with a fs light pulse. As a result of the above description one can summarize that the energy of incident photons is primarily absorbed by electrons and is transferred via different processes and timescales into the phonons of the crystal lattice.

3.1.1 Implications to the Modeling of XFELO Bragg Mirrors

Bragg reflection – the underlying principle of Bragg mirrors – relies on a well defined lattice constant. The lattice constant can potentially be perturbed by stress induced by intense fs XFELO pulses. The carrier thermalization dynamics pointed out in section 3.1 determine the stress generation. According to these carrier dynamics the stress generation occurs on two timescales. The first timescale is the electron-lattice thermalization time $\tau_{\text{el-latt}}$ which is typically of the order of some ps. The second timescale is the electron recombination time, which is for diamond of the order of hundreds of ps. Thermal expansion due to electron-lattice thermalization was observed in an fs optical pump and fs x-ray diffraction probe experiment in the semiconducting material InSb [Chin et al., 1999]. The dominant mechanism for electron relaxation in InSb is the emission of longitudinal optical phonons which was assumed to take 2 ps. The observed onset of the lattice expansion was about 10 ps after the arrival of the pump pulse. The delay of the onset of lattice expansion of about 7 ps was explained as a signature of non equilibrium phonon dynamics and the delay was assumed to be the thermalization time of the initial longitudinal optical phonons.

However, the stress induced within the material by such processes does not instantaneously expand the lattice because of the confinement of the surrounding crystal. Instead, the expansion has to nucleate at a free surface, forming a highly strained layer, which can than propagate with the speed of sound into the crystal. Due to lateral confinement, the lattice expansion occurs primarily normal to the surface [Kojima et al.,

1994]. In diamond, electron-lattice thermalization has a rapid and a slow component which can be associated with the relaxation via optical and acoustic phonons respectively. The time needed to reach thermal equilibrium between the carriers and the lattice was estimated to be 100 ps at 100 K and 30 ps at 300 K [Kozak et al., 2015].

The dynamical thermal expansion of diamond has also been directly observed (at room temperature) by an optical pump and x-ray diffraction probe experiment [Stoupin et al., 2012]. At this experiment a temporal resolution of about 500 ps was achieved and within this temporal resolution the thermal expansion was observed to be instantaneous. For the functionality of Bragg-mirrors for an XFELO only the condition of the mirrors at the time when the photon pulse impinges is of relevance. This imposes three timescales for modeling, which have to be considered. Depending on the timescale, different processes have to be considered which have the potential to disturb the reflectivity of the mirrors on arrival of an XFELO pulse.

The first timescale is the duration of an XFELO pulse which is typically < 200 fs. This time is too short for the crystal to respond on the photon pulse with expansion and therefore the reflection of a photon pulse is assumed not to be perturbed by the pulse itself[20]. Under the assumption that the XFELO pulses do not destroy the crystal structure, the mirror should relax to its initial condition after a certain time. This relaxation takes primarily place by heat transfer, but the generation of coherent phonon pulses, which transport energy, too, has also been observed (s. section 3.3).

The second timescale is the repetition time of the photon pulse which would be 220 ns for an XFELO running at the European XFEL. At an early stage when the lattice- and the electron-system are not in equilibrium, heat conduction takes place both by electrons and phonons. This early energy transport can be described by a two temperature model [Shin et al., 2015], where diffusive heat conduction in the lattice- and in the electron-subsystem is assumed. However, the time scale of 220 ns is long compared to the carrier thermalization time in diamond, which is about 500 ps. Therefore, the modeling presented in the following sections assumes an instantaneous electron-lattice thermalization. In the case of heat conduction this amounts to saying that the thermal conductivity of the diamond during the electron-lattice thermalization is assumed to be equal to the lattice thermal conductivity.

The third time scale is the duration of the photon pulse train, which can be assumed to be between 500 µs and CW (continuous wave). On this timescale, vibrations or static

[20] This can be assumed for pulse energies below a certain threshold. Ultrafast phase transitions in silicon for example take place at an electron-hole density of 10^{22} cm^{-3}. By this process significant changes in the crystal structure have been observed to take place within tens of fs [Sokolowski-Tinten and von der Linde, 2004].

deformations of the whole crystal in its mount due to thermal expansion become an issue. The thermal load is distributed over the whole crystal and the question of the heat dissipation from the crystal arises. When considering a heat sink, a low contact resistance along with a low induced mechanical strain is needed.

3.2 Thermal Expansion of Insulators and Semiconductors

When an insulator crystal is subjected to a temperature change the change in the phonon spectrum causes the crystal to expand or to shrink because the potentials in which the atoms are bounded are not purely harmonic and thus their oscillation amplitude and their oscillation frequency are dependent. The majority of materials have a positive temperature coefficient, which means that they expand upon heating. Thermal expansion is a well known effect and its physics can be found in various text books about solid state physics. The derivation of thermal expansion given here can be found in [Ashcroft and Mermin, 2005a]. The relative change of length with temperature of a cubic crystal is described by the equation

$$\beta = \frac{1}{L}\left(\frac{\partial L}{\partial T}\right)_P = \frac{1}{3V}\left(\frac{\partial V}{\partial T}\right)_P = \frac{1}{3B}\left(\frac{\partial P}{\partial T}\right)_V \tag{3.1}$$

where β is the linear expansion coefficient, L is the length, V the volume, P the pressure, T the temperature and B is the bulk modulus of the crystal. The actual length at a given temperature can be determined by solving equation (3.1) for $L(T)$, which yields

$$L(T) = L(T_0)\exp\left(\int_{T_0}^{T} \beta(T')\,\mathrm{d}T'\right). \tag{3.2}$$

For small temperature changes, β can be assumed constant which allows equation (3.2) to be simplified to

$$L(T) = L_0 \exp\left(\beta \Delta T\right). \tag{3.3}$$

This expression in turn can be expanded into a Taylor series and approximated to first order as

$$L \approx L_0(1 + \beta\Delta T) \implies \Delta L \approx \beta L_0 \Delta T. \tag{3.4}$$

For most practical applications the approximation (3.4) is sufficient and is therefore widely used. To obtain an expression for β the pressure used in equation (3.1) can be written as

$$P = \left(\frac{\partial F}{\partial V}\right)_T \tag{3.5}$$

where F represents the Helmholtz free energy which is given by $F = U - TS$. Here, the entropy S and the internal energy U are related by

$$T\left(\frac{\partial S}{\partial T}\right)_V = \left(\frac{\partial U}{\partial T}\right)_V. \tag{3.6}$$

Hence, by using $S = 0$ at $T = 0$, the pressure can be expressed without the entropy as

$$P = -\frac{\partial}{\partial V}\left[U - T\int_0^T \frac{\mathrm{d}T'}{T'}\frac{\partial}{\partial T'}U(T', V)\right]. \tag{3.7}$$

By inserting the Bose-Einstein distribution $n^0_\omega(\boldsymbol{k})$ (equation (3.32)) into the expression for the internal energy of the crystal lattice U_l (equation (3.31)) and inserting U_l into equation (3.7) the pressure yields

$$P = -\frac{\partial}{\partial V}\left[U_\mathrm{l}^\mathrm{eq} + \sum_{\boldsymbol{k},p}\frac{1}{2}\hbar\omega(\boldsymbol{k},p)\right] + \sum_{\boldsymbol{k},p}\left(-\frac{\partial}{\partial V}\hbar\omega(\boldsymbol{k},p)\right)\frac{1}{\exp\left(\frac{\hbar\omega(\boldsymbol{k},p)}{k_\mathrm{B}T}\right)-1}, \tag{3.8}$$

where $\omega(\boldsymbol{k}, p)$ denotes the angular frequency of the phonon with wave vector $\boldsymbol{k}$ and polarization index p. In this equation the first term contributes the derivative of the zero point energy with respect to the volume and at $T > 0$ the second term contributes the derivative of the phonon energies with respect to the volume. In this equation the equilibrium pressure only depends on temperature through the dependence of the frequencies of the normal modes on the equilibrium volume. In a perfect harmonic crystal, where the force constants K do not depend on the displacement (s. equation (3.28)), the frequencies can not depend on the volume. Therefore, just like the thermal conductivity discussed in section 3.4.2, the thermal expansion is an anharmonic effect of the crystal lattice. By inserting equation (3.8) into equation (3.1) the coefficient of thermal expansion is given by

$$\beta = \frac{1}{3B}\sum_{\boldsymbol{k},p}\left(-\frac{\partial}{\partial V}\hbar\omega(\boldsymbol{k},p)\right)\frac{\partial}{\partial T}\frac{1}{\exp\left(\frac{\hbar\omega(\boldsymbol{k},p)}{k_\mathrm{B}T}\right)-1}. \tag{3.9}$$

This equation contains the expression for the volumetric heat capacity at constant volume (cf. equation (3.34)) which can be written as

$$C_\mathrm{l} = \sum_{\boldsymbol{k},p} \frac{\hbar\omega(\boldsymbol{k},p)}{V} \frac{\partial}{\partial T} n^0_\omega(\boldsymbol{k}) = \sum_{\boldsymbol{k},p} c_\mathrm{l}(\boldsymbol{k},p) \tag{3.10}$$

where c_l is the contribution of the normal mode $\boldsymbol{k}$, p to the heat capacity of the lattice C_l at constant volume. In practice the so-called Grüneisen parameter $\gamma_{\boldsymbol{k}p}$ for the mode $\boldsymbol{k}$, p is often used to obtain an expression for β. It is given by:

$$\gamma_{\boldsymbol{k}p} = -\frac{V}{\omega(\boldsymbol{k},p)} \frac{\partial\omega(\boldsymbol{k},p)}{\partial V} = -\frac{\partial(\ln\omega(\boldsymbol{k},p))}{\partial(\ln V)}. \tag{3.11}$$

The entire Grüneisen parameter is defined as the weighted average of the $\gamma_{\boldsymbol{k}p}$ as

$$\gamma = \frac{\sum_{\boldsymbol{k},p} \gamma_{\boldsymbol{k}p} c_\mathrm{l}(\boldsymbol{k},p)}{\sum_{\boldsymbol{k},p} c_\mathrm{l}(\boldsymbol{k},p)}, \tag{3.12}$$

where the contribution to the thermal expansion of each mode is weighted by its contribution to the heat capacity. Using the definition for the entire Grüneisen parameter equation 3.9 can be written as

$$\beta = \frac{\gamma C_\mathrm{l}}{3B}. \tag{3.13}$$

In the Debye model (s. discussion in section 3.4.1) the frequencies of the normal modes scale linearly with the Debye cutoff frequency ω_D. In this case the Grüneisen parameter yields

$$\gamma = \gamma_{\boldsymbol{k}p} = -\frac{\partial(\ln\omega_\mathrm{D})}{\partial(\ln V)} \tag{3.14}$$

In a real crystal the $\gamma_{\boldsymbol{k}p}$ are not equal for all normal modes. Hence, γ is slightly dependent on temperature. However, an estimation of $\beta(T)$ can be obtained from $C_\mathrm{l}(T)$ via equation (3.13) where γ can be calculated at a known $\beta(T_0)$. Figure 3.2 shows a comparison between $\beta(T)$ obtained from equation (3.13) and an empirical formula [Stoupin and Shvyd'ko, 2011] which reproduces measurements of $\beta(T)$ with deviations of less than 3×10^{-8}.

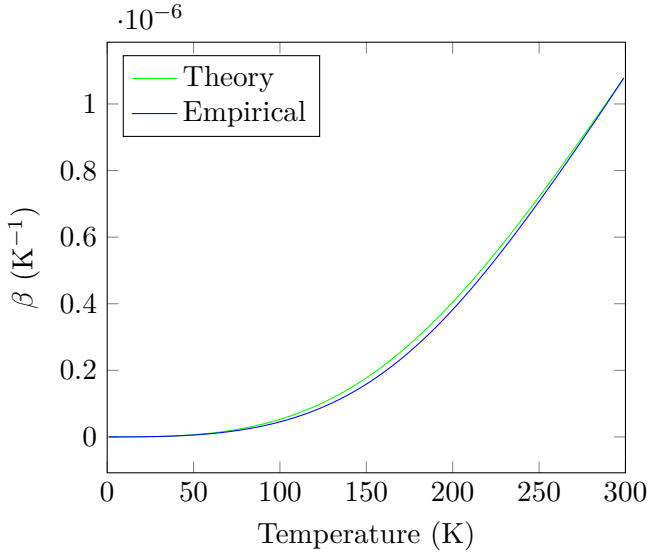

Figure 3.2: The coefficient of thermal expansion of diamond as a function of temperature. Comparison between an empirical formula which reproduces measurements and the theoretical result of equation (3.13). The heat capacity was obtained by equation (3.37).

3.3 Generation of Strain by absorbed Photon Pulses

The generation process of thermal and mechanical strain outlined in this section follows primarily the argumentation given by [Thomsen et al., 1986; Carminati et al., 2006a]. The absorption of a photon pulse and the following conversion to thermal phonons as described in section 3.1 causes the thermal expansion of the material[21] as discussed in section 3.2. To quantify this effect the energy density $W(x,t)$ of the radiation absorbed within the penetration depth of the material can be calculated by [Carminati et al., 2006a]

$$W(x,t) = \frac{\kappa_\nu (1-R) E_\mathrm{p}}{A} \mathrm{e}^{-\kappa_\nu x} \Gamma(t) \tag{3.15}$$

where κ_ν is the absorption coefficient, R is the reflectivity, E_p is the energy of the photon pulse and A is the irradiated area. The function $\Gamma(t)$ represents the Heaviside step function. This one-dimensional model is a reasonable simplification as long as the beam diameter is significantly larger than the thickness of the considered material.

[21] In this discussion the contribution of the photoexcited carriers to the thermal expansion is neglected because in the considered case the acoustic pulse duration is long compared to the carrier lifetime. See [Thomsen et al., 1986] and [Matsuda et al., 2015] for further explanation.

Furthermore, when the photon pulse duration is assumed to be short compared to the time constant of the corresponding heat transfer problem, the temperature rise due to the absorbed energy is given by

$$\Delta T(x,t) = \frac{W(x,t)}{\rho C_\mathrm{p}} \tag{3.16}$$

where C_p is the specific heat capacity and ρ is the mass density. Assuming an isotropic material, this heterogeneous temperature distribution results in a thermal expansion $\Delta L \approx \beta L_0 \Delta T$ which in turn generates thermal stress $\boldsymbol{\sigma}^\mathrm{th}$. In the tensor notation, where the indices i, j, k, l are integers, which label a component of the respective tensor, the thermal stress is

$$\sigma_{ij}^\mathrm{th} = -\sum_{kl} C_{ijkl}\beta_{kl}\Delta T(x,t) = -\beta \Delta T(x,t) \sum_{kl} C_{ijkl}\delta_{kl}, \tag{3.17}$$

where C_{ijkl} is the elasticity tensor, β is the thermal expansion coefficient and δ is the Kronecker delta. For cubic crystals like diamond it can be shown that the elasticity tensor has only three independent elements and it can therefore be reduced to a matrix C_{ij}. In this simplified model introduced above, a temperature gradient only exists in the x direction. Hence, σ_{11} is the only nonzero element of the thermal stress tensor which can then be written as

$$\begin{aligned}\sigma_{11}^\mathrm{th}(x,t) = \sigma_\mathrm{th}(x,t) &= -\beta\Delta T(x,t)(C_{11}+2C_{12}) = -3\beta B \Delta T(x,t) \\ &= -\frac{3\beta B \kappa_\nu (1-R) E_\mathrm{p}}{\rho C_\mathrm{p} A} \mathrm{e}^{-\kappa_\nu x} \Gamma(t) = -\rho {v_\mathrm{s}}^2 \eta_0 \mathrm{e}^{-\kappa_\nu x} \Gamma(t)\end{aligned} \tag{3.18}$$

where $B = (C_{11} + 2C_{12})/3$ is the bulk modulus and v_s is the speed of sound, related to the elastic tensor C_{ij} via $\rho {v_\mathrm{s}}^2 = C_{11}$. The dimensionless parameter η_0 is defined as

$$\eta_0 = \frac{3\beta B \kappa_\nu (1-R) E_\mathrm{p}}{\rho {v_\mathrm{s}}^2 C_\mathrm{p} A}. \tag{3.19}$$

It determines the strain at the crystal surface, induced by the short laser pulse. The strain $\eta_{11}(x,t)$, induced in the material can be related to the displacement u_1 by $\eta_{11} = \partial u_1/\partial x$. Hereinafter, the stress and strain indices 11 and the index 1 of the displacement are omitted for simplicity. The associated stress field in the material can then be written

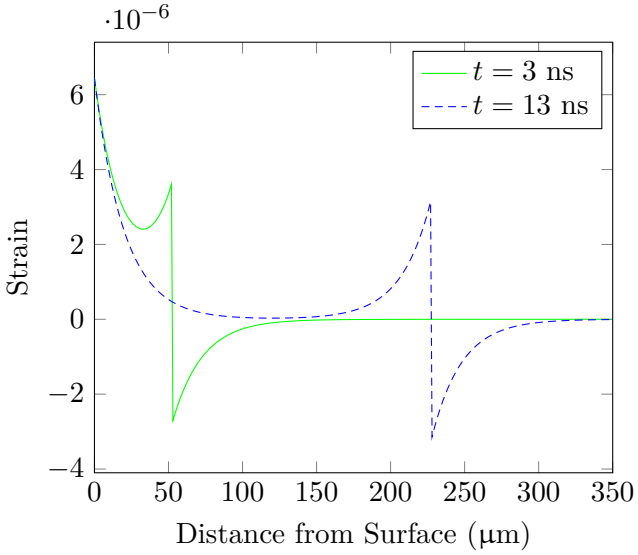

Figure 3.3: Strain profile in a diamond crystal at two different times after generation of the strain. The exponentially decaying strain on the left corresponds to thermal strain and the running pulse to the elastic mechanical strain. The mechanical pulse was generated by an optical pulse with a penetration depth of 20 µm and an energy density of 160 µJ/mm^2. This absorbed energy density corresponds to an absorbed peak energy density of a Gaussian beam with $\sigma = 50$ µm and an absorbed energy of 2.5 µJ.

as the sum of the mechanical stress $\sigma_{11}^{\mathrm{m}} = C_{11}\partial u_1/\partial x = \sigma^{\mathrm{m}}$ and the thermal stress σ^{th}, which yields

$$\sigma(x,t) = \sigma^{\mathrm{m}}(x,t) + \sigma^{\mathrm{th}}(x,t) = \rho {v_{\mathrm{s}}}^2 \frac{\partial u}{\partial x} - \rho {v_{\mathrm{s}}}^2 \eta_0 \mathrm{e}^{-\kappa_\nu x} \Gamma(t). \tag{3.20}$$

Using Cauchy's equation and neglecting body forces[22] leads to the equation of motion of the problem:

$$\rho \frac{\partial^2 u}{\partial t^2} = \frac{\partial \sigma}{\partial x}. \tag{3.21}$$

Inserting equation (3.20) into equation (3.21) gives the equation of propagation for the displacement in the x direction u of the problem:

$$\frac{\partial^2 u}{\partial x^2} - \frac{1}{{v_{\mathrm{s}}}^2} \frac{\partial^2 u}{\partial t^2} = -\eta_0 \kappa_\nu \mathrm{e}^{-\kappa_\nu x} \Gamma(t). \tag{3.22}$$

[22] Forces which act throughout the volume of a body – like gravity for example.

This equation is a wave equation for $u(x,t)$ with a source term and it can also be formulated as an equation for η by applying $\partial/\partial x$ to equation (3.22) since $\eta = \partial u/\partial x$. Solving equation (3.22) or the respective equation for the strain directly results in the strain profile given by

$$\eta(x,t) = \frac{\eta_0}{2}\left[(2 - \mathrm{e}^{-\kappa_\nu v_\mathrm{s} t})\mathrm{e}^{-\kappa_\nu x} - \mathrm{sgn}(x - v_\mathrm{s} t)\mathrm{e}^{-\kappa_\nu |x - v_\mathrm{s} t|}\right], \tag{3.23}$$

where a semi infinite crystal with a stress free surface was assumed as boundary conditions. Figure 3.3 shows the strain distribution of equation (3.23) for 3 ns and 13 ns after the arrival of a 12 keV x-ray pulse in a diamond crystal. The values for the calculation are given in table 3.1. The exponential decay starting at $x = 0$ represents the thermal strain which caused the running pulse of the mechanical (elastic) strain. This pulse is composed of two opposed exponential functions. The shape of the running pulse can be understood by means of the d'Alembert solution of the wave equation which yields for $\partial\eta(x,0)/\partial t = 0$ the solution[23]

$$\eta(x,t) = \frac{F(x - v_\mathrm{s} t) + F(x + v_\mathrm{s} t)}{2}, \tag{3.24}$$

where $F(x,0)$ is a function, which describes the original distortion of the medium, causing the generation of the wave. Thus the thermal strain at the surface of the medium, which has an exponential shape due to the absorption characteristic of the radiation, generates two copies propagating in opposite directions. Because the pulses are generated at the stress free surface, the pulse propagating in the negative x direction experiences a reflection with a reflection coefficient for the strain of -1. This results in the pulse shape shown in figure 3.3. In the present model heat conduction is neglected, which causes the thermal strain to be static. In section 3.4 an introduction to heat transfer is given. If the thermal strain changes while the ultrasonic pulse propagates over the thermally strained area, the pulse shape of the ultrasonic pulse would be distorted. As explained above, the absorption length of the radiation primarily determines the length of the pulse, which in turn determines the exited phonon frequencies. If the center of the propagating strain pulse is taken as $x = 0$ and the strain pulse is also taken as far

[23] This solution is only valid for homogeneous (without a source term) wave equations in one spatial dimension.

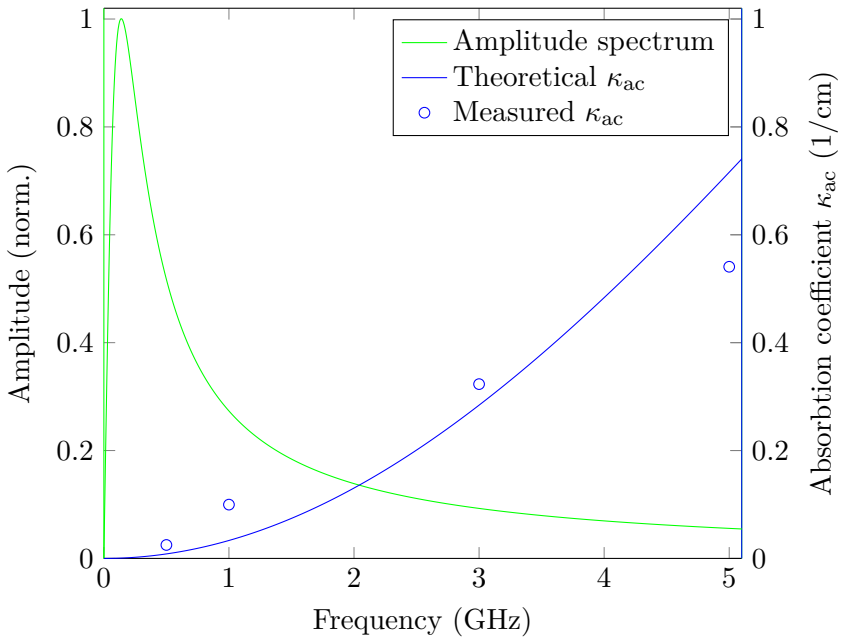

Figure 3.4: Spectral acoustic absorption coefficient of diamond and normalized amplitude spectrum of the laser-excited strain pulse shown in figure 3.3. The amplitude spectrum of the strain pulse was calculated from equation (3.25) and the spectral acoustic absorption coefficient was calculated from the equations (3.26) and (3.27) using the numerical values shown in table 3.1 The measurement data are taken from [Telichko et al., 2015]

from the surface of the crystal, then the temporal Fourier transform of the propagating strain pulse yields [Matsuda et al., 2015]

$$\int_{-\infty}^{\infty} \eta(x,t) \mathrm{e}^{\mathrm{i}\omega t}\, \mathrm{d}t = \eta_0 \frac{\mathrm{i}\omega}{\omega^2 + \kappa_\nu^2 v_\mathrm{s}^2}. \tag{3.25}$$

The relaxation times of the phonons depend on their frequencies and thus the absorption length $1/\kappa_\nu$ of the photon radiation also has an influence on the damping of the acoustic pulse. The attenuation of sound waves in dielectric crystals can be determined by the Boltzmann transport equation (BTE), where the attenuation is described by phonon - phonon scattering [Woodruff and Ehrenreich, 1961]. The spectral acoustic absorption coefficient $\kappa_\mathrm{ac}(\omega)$ [Kaviany, 2014a] is given by

$$\kappa_\mathrm{ac}(\omega) = \frac{\tau c_v \gamma^2 T \omega^2}{2 v_\mathrm{s}^3 \left(1 + 2\omega^2 \tau^2\right)}, \tag{3.26}$$

where τ is the phonon relaxation time, c_v the specific heat at constant volume and γ the Grüneisen parameter (s. equation (3.13)). The phonon relaxation time can be estimated at

$$\tau = \frac{3\lambda_\mathrm{th}}{\rho c_v v_\mathrm{s}^2}, \tag{3.27}$$

where λ_th is the thermal conductivity and ρ is the mass density. Figure 3.4 shows the normalized amplitude spectrum of the laser excited strain pulse shown in figure 3.3 and the spectral acoustic absorption coefficient $\kappa_\mathrm{ac}(\omega)$ of diamond. The amplitude spectrum was obtained from equation (3.25) and the spectral acoustic absorption coefficient was obtained from equation (3.26) using the respective parameters given in table 3.1. The values given in table 3.1 apply to the typical scenario of an XFELO with diamond mirrors.

Due to this final thermalization of the coherent phonon pulse which has its origin in the thermal expansion of the material these strain pulses can be considered as a second channel of highly ballistic thermal energy transport.[24]

3.4 Heat Transfer in Insulators and Semiconductors

The heat transfer in a solid is based on the transport of energy carriers. The principal carriers in a solid are the photon, the electron and the phonon. Depending on the material properties and the environmental conditions (e.g. the temperature or external

[24] See section 3.4.3.2 for more details about ballistic heat transport by phonons.

Table 3.1: Input parameters of the calculations shown in figures 3.3 and 3.4.

Parameter	**Abbr.**	**Unit**	**Value**
Thermal conductivity	λ_{th}	W/(m K)	$1.73 \cdot 10^{3}$
Specific heat	c_v	J/(kg K)	$5.11 \cdot 10^{2}$
Mass density	ρ	kg/m^2	$3.51 \cdot 10^{3}$
Sound velocity	v_{s}	m/s	$1.75 \cdot 10^{4}$
Absorption coefficient	κ_ν	1/m	$5.00 \cdot 10^{4}$
Grüneisen parameter	γ	–	$7.90 \cdot 10^{-1}$
Temperature	T	K	$3.00 \cdot 10^{2}$
Th. expansion coefficient	β	1/K	$1.08 \cdot 10^{-6}$
Bulk modulus	B	Pa	$4.42 \cdot 10^{11}$
Pulse energy	E_{p}	J	$2.50 \cdot 10^{-4}$
Reflectance	R	–	$9.90 \cdot 10^{-1}$
Irradiated area	A	m^2	$1.57 \cdot 10^{-8}$

heat sources which perturb the local thermal equilibrium) the influence of the different carriers to the overall energy transport can vary. The heat current carried by photons can usually be neglected at room temperatures and below [Stein et al., 1981]. In metals the prevailing amount of heat is carried by electrons whereas in semiconductors and insulators the heat is mainly carried by phonons [Majumdar, 1993]. The reason for the different transfer mechanisms are the different electronic band structures which lead to a huge number of free electrons in metals and in semiconductors and insulators (at room temperature and below) to primarily bounded electrons.[25] Since the experiments presented in chapter 5 are conducted with diamond which is an insulator, this chapter will focus on phonon heat transport.

The phonon modes which exist in a particular crystal depend on its lattice system. Diamond for example has a Bravais lattice with a two-point basis. Owing to the linearization of the distance dependent intermolecular forces the different distances between the carbon atoms can be modeled by different spring constants. In one dimension the diamond structure can therefore be represented as a chain of identical masses separated

[25] In the case of pulsed laser irradiation the assumption of primarily bounded electrons is only valid after recombination. Because the time constant of the cooling cycles considered in this work are long compared to the lifetime of free electrons in diamond, as discussed in section 3.1.1, primarily bounded electrons can be assumed.

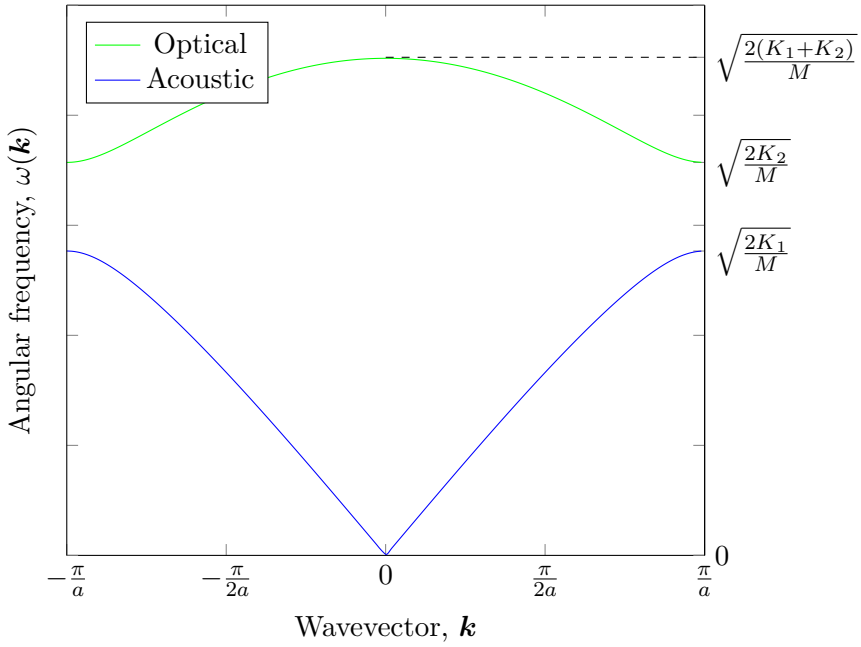

Figure 3.5: Dispersion relation of the phonons in a 1D harmonic FCC crystal lattice with a two point basis (diamond structure).

by springs with two alternating spring constants. The equations of motion for this one dimensional chain are given by

$$M\frac{\mathrm{d}^2 u_n}{\mathrm{d}t^2} = -K_1(u_n - v_n) - K_2(u_n - v_{n-1}) \tag{3.28a}$$

$$M\frac{\mathrm{d}^2 v_n}{\mathrm{d}t^2} = -K_1(v_n - u_n) - K_2(v_n - u_{n+1}) \tag{3.28b}$$

where M represents the mass of the individual atom, u_n and v_n denote the displacement of the first and second atom of the primitive cell n and K_1, K_2 represent the spring constants 1 and 2. The angular frequency ω of the solution as a function of the wavevector $\boldsymbol{k}$, also known as the dispersion relation, can be obtained by taking $\exp(-i\omega t)$ as an ansatz for the time dependence of the solution. By assuming $K_1 < K_2$ the dispersion relation for the one dimensional crystal yields:

$$\omega^2 = \frac{K_1 + K_2}{M} \pm \frac{1}{M}\sqrt{K_1^2 + K_2^2 + 2K_1K_2\cos(\boldsymbol{k}a)} \tag{3.29}$$

The phonon dispersion relation $\omega(\boldsymbol{k})$ is shown in fig. 3.5. It is periodic over the so called Brillouin zones and therefore only plotted for the first Brillouin zone from $-\pi/a$ to π/a. Wavevectors outside of the first Brillouin zone correspond to wavelengths of less than the lattice constant a. Because of the periodicity of the dispersion relation, these solutions are not unique and hence equivalent to the solutions within the first Brillouin zone. The most important information which can be extracted from the dispersion relation is the velocity

$$v_\omega = \frac{\partial \omega}{\partial \boldsymbol{k}} \tag{3.30}$$

of the phonons with the angular frequency[26] ω. The dispersion relation shown in fig. 3.5 possesses two branches – an optical and an acoustic branch. The name acoustic refers to the linear dispersion relation $\omega = v_\mathrm{s}\boldsymbol{k}$ of this branch from acoustic to ultrasonic frequencies where v_s represents the well known speed of sound. The term optical however refers to the high frequencies of these phonons which allow photons at or near the visible spectrum to interact with them. Due to their different propagation speeds acoustic phonons carry the majority of energy so that the contribution of the optical phonons is usually neglected when considering transport properties. However, if the specific heat is considered, both the optical and acoustic branches have to be taken into account. In the three dimensional case the dispersion relation is very similar to the one dimensional case considered here. The effects observed in the one dimensional case hold generally true for the 3D case, but in the 3D case the branches split into three polarization directions and become dependent on the crystal orientation which in turn depends on the respective crystal symmetry.

3.4.1 The Heat Capacity of the Lattice

In the previous sections the term phonon was already used as the quantum of crystal vibrations. This can be justified post hoc by introducing the equation for the internal energy [Ashcroft and Mermin, 2005a, p. 577]

$$U_\mathrm{l} = U_\mathrm{l}^\mathrm{eq} + \sum_{\boldsymbol{k},p} \left[n_\omega^0(\boldsymbol{k}) + \tfrac{1}{2} \right] \hbar\omega(\boldsymbol{k}, p), \tag{3.31}$$

[26] If transport properties are discussed phonons are considered to be localized. One single phonon with one single wave vector can not be localized. To obtain a localized displacement of the atoms in a crystal, phonons resp. eigenmodes with wavevector $\boldsymbol{k} \pm \Delta\boldsymbol{k}$ have to be exited. The resulting wave packet is in analogy to localized electrons also called phonon and localized on the order of $\Delta x \approx 1/\Delta\boldsymbol{k}$

which is composed of $3N$ quantum mechanical harmonic oscillators. Here, n^0_ω is the mean number of phonons at thermal equilibrium, N is the number of atoms in the crystal and p is an index for the respective phonon polarization. The constant U_l^eq represents the contribution to the potential energy of the static equilibrium distribution of the atoms in the crystal lattice. The oscillators in equation (3.31) are not coupled because coupled harmonic oscillators in real space decouple in reciprocal space. Like a single harmonic oscillator, this system has quantized allowable energy levels for a respective eigenmode. In the particle terminology the mean number of phonons with a certain energy represent the amplitude of the respective mode. The allowable energy levels of vibrational modes in a crystal are equivalent to the allowable energy levels of electromagnetic modes in a cavity, which are $(n^0_\omega + 1/2)\hbar\omega$. Therefore, the term phonon is used in analogy to the quantum field theory of electromagnetic fields to describe the vibrational normal modes of a crystal. Because both phonons and photons are bosons, their mean number at a thermal equilibrium temperature T is described by the Bose-Einstein distribution which is given by

$$n^0_\omega(\boldsymbol{k}) = \frac{1}{\exp\left(\frac{\hbar\omega(\boldsymbol{k},p)}{k_\mathrm{B}T}\right) - 1}, \tag{3.32}$$

where $\hbar$ is the reduced Planck constant and k_B is the Boltzmann constant. In the limiting case of a large crystal the equation (3.31) can be simplified by replacing the sum over $\boldsymbol{k}$ by an integral over ω. The specific internal energy of the lattice vibrations[27] is then given by

$$u_\mathrm{l} = \sum_p \int D(\omega) n^0_\omega \hbar\omega \,\mathrm{d}\omega \tag{3.33}$$

where D represents the phonon density of states. The heat capacity of the lattice can now be obtained by applying their thermodynamic definition to equation (3.33) [Kittel, 2004, p. 113] which yields

$$C_\mathrm{l} = \frac{\partial u_\mathrm{l}}{\partial T} = \frac{\partial}{\partial T}\left[\sum_p \int D(\omega) n^0_\omega \hbar\omega \,\mathrm{d}\omega\right]. \tag{3.34}$$

To obtain the phonon density of states the two different models of Debye and Einstein are commonly used. Figure 3.6 shows a comparison between experimental results for the heat capacity of diamond, the classical Dulong-Petit law and the results based on the two quantum mechanical models of Einstein and Debye. In the high temperature limit the models of Einstein and Debye converge to the classical Dulong-Petit result for

[27] omitting the contribution U_l^eq of the static lattice

the heat capacity of $3k_{\mathrm{B}}N = 24.94\ \mathrm{J/(mol\,K)}$. A simple approach, made by Einstein, assumes a flat dispersion relation, where all N harmonic oscillators oscillate at the same frequency $\omega(\boldsymbol{k}) = \omega_0$. The density of states of the Einstein model is therefore given by:

$$D(\omega) = N\delta(\omega - \omega_0). \tag{3.35}$$

For crystals with a diamond structure the Einstein model provides reasonable results because of the presence of optical phonons in diamond structures which are adequately represented by a constant dispersion relation. At low temperatures the model fails because statistically only low frequency phonons are excited which have a density of states of zero in the Einstein model. The more complex Debye model assumes a linear dispersion relation $\omega(\boldsymbol{k}) = v_{\mathrm{s}}\boldsymbol{k}$. In the Debye model the density of states is given by [Kaviany, 2014b]

$$D(\omega) = \frac{V}{2\pi^2 {v_{\mathrm{s}}}^3}\omega^2 \tag{3.36}$$

where V represents the volume of the crystal. Inserting equation (3.36) and equation (3.32) into equation (3.34) and introducing the Debye cut-off frequency ω_{D} the heat capacity yields

$$C_{\mathrm{l}}(T) = \frac{3V\hbar^2}{2\pi^2 {v_{\mathrm{s}}}^3 k_{\mathrm{B}} T^2} \int_0^{\omega_{\mathrm{D}}} \omega^4 \frac{\exp\left(\frac{\hbar\omega}{k_{\mathrm{B}}T}\right)}{\left[\exp\left(\frac{\hbar\omega}{k_{\mathrm{B}}T}\right) - 1\right]^2}\,\mathrm{d}\omega. \tag{3.37}$$

A very common measure in literature is the Debye temperature θ_{D} which can directly be derived from the Debye cut-off frequency by

$$k_{\mathrm{B}}\theta_{\mathrm{D}} = \hbar\omega_{\mathrm{D}} \implies \theta_{\mathrm{D}} = \frac{\hbar\omega_{\mathrm{D}}}{k_{\mathrm{B}}}. \tag{3.38}$$

The Debye temperature is a measure for the highest possible phonon frequency in the crystal and denotes the temperature at which all modes are just excited. For temperatures below 800 K the Debye model is in good agreement with the measured heat capacity of diamond (s. Fig. 3.6) because the vast majority of the phonons excited at those temperatures are low frequency phonons which obey a linear dispersion relation. In the context of this work, only the diamond heat capacity at room temperature and below are of interest and therefore the results produced by the Debye model are sufficiently accurate for all considerations. When required, the accuracy could be increased by combining the Einstein and the Debye model so that the Debye model is only applied

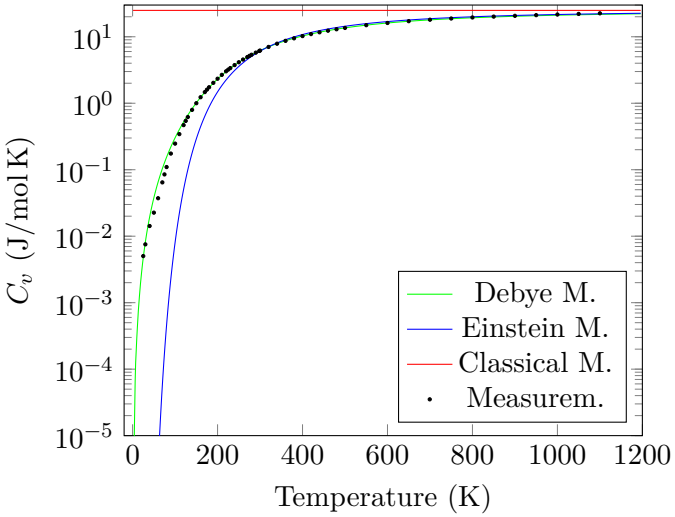

Figure 3.6: Comparison of the heat capacity of diamond with the respective results based on the Debye model, the Einstein model and the classical Dulong-Petit law. The parameters used for the Einstein and Debye model are the Einstein temperature of 1320 K and the Debye Temperature of 1860 K respectively.

to the acoustical branches of the dispersion relation and the Einstein model only to the optical branches.

3.4.2 The Thermal Conductivity of the Lattice

If transport properties are discussed, phonons are considered as localized. One single phonon with one single wave vector can not be localized. To obtain a localized displacement of the atoms in a crystal, phonons respectively eigenmodes with wavevector $\boldsymbol{k} \pm \Delta\boldsymbol{k}$ have to be exited. The resulting wave packet is, in analogy to localized electrons, also called phonon and localized on the order of $\Delta x \approx 1/\Delta\boldsymbol{k}$. An important equation for the understanding of phonon thermal transport was originally derived from the kinetic theory of gases, but it is also applicable to energy carriers in solids when treated as particles [Kittel, 2004, p. 122]. The equation states:

$$\lambda_{\mathrm{th}} = \frac{1}{3} C_{\mathrm{l}} v_{\mathrm{s}} l \tag{3.39}$$

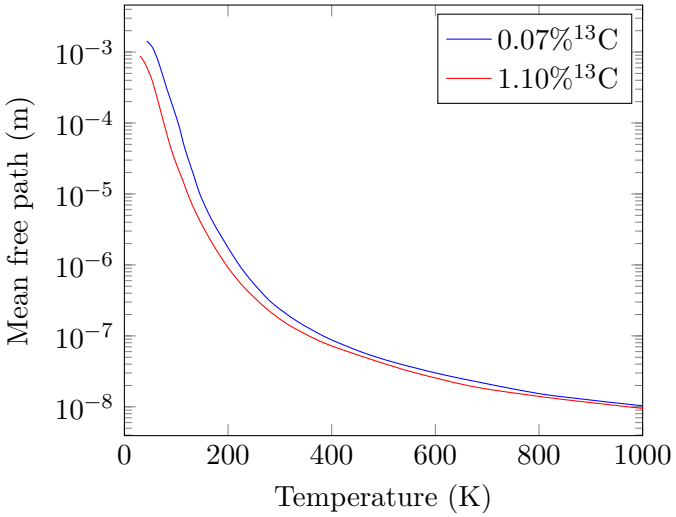

Figure 3.7: Effective mean free path of the phonons in diamond with two different abundances of ^{13}C. The red curve represents natural diamond and the blue curve represents an isotopically purified Diamond with an abundances of ^{13}C of 1.1% and 0.07% respectively.

Here, λ_{th} represents the thermal conductivity, C_{l} the heat capacity per unit volume and v_{s} represents the average group velocity in the direction of the thermal gradient.[28] The expression l represents the average mean free path of the phonons between two collisions, which do not conserve momentum. Collisions with momentum conservation cannot attenuate the phonon flux directly. As shown in figure 3.7 the equation (3.39) can be used for a rough estimation of the mean free path of the phonons by using measured values of λ_{th}, C_{l} and v_{s}. When using the average mean free path approximation it should be kept in mind that the mean free path of phonons has a strong ω-dependence which usually spans several orders of magnitude [Minnich et al., 2011; Wilson and Cahill, 2015] and therefore using this approximation can be very misleading.

The phonon mean free path is in principle determined by two different processes: Geometrical scattering at crystal boundaries, lattice defects and impurities, and carrier scattering, where phonon-phonon scattering is the dominateing carrier scattering process. In a perfect harmonic crystal[29] as described by equation (3.28) a single lattice wave is not attenuated and cannot interact with other waves. Hence, the heat conductivity of

[28] To obtain a value for v_{s} the speed of sound of the one longitudinal mode v_l and the speed of sound of the two transverse modes v_t can be averaged. For diamond with $v_l = 17500$ m/s and $v_t = 12800$ m/s the average group velocity can be estimated at $v_{\text{s}} \approx 1/3(v_l + 2v_t) \approx 14400$ m/s

[29] A crystal with a perfect structure in which only forces linear in the displacement act on the atoms.

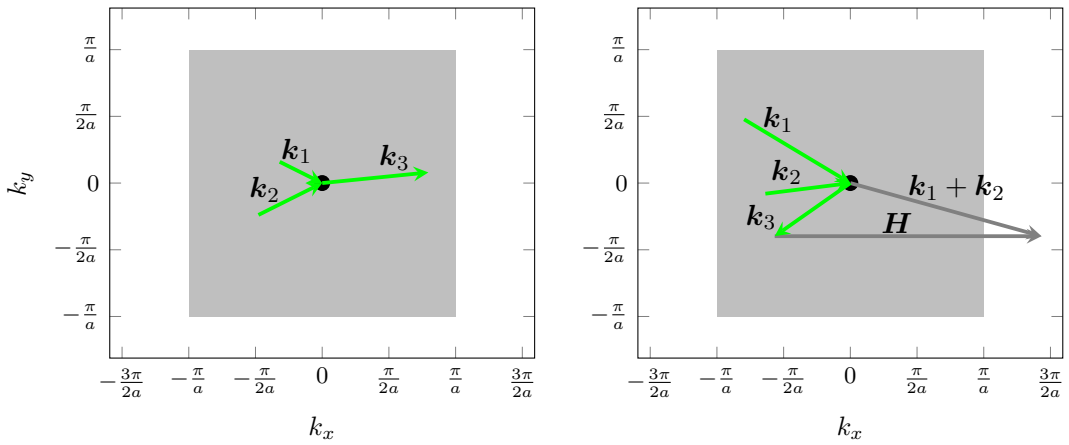

(a) N Process (b) U Process

Figure 3.8: Comparison between the U and N scattering process. The gray squares represent the first Brillouin zone and the black dots represents a point of the reciprocal lattice. See text for further explanation.

such a crystal would be infinite. To explain the effect of phonon scattering, anharmonic terms must be introduced in the interatomic displacements. These anharmonic terms impose a displacement dependency of the elastic constants on the crystal. The presence of one phonon then results in a temporal and spatial modulation of the elastic constants. For a second phonon this modulation acts as a moving grating where it is scattered. As a result a third phonon is created:

$$\boldsymbol{k}_1 + \boldsymbol{k}_2 = \boldsymbol{k}_3^{\mathrm{N}} \tag{3.40}$$

This scattering mechanism in general would still not suffice to establish a local thermal equilibrium and thus a temperature gradient or a thermal resistance in the crystal because the over-all phonon momentum $\hbar\boldsymbol{k}$ would be conserved. This situation is comparable with a flowing gas in a tube with frictionless walls. There, the over-all momentum or energy flux of the gas molecules is conserved because in each collision among the molecules the velocity of the gas center of mass and the averaged energy of all molecules stays constant. For a phonon gas this kind of scattering is referred to as normal process or N process. If only N processes were present in a crystal, the heat transport would be radiative in nature rather than diffusive. To be able to explain the thermal resistance of a crystal, another process, originally discovered by Peierls, exists – the so called umklapp

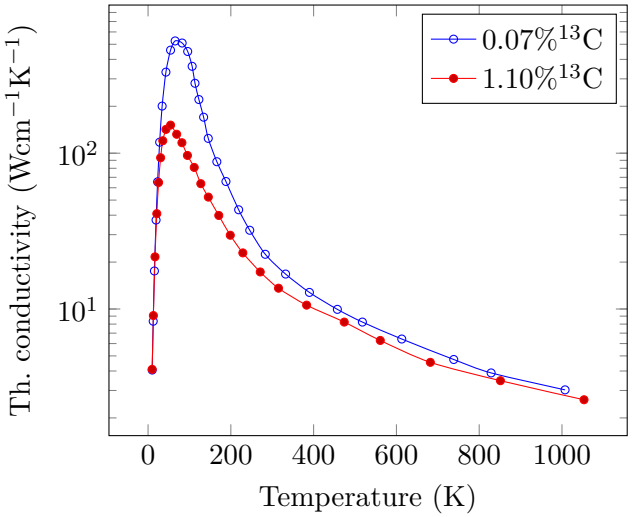

Figure 3.9: Thermal conductivity of diamond with two different abundances of ^{13}C. The red curve represents natural diamond and the blue curve represents an isotopically purified Diamond with an abundances of ^{13}C of 1.1% and 0.07%, respectively. The measurement data are taken from [Graebner, 1995].

process or U process [Ziman, 1960b]. In contrast to the N process described by equation (3.40), the U process

$$\boldsymbol{k}_1 + \boldsymbol{k}_2 = \boldsymbol{k}_3^{\mathrm{U}} + \boldsymbol{H} \tag{3.41}$$

does not conserve the phonon wave vector $\boldsymbol{k}$. Here, $\boldsymbol{H}$ is the reciprocal lattice vector. Equation (3.41) is often referred to as the conservation of quasi-momentum. Because in a crystal only phonons which wavevectors lying in the first Brillouin zone can exist, any $\boldsymbol{k}$ produced in a collision ranging out of the first Brillouin zone must be brought back by addition of $\boldsymbol{H}$. Figure 3.8 shows an illustration and a comparison of the N and U processes. The $\boldsymbol{k}_3^{\mathrm{U}}$ generated in the U process of equation (3.41) travels in the opposite direction of the $\boldsymbol{k}_3^{\mathrm{N}}$ generated in the N process of equation (3.40) and therefore creates a thermal resistance. Because the U processes only take place when $\boldsymbol{k}_1 + \boldsymbol{k}_2$ lies outside of the first Brillouin zone, the probability for the occurrence of a U process is, according to equation (3.32), very temperature dependent. As a result, the mean free pass l for U processes declines sharply with increasing temperatures. Figure 3.9 shows the thermal conductivity for two diamond crystals with different purity. Both show the same temperature dependence. The steep increase of the thermal conductivity at low temperatures originates from the increasing heat capacity (s. Fig. 3.6 and equation (3.39)) at those temperatures. As the temperature increases the U processes set in,

start to compensate and eventually overcompensate for the increasing heat capacity. At temperatures above the Debye temperature of $\theta_D = 1860$ K the heat capacity converges to a constant value, all allowed modes are exited and the overall phonon population increase with temperature. In this temperature region the phonon-phonon mean free path scales according to

$$l_{pp} \propto \frac{1}{T}, \tag{3.42}$$

which results in an inverse T proportionality of the thermal conductivity at high temperatures ($T > \theta_D$), where the heat capacity is constant. Lattice defects and impurities also limit the mean free path of the phonons. Nitrogen for example is the most common chemical impurity in natural diamond. The two curves in Fig. 3.9 show the effect of the ^{13}C content on thermal conductivity of diamond. Here the random distribution of isotopic mass differences disturb the periodicity of the lattice seen by the phonons. However, the expected decrease of the thermal conductivity due to the Rayleigh scattering on the ^{13}C isotopes is only about 1 to 2% and hence cannot explain the large decrease alone. The discrepancy has been attributed to the presence of N processes as to serve to exchange energy between low and high energy modes [Wei et al., 1993; Berman, 1992]. Because the Rayleigh scattering has a strong frequency dependence, the N processes can decrease the mean free path indirectly by increasing the Rayleigh scattering. This normally small effect becomes particularly important for high purity single crystals near the conductivity peak at about 80 K [Wei et al., 1993].

The effects discussed in this section are important basics for the understanding of the heat transfer in the cryogenically cooled cavity mirrors of an XFELO because at low temperatures the mean free path of the principal heat carriers – the phonons – reach the characteristic length scales of the mirrors. In this case the simplifying assumption of purely diffusive heat transport is no longer applicable and thus the heat transfer has to be considered on a microscopic scale. In section 3.4.3 the modeling of the heat transfer on a microscopic scale is discussed.

3.4.3 Modeling the Heat Transfer

To obtain a quantitative description of the heat transfer on the microscopic scale three different methods are commonly used:

1. Continuum models

2. The Bolzmann transport equation [Majumdar, 1998]

3. Molecular approaches, such as lattice dynamics, molecular dynamics and Monte Carlo simulations. [Klitsner et al., 1988; Chou et al., 1999; Tamura et al., 1999]

The continuum models are the simplest approach because they describe the problem on a macroscopic scale. To also take microscale heat transfer effects into account the models can be modified and they are typically applicable as long as meaningful local temperatures can be established. Their advantage are their relatively simple application to real problems due to their usage of macroscopic material constants[30], which can be measured directly. When the Boltzmann transport equation is used, no local thermal equilibrium is needed anymore because instead of a local temperature the equation only depends on the statistical distributions of the energy carriers. The accuracy of the Boltzmann transport equation is however limited by the estimation of its collisional term because its modeling is very difficult and the assumptions to be made lead to an uncertainty. The molecular approaches are conceptually the most fundamental but they suffer from their computational expense and their ultimate limitation due to the uncertain knowledge about the intermolecular forces between the atoms.

Because of the relatively easy application of the continuum models and the questionable added value of the other approaches in the context of this thesis, continuum models and their limitations will be discussed in the following.

3.4.3.1 Derivation of the Heat Equation

In this section it will be shown that, under certain assumptions, the heat equation HE and the hyperbolic heat equation HHE (cf. eq. (3.55)) can be derived from the more general phonon Boltzmann transport equation (BTE).[31] The general form of the phonon BTE states [Carminati et al., 2006b, p. 80]:

$$\frac{\partial n_\omega}{\partial t} + v_\omega \boldsymbol{s} \cdot \nabla n_\omega = \left.\frac{\mathrm{d}n_\omega^0}{\mathrm{d}t}\right|_{\mathrm{col}} \approx \frac{n_\omega^0 - n_\omega}{\tau_\omega} \tag{3.43}$$

Where n_ω is the average number of phonons with angular frequency ω moving in the direction of the unit vector $\boldsymbol{s}$, v_ω is the group velocity of the phonons and n_ω^0 is the equilibrium distribution of the phonons. The right hand side of the the equation is the so called collisional term, which describes the rates of creation and destruction of phonons during collisions. Usually, the collisional term is approximated by the so called

[30] The usually needed material constants heat capacity and thermal conductivity are not very constant with temperature when $T < \theta_\mathrm{D}$, which is shown in Figs. 3.6 and 3.9. This temperature dependence has to be considered when relatively large temperature differences exist in the thermal problem.

[31] A more detailed derivation of the heat equation from the BTE can be found in [Yilbas et al., 2011].

relaxation time approximation because an exact expression is difficult to obtain. In this approximation τ_ω represents the mean free time between collisions of the phonon with angular frequency ω. On length scales larger than the coherence length (typically of the order of some nm), phonons behave like classical particles carrying the energy of $\hbar\omega$. Therefore, in analogy to thermal radiation of photons, a spectral radiative intensity

$$I_\omega(\boldsymbol{r}, t, \boldsymbol{s}) = \sum_p D(\omega) n_\omega(\boldsymbol{r}, t, \boldsymbol{s}) \hbar\omega v_\omega \tag{3.44}$$

can be defined for phonons [Joshi and Majumdar, 1993]. Here, the sum is over the three polarization branches and D is the density of states. When multiplying equation (3.43) by $D\hbar\omega$ the BTE for radiative transfer

$$\frac{1}{v_\omega}\frac{\partial I_\omega}{\partial t} + \boldsymbol{s}\cdot\nabla I_\omega = \frac{1}{\tau_\omega v_\omega}(I_\omega^0 - I_\omega) \tag{3.45}$$

can be obtained. The heat flux is then given by

$$\boldsymbol{q}(\boldsymbol{r}, t) = \int_0^{\omega_{\max}} \int_{4\pi} I_\omega(\boldsymbol{r}, t, \boldsymbol{s}) \boldsymbol{s}\, \mathrm{d}\Omega\, \mathrm{d}\omega \tag{3.46}$$

where the first integral is carried out over a sphere. Hence $d\Omega$ represents the solid angle around $\boldsymbol{s}$. Simplifying this equation by considering the heat current in x-direction and assuming a constant phonon velocity v_s yields

$$q_x(x, t) = 2\pi \int_{-1}^{1} \int_0^{\omega_\mathrm{D}} I_\omega(x, t, \mu)\mu\, \mathrm{d}\omega\, \mathrm{d}\mu \tag{3.47}$$

where the x-component of v_s is expressed by $v_x = v_\mathrm{s}\mu$ and $\mu = \cos(\phi)$. Here ϕ is the angle between the x-axis and the direction of the radiation. Assuming the relaxation time τ_ω as independent of the angular frequency of the phonons, multiplying equation (3.45) by $2\pi\mu$ and performing the same integration as in equation (3.47) on both sides yields [Yilbas et al., 2011]

$$\begin{aligned}\frac{2\pi}{v_\mathrm{s}}\frac{\partial}{\partial t}\int_{-1}^{1}\int_0^{\omega_\mathrm{D}} I_\omega \mu\, \mathrm{d}\omega\, \mathrm{d}\mu + 2\pi \int_{-1}^{1}\int_0^{\omega_\mathrm{D}} \frac{\partial I_\omega}{\partial x}\mu^2\, \mathrm{d}\omega\, \mathrm{d}\mu \\ = \frac{2\pi}{\tau v_\mathrm{s}}\int_{-1}^{1}\int_0^{\omega_\mathrm{D}} \mu I_\omega^0\, \mathrm{d}\omega\, \mathrm{d}\mu - \frac{2\pi}{\tau v_\mathrm{s}}\int_{-1}^{1}\int_0^{\omega_\mathrm{D}} I_\omega \mu\, \mathrm{d}\omega\, \mathrm{d}\mu.\end{aligned} \tag{3.48}$$

When the mean free path of the heat carriers τv_s is small compared to the characteristic length scales L of the medium (i.e. temperature profiles or dimensions of the medium),

the heat transfer is diffusive. In the diffusive regime the intensity can be expanded into a Taylor series

$$I_\omega = I_0 + \frac{\tau v_\mathrm{s}}{L} I_1 + \left(\frac{\tau v_\mathrm{s}}{L}\right)^2 I_2 + \cdots \tag{3.49}$$

which allows to first order for the approximation [Kittel, 2004]

$$\frac{\partial I_\omega(x,t)}{\partial x} \approx \frac{\partial I^0_\omega(T(x,t))}{\partial x} = \frac{\partial I^0_\omega(T(x,t))}{\partial T}\frac{\mathrm{d}T}{\mathrm{d}x}. \tag{3.50}$$

Using the relations $v_x = v_\mathrm{s}\mu$ and $v^2 = v_x^2 + v_y^2 + v_z^2 \approx 3v_z^2$ and using approximation (3.50) by inserting into the second term on the left hand side of equation (3.48) yields

$$\frac{1}{v_\mathrm{s}\tau}\frac{\mathrm{d}T}{\mathrm{d}x}\frac{2\pi}{3}\int_{-1}^{1}\int_0^{\omega_\mathrm{D}} \tau v_\mathrm{s}\frac{\partial I^0_\omega}{\partial T}\,\mathrm{d}\omega\,\mathrm{d}\mu = \frac{1}{v_\mathrm{s}\tau}\frac{\mathrm{d}T}{\mathrm{d}x}\lambda_\mathrm{th} \tag{3.51}$$

where λ_th is defined as the thermal conductivity. Inserting equation (3.47) into the first term on the left hand side and into the second term on the right hand side of equation (3.48) and using relation (3.51) derived for the second term on the left hand side of equation (3.48), then equation (3.48) can be written as

$$\tau\frac{\partial q_x}{\partial t} + q_x = -\lambda_\mathrm{th}\frac{\mathrm{d}T}{\mathrm{d}x}. \tag{3.52}$$

The first term on the right hand side of (3.48) is equal to zero because it is an asymmetric function integrated over a symmetric interval. Equation (3.52) is called Catteneo's equation [Cattaneo, 1958; Joseph and Preziosi, 1989]. When the time scale of interest is much larger than the mean phonon relaxation time τ, the first term of equation (3.52) can be neglected and the remaining part of the equation is equivalent to Fourier's law. Introducing the energy conservation relation

$$C_\mathrm{l}\frac{\partial T}{\partial t} + \frac{\partial q_x}{\partial x} = 0 \tag{3.53}$$

where C_l is the volumetric specific heat, differentiating equation (3.52) with respect to x and substituting the last expression of that derivative into equation (3.53) yields

$$C_\mathrm{l}\frac{\partial T}{\partial t} - \lambda_\mathrm{th}\frac{\mathrm{d}^2T}{\mathrm{d}x^2} - \tau\frac{\partial^2 q_x}{\partial x\partial t} = 0. \tag{3.54}$$

By differentiating equation (3.53) with respect to t, rearranging the terms and inserting it into equation (3.54), the so called hyperbolic heat equation (HHE)

$$\tau \frac{\partial^2 T}{\partial t^2} + \frac{\partial T}{\partial t} = \frac{\lambda_{\mathrm{th}}}{C_{\mathrm{l}}} \frac{\mathrm{d}^2 T}{\mathrm{d}x^2} \tag{3.55}$$

can be obtained [Majumdar, 1993]. Here again, when the mean phonon relaxation time τ is much shorter than the timescale of interest, the first term of equation (3.55) can be neglected and the HHE reduces to the ordinary heat equation (HE).

3.4.3.2 Ballistic limits of the Heat Equation

The classical heat equation is widely used in analyzing heat conduction experiments like transient thermal gratings or frequency and time-domain thermoreflectance, respectively [Käding et al., 1995; Cahill et al., 2002]. The reason for that is its simple applicability and its computational efficiency compared to rigorous approaches such as the BTE, which can be computationally too demanding for routine analysis of experiments [Maassen and Lundstrom, 2016].

So far, the bulk thermal properties have been discussed. In this discussion an infinite crystal was implied through the definition of transport coefficients (i.e. thermal conductivity) which are independent of shape and size of the specimen. Although the microscopic description of the heat transport is very complex, it can be described on a macroscopic scale on the basis of relatively simple diffusion equations[32] using these transport coefficients. This diffusion equation relies on the mathematical law of large numbers in that way as it represents the large-scale long-time approximation of a microscopic random walk under a temperature gradient. Therefore, the applicability of diffusion equations is only unrestricted as long as the considered distances cover many mean free path lengths and the considered intervals endure many relaxation times. For practical purposes this condition is already satisfied within only a few mean free paths and relaxation times, respectively [Ziman, 1960a]. The well known Fourier diffusion equation is usually applied to describe heat conduction in solids. At room temperature, Fourier theory has been successfully applied down to µm length scales and ns time scales [Wilson and Cahill, 2015]. However, at length and time scales comparable to the mean free path and relaxation time, respectively, the transport regime of the phonons becomes quasi-ballistic and the Fourier equation begins to fail [Minnich et al., 2011]. Since the mean free path of the phonons has a strong temperature dependence, at low tem-

[32] The Fourier equation and Cattaneo's equation and the associated heat equations (the HE and the HHE).

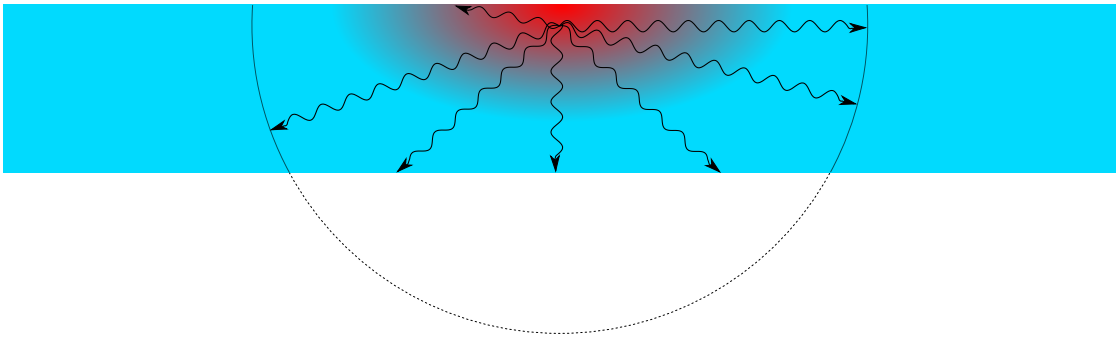

Figure 3.10: Illustration of the boundary scattering effect. The circle depicts the undisturbed average mean free path of the phonons and the color gradient represents a temperature gradient. See text for further explanation.

peratures quasi-ballistic heat transport can already occur on mm length scales. When heat transport in a crystal becomes quasi-ballistic, two different size effects arise, which diminish the predictive power of Fourier theory.

The first effect, illustrated in figure 3.10, is the boundary scattering of the phonons [Casimir, 1938]. Boundary scattering occurs when the mean free path becomes comparable to the crystal dimensions. Due to the freeze-out of umklapp processes at low temperature, for example, scattering occurs less in the bulk and more at the crystal boundaries. This scattering leads to a reduction of the mean free path compared to the bulk value and hence (usually) to a reduction of the thermal conductivity of the crystal. As a result, the thermal conductivity becomes dependent on the crystal dimensions which contradicts the assumption of Fourier theory that the thermal conductivity is a material constant. Several approaches were presented[33] to consider this size effect by introducing an effective thermal conductivity λ_{eff}. A measure for the degree of ballistic transport is the Knudsen number $Kn = l_{\text{b}}/L$, where L represents the characteristic length scale[34] of the system and l_{b} the bulk mean free path. Assuming diffusive scattering at the boundary and $Kn^{-1} \gg 1$, a relatively simple expression under the gray approximation[35] could be derived [Flik and Tien, 1990; Majumdar, 1993], viz

$$\frac{\lambda_{\text{eff}}}{\lambda_{\text{b}}} = \frac{1}{1 + \frac{Kn}{\alpha}}, \tag{3.56}$$

[33] [Zhang, 2007; Flik and Tien, 1990; Majumdar, 1993; McGaughey et al., 2011]
[34] In the case of a thin crystal L would represent the thickness of the crystal whereas in case of a wire L would represent its diameter.
[35] A single, mode independent phonon velocity and relaxation time.

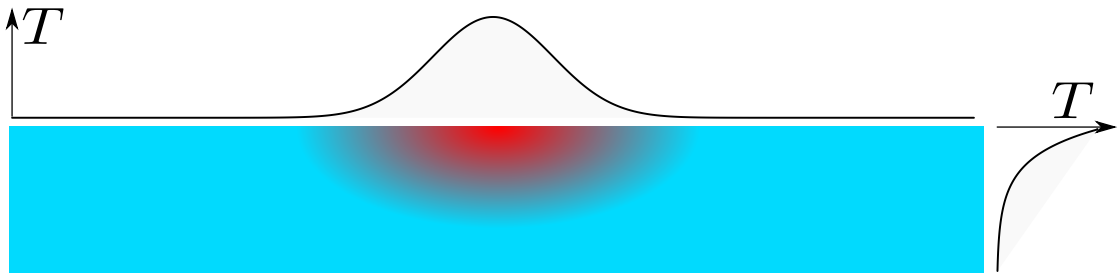

Figure 3.11: Temperature gradient in a crystal after pulsed laser heating. The graphs at the top and the side illustrate the temperature profile in the respective direction of the crystal.

where α is a parameter which depends on the geometry of the sample and the direction of heat flow. For a thin layer, [Majumdar, 1993] found α to be $^8/_3$ and $^3/_4$ for the in-plane and cross-plane direction, respectively. For simple geometries these gray models provide convenient algebraic expressions but they tend to over-predict the rate at which λ_{eff} approaches λ_{b} when Kn approaches zero [McGaughey et al., 2011]. The reason for that is that gray models neglect the influence of the mode dependent mean free path of the phonons which can span orders of magnitude [Sellan et al., 2010]. Making an exact prediction of the boundary scattering effect is difficult because the exact mean free path spectrum of a material is usually not available and the condition of the boundary[36] is usually also unknown. Because the mean free path can span orders of magnitude, it is hard to predict whether a certain phonon is reflected specularly or diffusely. This effect has an additional temperature dependence because the phonon distribution in the crystal strongly depends on temperature. For that reason, an accurate modeling of the boundary effect is hard to achieve [Maldovan, 2012; McGaughey et al., 2011].

The second size effect which reduces the predictive power of Fourier's law is the "gradient effect" of the temperature field. This effect occurs, as presented in figure 3.11 and 3.12, when the gradient of the temperature field in the crystal varies rapidly over length scales which are of the order of the mean free path of the phonons [Ashcroft and Mermin, 2005b; Wilson and Cahill, 2015]. This rapidly varying temperature gradient causes the heat conduction to become ballistic, but due to the mean free path spectrum, which spans over orders of magnitude, this effect does not cause an abrupt failure of Fourier theory. As presented in figure 3.12, Fourier theory fails because its prediction of the heat current in the ballistic and quasi ballistic case is wrong. The reason for that is the first

[36] The boundary can be "black", diffusely or specular, reflecting or something in between. Whether a boundary reflects specular or diffusive depends on their roughness compared to the respective phonon wavelength.

order Tailor-series approximation where Fourier's law relies on. This approximation fails in cases where the temperature gradient varies fast compared to the phonon mean free path. To model the heat transfer in this regime, a ballistic/diffusive model was introduced [Wilson and Cahill, 2014]. The model is based on the idea that high wavevector phonons contribute the vast majority to the material's heat capacity while their mean free path is usually short (compared to low wavevector phonons) so that they can be assumed to be diffusive ($l_{\mathrm{pp}}(\boldsymbol{k}_0) \ll L$) whereas the low wavevector phonons ($\boldsymbol{k} < \boldsymbol{k}_0$) are ballistic. As a result, the mean occupation of the high wavevector phonons can be described by a single temperature field. This resulting thermal reservoir transports heat diffusive for ($\boldsymbol{k} > \boldsymbol{k}_0$) and ballistic for ($\boldsymbol{k} < \boldsymbol{k}_0$).[37] In this ballistic/diffusive model [Wilson and Cahill, 2014] the heat current is expressed as

$$\boldsymbol{q}(\boldsymbol{r}) = -\lambda_{\mathrm{th}}^{0} \nabla T(\boldsymbol{r}) + \sum_{p} \sum_{\boldsymbol{k}<\boldsymbol{k}_0} \boldsymbol{q}_{\mathrm{NL}}(l_{\mathrm{pp}}(\boldsymbol{k}), \boldsymbol{r}), \tag{3.57}$$

where $\lambda_{\mathrm{th}}^{0}$ represents the fraction of thermal conductivity contributed by the diffusive phonons ($\boldsymbol{k} > \boldsymbol{k}_0$), $\boldsymbol{q}_{\mathrm{NL}}$ is the non-local heat current due to ballistic phonons with ($\boldsymbol{k} < \boldsymbol{k}_0$) and $\boldsymbol{k}_0$ is the wavevector which separates the high and low wavevector phonons. When the timescale of interest is much longer than the relaxation time of the phonons, for the one dimensional case, the nonlocal heat current yields,

$$\boldsymbol{q}_{\mathrm{NL}}(k) = \frac{v_k}{2} C_{\mathrm{l}}(k) \Delta T_{\mathrm{avg}}(k), \tag{3.58}$$

where T_{avg} represents the average temperature difference between phonons with MFP $l_{\mathrm{pp}}(k)$ traveling in positive and negative direction. As shown in figure 3.12 this average temperature can be expressed in the gray approximation ($l_{\mathrm{pp}} = \text{const.}$) as

$$\Delta T_{\mathrm{avg}}(x, l_{\mathrm{pp}}) = T(x - l_{\mathrm{pp}}) - T(x + l_{\mathrm{pp}}), \tag{3.59}$$

since on average the phonons which scatter at x have scattered at $x \pm l_{\mathrm{pp}}$ before. When the variation of the temperature gradient is slow compared to the phonon MFP, then equation (3.59) can be approximated as

$$\Delta T_{\mathrm{avg}}(x, l_{\mathrm{pp}}) \approx -2 l_{\mathrm{pp}} \nabla T \tag{3.60}$$

[37] The definition of high- and low-wavevector phonons depends on the considered problem. The value of $\boldsymbol{k}_0$ has to be chosen so that the high-wavevector phonons have a mean free path, which is much shorter than the length scales of the temperature profile. Typical values for $\boldsymbol{k}_0$ are $0.4\boldsymbol{k}_{\mathrm{max}}$ - $0.25\boldsymbol{k}_{\mathrm{max}}$. See [Wilson and Cahill, 2014] for more details.

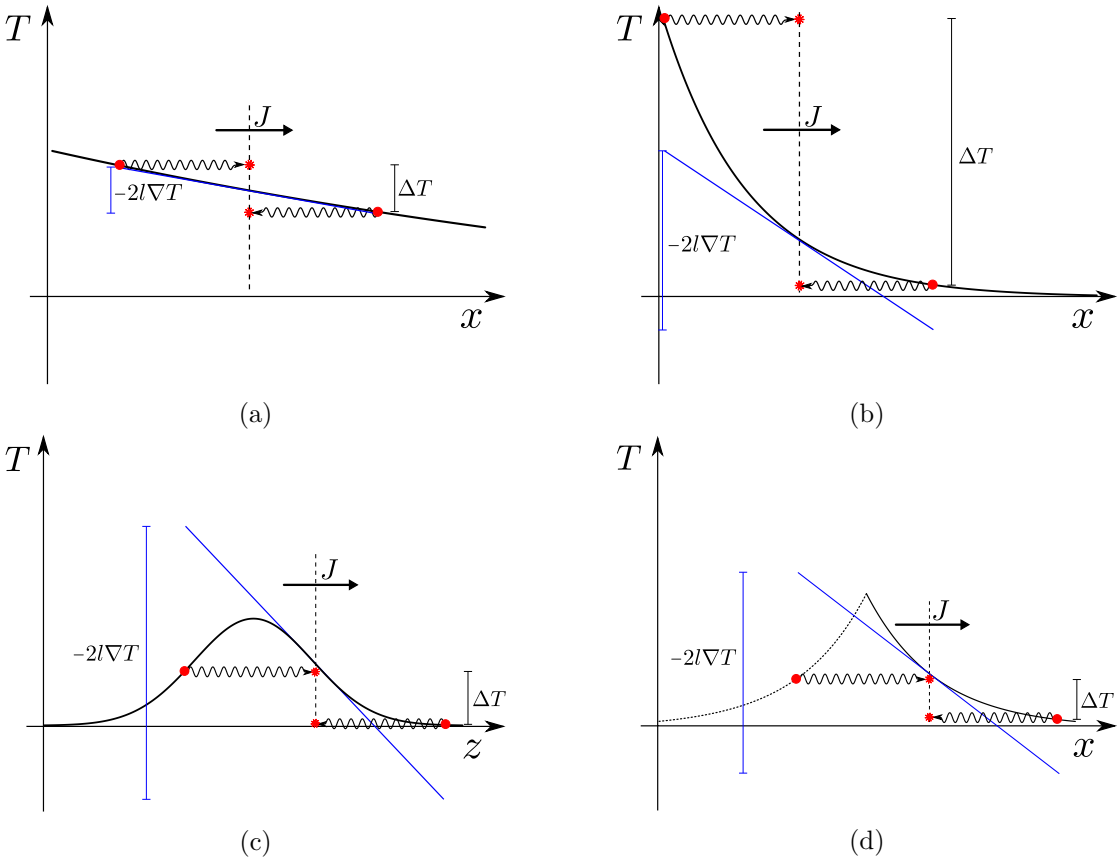

Figure 3.12: Illustration of the gradient effect. The figures show different characteristic temperature profiles. The blue dimension lines represent the first order approximation for ΔT and the black dimension lines represent the true ΔT. The dashed line depicts the point where the heat current is evaluated and the two incoming phonons scatter. The temperature difference is evaluated at the average origin of the two incoming phonons scattering at the dashed line. (a) Example for a temperature profile where the first order approximation for ΔT is adequate. (b,c) Typical in-plane and cross-plane temperature profiles of a laser irradiated solid. The exponential shape of the temperature profile (cross-plane) in (b) is caused by the absorption characteristic of the radiation and the Gaussian (in-plane) temperature profile in (c) is caused by the intensity profile of the radiation, which is typically Gaussian. Here the the first order approximation is invalid. (d) Cross-plane temperature profile where the phonon is reflected at the surface of the crystal. The dotted line represents the temperature profile mirrored at the surface of the crystal. Here, the first order approximation is also invalid. The figure is modified from [Wilson and Cahill, 2014].

and equation (3.58) reduces to Fourier's law. This implies that within the ballistic/diffusive model Fourier's law predicts the correct heat current when equation (3.60) represents an appropriate approximation.

An alternative approach to treat ballistic heat transport was recently proposed by [Maassen and Lundstrom, 2014, 2015] and in a similar way by [Regner et al., 2014]. Maassen and Lundstrom used the so called McKelvey-Schockley flux method (MSM), which was originally developed for the description of electron transport, and adapted it to phonon heat transport.The McKelvey-Schockley flux equations can be derived from the Boltzmann transport equation (BTE) [Rhew and Lundstrom, 2002] and hence they are applicable on all length and time scales where the BTE is valid. As opposed to the BTE the MSM discretises the phonon flux into a forward and a backward stream instead of accounting for phonons traveling in all directions. This simplification significantly reduces the computational expense and enables analytic solutions. With $F^{\pm}(x,t,\epsilon)$ being the phonon flux in the positive and negative direction, respectively, the McKelvey-Schockley flux equations yield

$$\frac{1}{v_x}\frac{\mathrm{d}F^{+}}{\mathrm{d}t}+\frac{\mathrm{d}F^{+}}{\mathrm{d}x}=-\frac{F^{+}}{l_x}+\frac{F^{-}}{l_x} \tag{3.61a}$$

$$-\frac{1}{v_x}\frac{\mathrm{d}F^{-}}{\mathrm{d}t}+\frac{\mathrm{d}F^{-}}{\mathrm{d}x}=-\frac{F^{+}}{l_x}+\frac{F^{-}}{l_x} \tag{3.61b}$$

where $v_x(\epsilon)$ represents the average x-projected phonon velocity, $l_x(\epsilon)$ is the MFP for backscattering along the x-direction and ϵ is the phonon energy. The equations (3.61) are of first order in the spatial and time coordinates and therefore, they can be solved by specifying one initial and one boundary condition. In this case the boundary condition corresponds to specifying the injected phonon flux at the (crystal) boundaries and the initial condition corresponds to specifying the phonon flux at a given time. The resulting solutions cover ballistic effects and show good agreement with the solutions of the phonon BTE while requiring significantly less computation. Besides these considerations the probably most interesting result of [Maassen and Lundstrom, 2014, 2015] is that the McKelvey-Schockley flux equations (3.61) can be rewritten without approximation, as the Cattaneo equation (eq. (3.52)) and the HHE (eq. (3.55)) and in the steady state case as Fourier's law and the HE, respectively.

All of these equations were derived from the BTE in section 3.4.3.1 under the assumption of diffusive heat transfer. In the derivation of the HE and the HHE from the MSM it is shown that no such assumptions are needed which explains why diffusion

equations work well in some situations when ballistic effects are present. By considering the equivalence between the McKelvey-Schockley flux equations and the diffusion equations it turns out that the key to capturing ballistic effect is to also use the (physical correct) boundary conditions of the McKelvey-Schockley flux equations for the diffusion equations. In this case both the diffusion equations and the McKelvey-Schockley flux equations yield the same results. Therefore, [Maassen and Lundstrom, 2016] conclude that the range of problems that can be addressed with diffusion equations is much broader than has been generally understood.

To summarize, in this section an overview of the current state of research in the field of ballistic phonon transport was given. The focus of this overview was on methods which are computationally relatively cheap and which can be used to analyze raw data to extract thermal properties of specimens. This focus was chosen because the measurements presented it chapter 5 impose the requirement for routine analysis of transient experimental data.

3.5 Conclusion

As outlined in this chapter the effects caused by the pulsed Laser irradiation are complex and only understood to some extent. Especially the thermalization dynamics of the involved carriers is a field where quantitative predictions from theory are only reliable for routine applications (well known materials at usual conditions). In the case of an XFELO cavity the question of the maximum acceptable heat load is a major issue where phonon thermalization plays the most important role. In order to maximize the acceptable heat load, thin diamond plates at about 50 K are considered as the most promising mirror material. Predicting the thermalization dynamics of a thin diamond plate at 50 K is not a routine application of the theory and can therefore not reliably be done. As described in section 3.4.2 and 3.4.3.2 the main unknowns that cause the leak in reliability are the unknown mean free path spectrum of the phonons and how this unknown spectrum of phonons interact with the surface of the crystal, which is also not in a perfectly known condition.[38] In order to determine a reliable threshold for the acceptable heat load on the mirrors, a measurement under conditions, which are as close as possible to the real conditions in an XFELO, is necessary. Based on this information numerical simulations can be confirmed and used for further development of the mirrors and additionally, prototypes of mirrors can directly be tested and improved. A measurement setup, which is used not only for a single measurement but for development

[38] Primarily the roughness of the surface determines the interaction with phonons.

purposes, should ideally involve only standard laboratory equipment and no devices like an XFEL or a synchrotron radiation source, where beam time is very rare. In chapter 5 the development of such a measurement setup along with the related first measurements is presented.

4 Numerical Studies

Building an XFELO requires components which have to perform on the edge of today's technological feasibility, including the production and acceleration of high-brightness electron beams, the optimization of radiation generation in the undulator and the electron and x-ray beam guidance so as to overlap the electron bunch with the x-ray pulse to obtain optimal FEL gain. In this chapter various numerical studies addressed to some of these aspects are presented. The goal of these studies is to investigate the feasibility of an XFELO in terms of technical challenges and physical limitations. In section 4.1 the required electron optics to match the x-ray and electron beam is considered. In section 4.2 the influence of angular, positional and, above all, arrival time jitter of the electron beam is investigated. In section 4.3 the influence of absorbed radiation on the Bragg reflection is considered. Section 4.1 and 4.2 have already been published as a conference paper [Maag et al., 2012, 2015].

4.1 Electron Optics

In an XFELO the optical axis has to coincide with the undulator axis. Hence, depending on the design of the XFELO cavity some or all optical elements are located on the undulator axis. In order to bypass the x-ray optical elements with the electron beam and match it with the Gaussian x-ray beam in the undulator, a magnetic chicane or the like and a focusing section are required. To obtain the requirements for the magnets and the dimensions of such a system a respective magnetic chicane and focusing section are considered below.

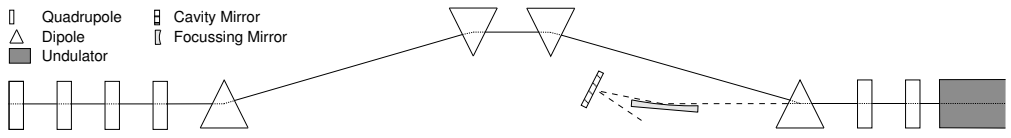

Figure 4.1: The scheme of the beamline. The black line represents the electron beam and the dotted line represents the x-ray beam. The shown mirrors are a part of the cavity. See figures 1.1 and 1.2 for an overview of the whole XFELO setup.

Table 4.1: Beam Parameters

Parameter	**Value**
Electron energy	17.5 GeV
Bunch charge	1 nC
Bunch length (FWHM)	178 fs
Slice emittance (normalized)	1 µm
Slice energy spread	0.45 MeV

4.1.1 Layout of the optical system for the Electron Beam

The layout of the chicane and the focusing section is mainly determined by the required offset of the electron beam and by the desired Twiss-parameters inside the undulator. The offset has to be sufficient for the electrons to pass by the mirrors of the FELO cavity. Due to the relatively small diameters of the x-ray and electron beam, both in the range of tens of µm, and the arrangement of the x-ray optics, an offset of 10 mm is sufficient. That allowed to design a chicane of 21 m length with a deflection angle of 0.1° without any focusing elements in between. Because of the symmetry of the chicane the dispersion is compensated automatically. In order to overlap the Gaussian x-ray and the electron beam inside the undulator properly, a round electron beam with the waist in the middle of the undulator is required. In addition it is desired to keep the beta functions small to reduce beam distortions due to field errors of the magnets. It was investigated if these requirements are met by the scheme shown in Fig. 4.1. The focusing into the undulator is performed by quadrupoles before and after the chicane. With the deflection angle θ of 1.74 mrad (0.1°) and a correlated relative energy spread $\Delta E/E$ of the electrons of about $3 \cdot 10^{-4}$ (see figure 4.4) the path length difference ΔL experienced by high and low energy electrons when traversing the chicane, can be approximated as [Jaeschke et al., 2015, p. 106]

$$\Delta L \approx L\theta^2 \Delta E/E, \tag{4.1}$$

where L is the total length of the chicane. Evaluating equation (4.1) yields a path length difference of about 20 nm. Comparing the path length difference of about 20 nm with the total bunch length of about 40 µm shows, that compression effects of the bunches are negligible for this chicane.

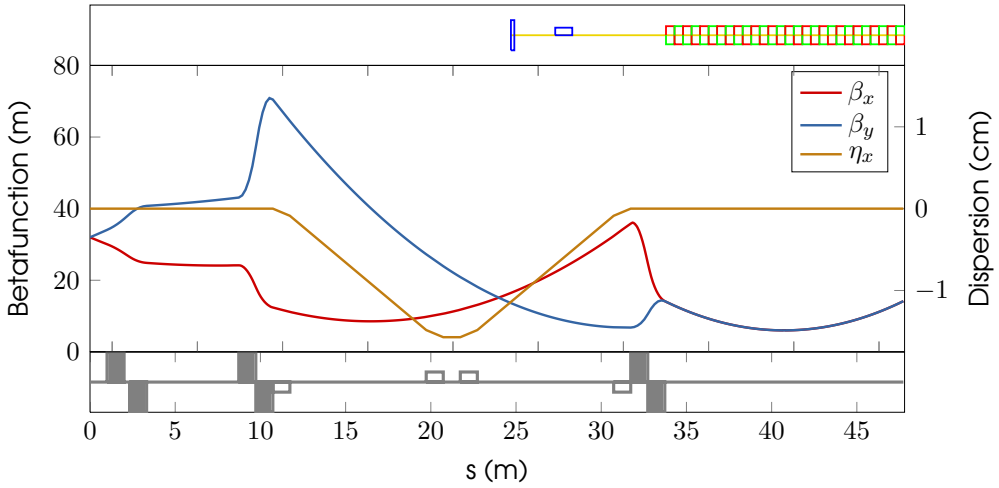

Figure 4.2: The beta functions and the dispersion of the beamline. In the upper part the undulator and the x-ray mirrors are shown. In the lower part the arrangement of the quadrupole (bold) and dipole magnets (normal) are shown.

4.1.2 Simulations

The calculation of the electron optics were performed by using the code Elegant [Borland, 2004]. The underlying beam parameters are shown in table 4.1. The initial α- and β-values were taken from the European XFEL lattice design at a position, suitable to install an XFELO. In order to get the required beam profile inside the undulator an optimization problem with the quadrupole strengths as the variables had to be solved. The conditions of the optimization were constrained in the middle of the undulator to: $\alpha_x = \alpha_y = 0$, $\beta_x = \beta_y = 6\text{m}$. This choice of Twiss-parameters represent an optimum trade-off between an appropriate electron density throughout the undulator and a reasonable x-ray energy density on the Bragg mirrors. In order to simplify the optimization process the contribution of the natural focusing of the undulator to the overall focusing strength was determined by [Wiedemann, 2007, p. 139]

$$\frac{1}{f_y} = \frac{K^2}{2\gamma^2} k_\mathrm{u}^2 L_u, \tag{4.2}$$

where f_y is the focal length of the undulator in the direction normal the plain of the sinusoidal motion of the electrons, K is the undulator parameter (cf. eq. (2.7)), k_u the undulator wave number, γ the Lorentz factor of the electrons and L_u the length of the undulator. Given an undulator parameter of 2, an undulator wave number of $2\pi/0.03$

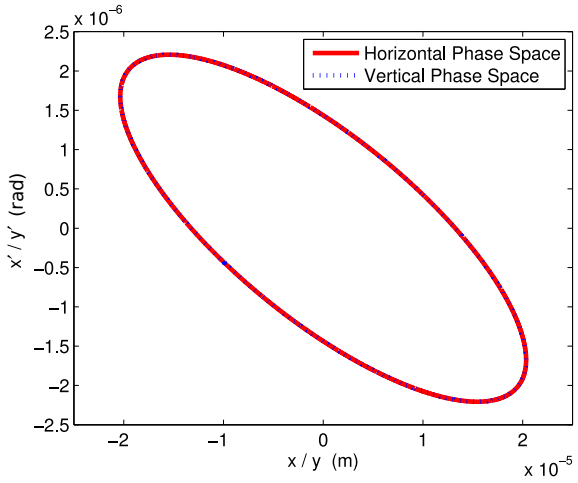

Figure 4.3: One-σ phase space ellipses of the electron beam in the transversal phase space at the entrance of the undulator. For the electron beam parameters, see table 4.1

m^{-1} and an undulator length of 15 m the focal length of the undulator yields about 890 m. Because this focal length is much bigger than the distance of 7.5 m between the undulator entrance and the electron beam waist the natural focusing of the undulator was neglected and the undulator was assumed as a drift space in the optimization procedure. The simplification of replacing the the undulator by a drift space was also validated by numerical simulations [Zemella et al., 2012]. Figure 4.2 shows the result of the optimization. It can be seen that the beam is transformed into a round shape at the entrance of the undulator and has the beam waist in the middle of the undulator. This beam profile also meets the requirement defined above to overlap the electron beam with the Gaussian x-ray beam. It can also be seen that the dispersion returns to zero after the chicane. It is important to enter the undulator without dispersion to keep the beam diameter small and hence overlap the electron beam with the x-ray beam properly. Furthermore, Fig. 4.2 shows in the upper part the dimensions of the undulator and the x-ray optics and in the lower part the arrangement of the magnets along the beamline. After setting up the electron optics, 500000 particles were tracked through the beamline. Figure 4.3 shows the 1σ ellipses in the transversal phase space for the x- and y-direction at the entrance of the undulator, respectively. As shown, the ellipses are identical as it could be anticipated from Fig. 4.2. Figure 4.4 shows the 1σ ellipse of the longitudinal phase space distribution for the beginning of the beamline and for the entrance of the undulator. It can be seen that the two ellipses are identical. That shows that the bunch

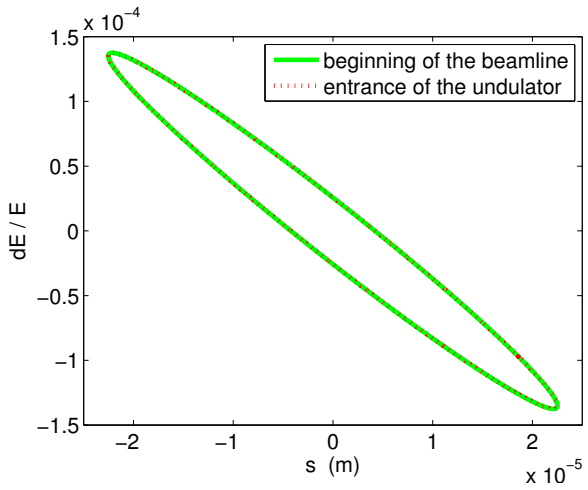

Figure 4.4: One-σ phase space ellipses in the longitudinal phase space at the beginning of the beamline and at the entrance of the undulator.

compression effect of the chicane is negligible. In Fig. 4.3 and 4.4 the ellipses were shown for the entrance of the undulator because at this point further simulations need to be conducted by specialized software. [Wiedemann, 2007, p. 139]

4.1.3 Conclusion

The considered magnetic chicane and focusing section are suitable to couple the corresponding electron beam into the cavity of the XFELO that is under consideration for the European XFEL. Figure 4.2 shows that the requirement of a round beam with a beam waist in the middle of the undulator was met. Furthermore it shows, that according to field quality specifications of the European XFEL quadrupole magnets, the maximum beta function is small enough to neglect distortion of the beam due to field errors of the magnets. Figure 4.2 shows also that due to the symmetry of the chicane the dispersion is compensated. Furthermore it was shown by evaluating equation (4.1) that bunch compression effects are negligible because of the relatively small deflection angle of the bending magnets. This result was confirmed by the results of the particle tracking shown in figure 4.4, where no bunch compression effects can be recognized.

4.2 Simulation of Arrival Time Jitter

In this section the influence of a lack of overlap between the electron bunches and the x-ray pulses is studied, whereby the focus rests on the arrival time jitter between electron

Table 4.2: Input parameters of the simulations

Parameter	**unit**	**Setup 1**	**Setup 2**
Electron energy	GeV	14.5	14.5
Bunch charge	nC	1	0.1
Bunch length (FWHM)	fs	178	18.8
Peak current	kA	4.9	5
Normalized emittance	µm	1	0.3
Slice energy spread	MeV	1.5	2.04
Beta function at waist	m	7.5	7.5
Radiation wavelength	Å	1.027	1.027
Undulator length	m	15	15
Undulator period	m	0.03	0.03
Cavity length	m	66.62	66.62
Outcoupled radiation	%	4	4
Cavity losses	%	8	8

bunch and x-ray pulse. The currently lowest arrival time jitter of 30 fs was achieved with a synchronization system reported in [Schulz et al., 2015] using 60 fs (RMS) long electron bunches. At the European XFEL a synchronization system similar to that is planned to be implemented [Altarelli et al., 2007] and it is assumed that the arrival time jitter will decrease for bunches shorter than 60 fs. At the European XFEL electron bunches with a length between 180 fs and 2 fs are planned to be generated. Due to the fact that the arrival time jitter of the electron bunches at the European XFEL will be of the order of the bunch length, some impact on the XFELO operation can be expected. To quantify the impact of the arrival time jitter on the XFELO operation, simulations using the code GENESIS 1.3 [Reiche, 2004] have been performed. The simulations have been performed for bunch lengths of 178 fs and 18.8 fs (FWHM), respectively, with four levels of arrival time jitter each. Since not only the arrival time is subjected to jitter, exemplarily a simulation has been performed that incorporates bunch position and angular jitter as well. The jitter levels used in this simulation are the levels expected for the European XFEL Linac.

4.2.1 Simulations

The simulations were performed with the single pass FEL code GENESIS 1.3 together with an oscillator extension code [Zemella, 2013], which calculates the propagation of the output radiation field in the cavity of one GENESIS run and uses it as the seed radiation

for a subsequent GENESIS run. The calculation of the field propagation inside the cavity comprises the free space propagation, the spectral filtering due to the Bragg reflection, the transformation due to the focusing elements and the outcoupling of a fraction of the radiation at one of the crystal mirrors. The spectral bandpass filter that is applied to the radiation to simulate the Bragg reflection (4 4 4) at a Diamond crystal has a width of $\Delta\lambda/\lambda \approx 1.66 \cdot 10^{-6}$ (FWHM) which corresponds to a Fourier-limited pulse duration of about 180 fs (FWHM). For the generation of the arrival time jitter a script was written that shifts the radiation pulse by the deviation in the arrival time relative to a reference point within the simulated time window. The value of the deviation in the arrival time is generated by a random number generator that generates Gaussian distributed random numbers. Since GENESIS has input variables for angular and positional deviations of the electron beam the implementation of this kind of jitter could be done in a different way. Hence a script was written generating uniformly distributed random numbers and writing these numbers into the GENESIS input file. Both scripts have to be executed for each cavity round trip to generate the respective jitter. The input parameter of the simulations are shown in Table 4.2. One run of a jitter simulation presented here starts with a first electron bunch that generates an x-ray pulse via the SASE process and continues until the XFELO has reached saturation. Since jitter is a statistical process the simulations presented here consist of 25 runs, allowing to calculate the mean and variance of the results.

4.2.2 Results

The arrival time jitter simulations have been performed for two different setups shown in Table 4.2. The essential difference in these two setups is the electron bunch length of 178 fs and 18.8 fs, respectively. The results of the simulations are shown in Figure 4.5. The top row shows the results of setup 1. The first plot of the top row shows the mean pulse energy versus the number of undulator passes and the center plot in the top row shows the corresponding deviation of the mean for the jitter levels (RMS) of 0 fs (blue), 30 fs (red), 60 fs (brown) and 120 fs (black). For the jitter levels of 30 fs and 60 fs the impact on the gain process is quite low whereas at 120 fs the impact is significant. This result is in good agreement with the expectation that a jitter significantly shorter than the bunch length should only have a low effect on the gain process. In the plot of the energy deviation from the mean pulse energy it is noticeable that the deviation of the mean has a maximum roughly at the point where the gain is maximum. The reason for this is that at high gain levels a relatively small disturbance gets amplified and thus broadens

the relative uncertainty. At saturation, lower pulse energies get amplified more than higher pulse energies and this leads to a narrowing of the relative uncertainty. The right picture in the top row shows the pulse duration versus the number of undulator passes. The pulse duration has a minimum about the point of the maximum gain. The reason for this could be that the amplitude of the electrical field in the center of the x-ray pulse is higher than at the head or the tail. If an electron bunch meets the circulating x-ray pulse it should therefore take longer for the microbunching to form at positions where the amplitude of the electrical field is lower compared to positions where the amplitude is higher. This should lead to a higher gain in the center of of the x-ray pulse until saturation is reached. Intensifying the center of the pulse more than the tails should thus shorten the over-all pulse duration. Furthermore the plot shows that the pulse duration increases with increasing jitter and that the fluctuation of the pulse duration increases with increasing jitter as well. The reason for the increase in the pulse duration is that due to the jitter the circulating pulse in the cavity and the electron bunch do not overlap completely, which leads to an asymmetrical growth of the x-ray pulse and thus the pulse duration increases. The plots in the bottom row show the results of setup 2 (see Table 4.2). It should be noticed that in the bottom row the assumed jitter levels, if compared to the bunch length, are much bigger than in the top row. However, as the first and second plot (bottom row) show, the gain process at the same jitter levels is almost as stable as in the simulations using 178 fs long electron bunches. The reason for this is the constant length of the circulating x-ray pulse. As mentioned above the Fourier-limited pulse length is due to the Bragg-reflection about 180 fs (FWHM). If a shorter pulse is generated only that fraction of the pulse within the bandwidth of the Bragg-reflection will be reflected. That leads to a circulating pulse much longer than the pulse generated in the undulator. Taking the circulating x-ray pulse of about 180 fs into account it becomes clear that the jitter sensitivity of an XFELO run with 18.8 fs electron bunches is almost the same as for an XFELO run with 178 fs electron bunches. Apart from this interesting fact the first two plots in the bottom row show the same characteristic like the first two plots in the top row. The right plot in the bottom row shows the mean pulse duration versus the number of undulator passes. All curves show a slight increase in pule duration and depending on the jitter level the pulse duration fluctuates more or less.

The results of the simultaneous simulation of arrival time jitter, angular jitter and positional jitter are shown in Figure 4.6. For the simulation the setup 2 (see Table 4.2) has been used. The jitter levels are with 30 fs for the arrival time jitter, 100 nrad for the angular jitter and 1 μm for the positional jitter chosen like expected for the European

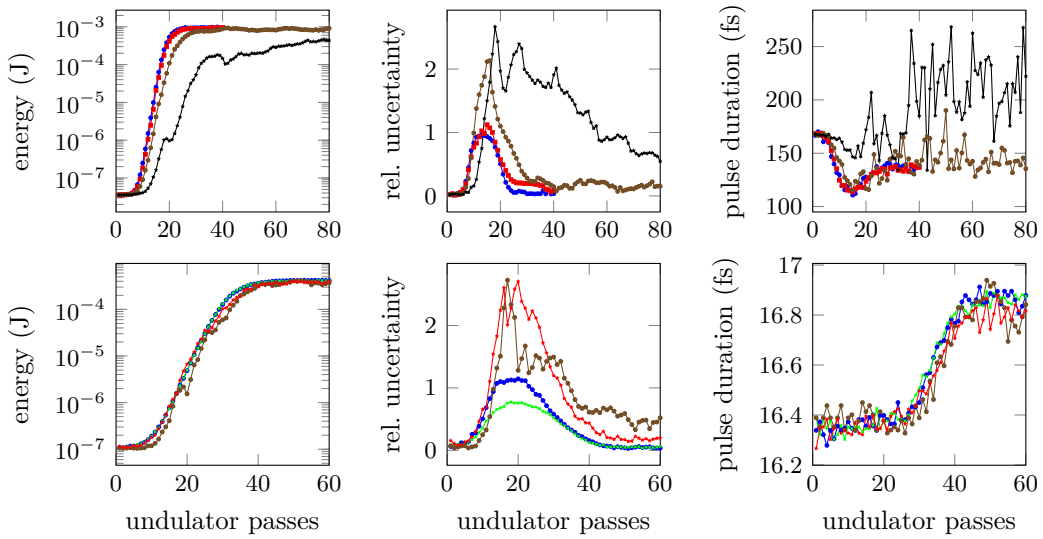

Figure 4.5: Effect of the arrival time jitter on the XFELO process at the undulator output for jitter levels of 0 fs (blue), 6.3 fs (green), 30 fs (red), 60 fs (brown), and 120 fs (black). In the top row the results of the simulation with 178 fs long electron bunches are shown. In the bottom row the results of the simulation with 18.8 fs long electron bunches are shown. The plots on the left show the mean pulse energy versus the number of undulator passes for the different jitter levels. The centered plots show the relative deviation of the mean pulse energy and the plots on the right show the mean pulse duration (FWHM) of the x-ray pulses.

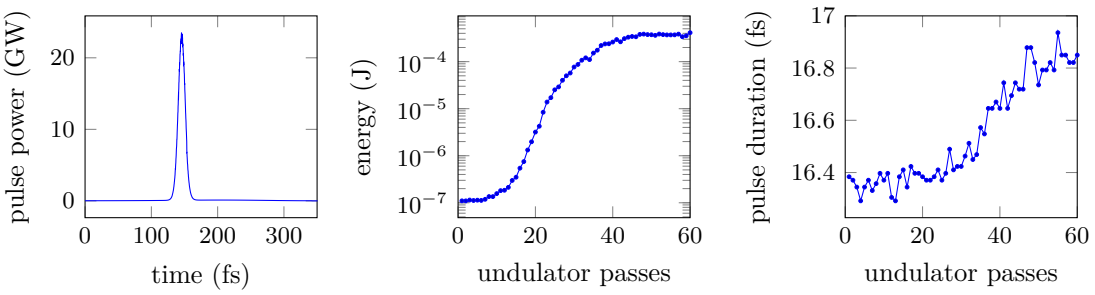

Figure 4.6: Performance of an XFELO at the undulator output considering the arrival time jitter (30 fs), angular jitter (100 nrad) and positional jitter (1 µm) expected for the European XFEL Linac. The left plot shows an exemplary pulse at saturation. The center plot shows the mean pule energy as a function of the number of undulator passes and the right plot shows the mean pulse duration (FWHM) as a function of the number of undulator passes.

XFEL Linac. The first plot shows an exemplary x-ray pulse at saturation. The pulse has an almost Gaussian shape with only some spikes on top which indicates a high level of longitudinal coherence. Even though it cannot be recognized very well it should be noticed that the 17 fs (FWHM) pulse has the weak circulating pulse of 180 fs (FWHM) as a background. The plot in the center shows the mean pulse energy versus the number of undulator passes. The curve has some small spikes and saturates at a mean pulse energy of about 300 µJ. The plot on the right shows the mean pulse duration as a function of the undulator passes. It can be seen that the mean pulse duration increases during the gain process and after saturation it stabilizes at about 16.8 fs. Overall this simulation shows a very similar characteristic to the simulation of setup 2 only taking arrival time jitter into account (see Figure 4.5).

4.2.3 Conclusion

In this section the influence of electron beam jitter on the XFELO gain process was studied. An interesting result of the simulations is that for bunch lengths below the Fourier-limited pulse length of the mirrors the sensitivity to arrival time jitter does not significantly increase when the bunch length decreases. Therefore it turned out that the levels of arrival time jitter which can be achieved with today's technology are low enough to allow stable XFELO operation for all electron bunch lengths. At arrival time jitter levels significantly below the duration of the circulating pulse the jitter has only a weak impact on the mean gain, the mean saturation energy, and the mean

pulse duration. However the fluctuation of these quantities increase noticeable. The simultaneous simulation of arrival time jitter, angular jitter and positional jitter have shown that it should be possible to run an XFELO under jitter conditions expected for the European XFEL Linac. Even though the fluctuations of the pulse energy and pulse duration are noticeably increased by the jitter the operation can be considered stable.

4.3 Influence of Generated Strain on the Bragg Reflection

In this section the influence of thermal and mechanical strain in the crossplane direction caused by pulsed laser irradiation will be studied. As discussed in chapter 3 a laser pulse irradiating a solid causes a thermal expansion of the solid and the thermal expansion in turn causes an elastic strain pulse propagating in the solid. Because Bragg reflection relies on a constant lattice spacing the laser pulse induced strain can distort the reflection characteristics of a Bragg mirror. In earlier studies [Zemella et al., 2012] the laser induced strain was assumed to be constant in the crossplane direction and the elastic strain pulse propagating in the crystal was not considered. With the assumption of a constant strain profile the standard dynamical theory of x-ray diffraction could be applied. Within this theory the absorption of pulse energy only causes a shift of the Bragg energy but the shape of the reflectivity curve is conserved. However the justification of this assumption is questionable because the penetration depth of the x-rays determines the thermal strain profile to be of the same order as the penetration depth of the x-rays. Additionally unstrained regions deep in the crystal can still reflect radiation at the original energy band especially in diamond with its very low absorption for x-rays around 12 keV. Therefore in this study a more realistic thermal and elastic strain profile is obtained by solving equation (3.21) numerically including a source therm which considers the thermal diffusion in the crystal. The resulting Bragg reflection was then calculated by means of the dynamical x-ray diffraction theory of multilayers [Stepanov et al., 1998], where strain profiles can be incorporated by discretizing the strain and assigning each discrete strain level to a certain layer in the multilayer system.

4.3.1 Simulation Details

In section 3.3 the train generation by a short laser pulse has already been discussed neglecting the influence of thermal conduction in the solid. In that case an analytic solution could be derived (c.f equation (3.23)). In this study the thermal conduction was considered, which disables an analytic solution of the thermomechanical problem.

When thermal conduction is considered the stress field in crossplane direction can be written as

$$\sigma(x,t) = \sigma^{\mathrm{m}}(x,t) + \sigma^{\mathrm{th}}(x,t) = \rho {v_{\mathrm{s}}}^2 \eta(x,t) - 3\beta B \Delta T(x,t), \tag{4.3}$$

where σ^{m} and σ^{th} are the thermal and mechanical strain contributions, respectively, ρ is the mass density, v_{s} the sound velocity, η the strain in crossplane direction, β the thermal expansion coefficient and B the bulk modulus. When equation (4.3) is inserted into Cauchy's equation (3.21) a wave equation can be derived in the same way as already shown in section 3.3. The resulting wave equation was solved under the assumption that the temperature field is decoupled from the strain field. Under this assumption the temperature field can be calculated separately from the strain field. The temperature field was calculated using an axisymmetric 2D code based on Fourier's law [Zemella, 2013, pp. 38–42]. The resulting strain field was then calculated numerically utilizing the finite-difference method with the central differencing scheme which yields a second order accuracy. The Bragg reflectivity curves were then obtained by using the strain field at subsequent time steps as an input to the program GID_sl [Stepanov, 2017] which solves dynamical diffraction problems of multilayers by means of the recursion matrix method [Stepanov et al., 1998]. In this calculation the strain fields at the different instances of time are assumed to be static, which neglects the small Doppler shift of the x-rays reflected from the propagating strain pulse.[39] The parameters of the simulation are shown in table 4.3. They represent the expected conditions in an XFELO cavity with a reduced saturation energy of the XFELO of about 200 µJ. The simulations were performed with two different crystals thicknesses. The first crystal has a thickness of 42 µm. Such a crystal could be used to couple out a fraction of the FEL radiation because the penetration depth of 12 keV x-rays at the diamond (4 4 4) reflection enables a fraction of the radiation to traverse the crystal before the radiation is scattered back. The second crystal has a thickness of 200 µm. This thickness represents an example of a thick crystal, which does not transmit any notable radiation and would therefore act as a standard cavity mirror.

4.3.2 Results of the Simulation

The first time steps of the simulation are shown in figure 4.7 for the 42 µm crystal and in figure 4.8 for the 200 µm crystal, respectively. The arrival of the x-ray pulse is at $x = 0$

[39] More details about this effect, which can be interpreted as coherent Brillouin scattering, can be found in [Reis et al., 2001] and [Lindenberg et al., 2000].

Table 4.3: Input parameters of the simulations shown in figure 4.7 and 4.8.

Parameter	**Abbr.**	**Unit**	**Value**
Thermal conductivity	λ_{th}	W/(m K)	$1.73 \cdot 10^{3}$
Specific heat	c_v	J/(kg K)	$5.11 \cdot 10^{2}$
Mass density	ρ	kg/m^2	$3.51 \cdot 10^{3}$
Sound velocity	v_{s}	m/s	$1.75 \cdot 10^{4}$
Absorption coefficient	κ_ν	1/m	$5.00 \cdot 10^{4}$
Temperature	T	K	$3.00 \cdot 10^{2}$
Th. expansion coefficient	β	1/K	$1.08 \cdot 10^{-6}$
Bulk modulus	B	Pa	$4.42 \cdot 10^{11}$
Absorbed pulse energy	E_{p}	J	$2.00 \cdot 10^{-6}$
Reflectance	R	–	$9.90 \cdot 10^{-1}$
Angle of incidence	α	degree	$9.00 \cdot 10^{1}$
Beam radius	σ	m	$5.00 \cdot 10^{-5}$
Bragg reflection	$(h\ k\ l)$	–	(4 4 4)

at $t = 0$. The plots on the left show the strain profile on the beam axis for different instances of time. The plots on the right show the associated Bragg reflectivity curve at the respective time step. The reflection curve of both the 42 and the 200 µm thick crystal show fringes (lower reflectivety local maxima) on both sides of the principal maximum of the curve. This fringes are caused by the finite thickness of the crystals and thus the finite number of lattice planes involved in the scattering process.[40] The time steps shown represent one transition of the strain pulse through the crystal. Because the strain pulses are reflected at the boundaries the pulses move back and forth. Therefore the further behavior of the strain can be obtained by reading the plots back and forth (excluding the plot at $t = 0$). However it should be kept in mind that the strain changes slightly with time because of thermal conduction and ultrasonic absorption (cf. fig. 3.4). As discussed in section 3.1.1, the condition of the Bragg mirrors is most important just before the arrival of the next x-ray pulse. At the European XFEL the electron bunch separation time will be about 220 ns. After that time the thermal strain is decayed to about 50% of its original value. The elastic strain pulse however remains almost constant with about 99% of its original value after 220 ns.[41] The results for the two different crystal thicknesses differ because of their different ratio between the penetration depth of the radiation and their thickness. In figure 4.7 (thin crystal) two strain pulses, one on each

[40] See fig. 1.4 where the Bragg reflectivity curves of an infinitely thick crystal is compared to that of a 42 µm thick crystal.

[41] This statement is based on the data shown in figure 3.4.

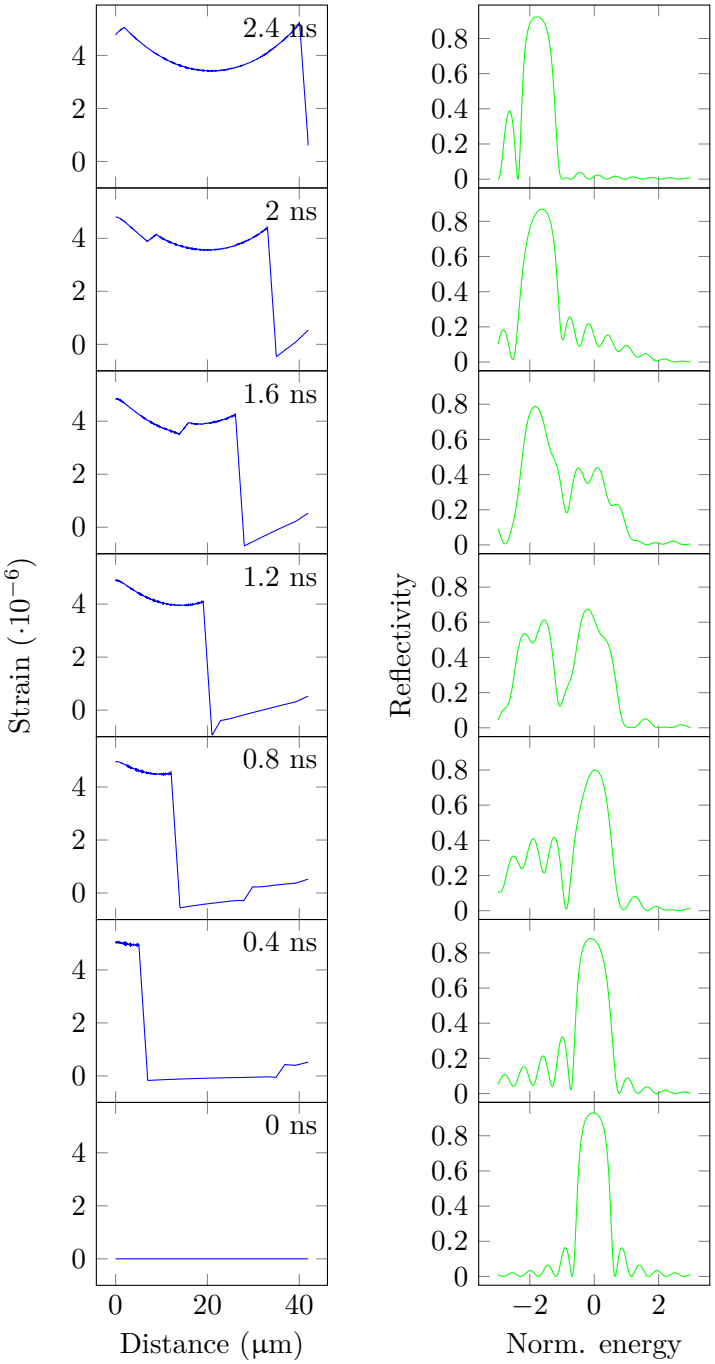

Figure 4.7: Strain field and the respective (4 4 4) Bragg reflectivity curve at 90° of a 42 µm thin diamond crystal. Both, the plots on the left and the right show snapshots at the time labeled in the upper right corner of the plots on the right. The strain was generated by a Gaussian beam with an RMS radius of $\sigma = 50$ µm and an absorbed energy of 2 µJ. The penetration depth of the radiation was 20 µm. The photon energy in the left plot is normalized to the FWHM of the reflectivity curve of the unstrained crystal of about 26.5 meV.

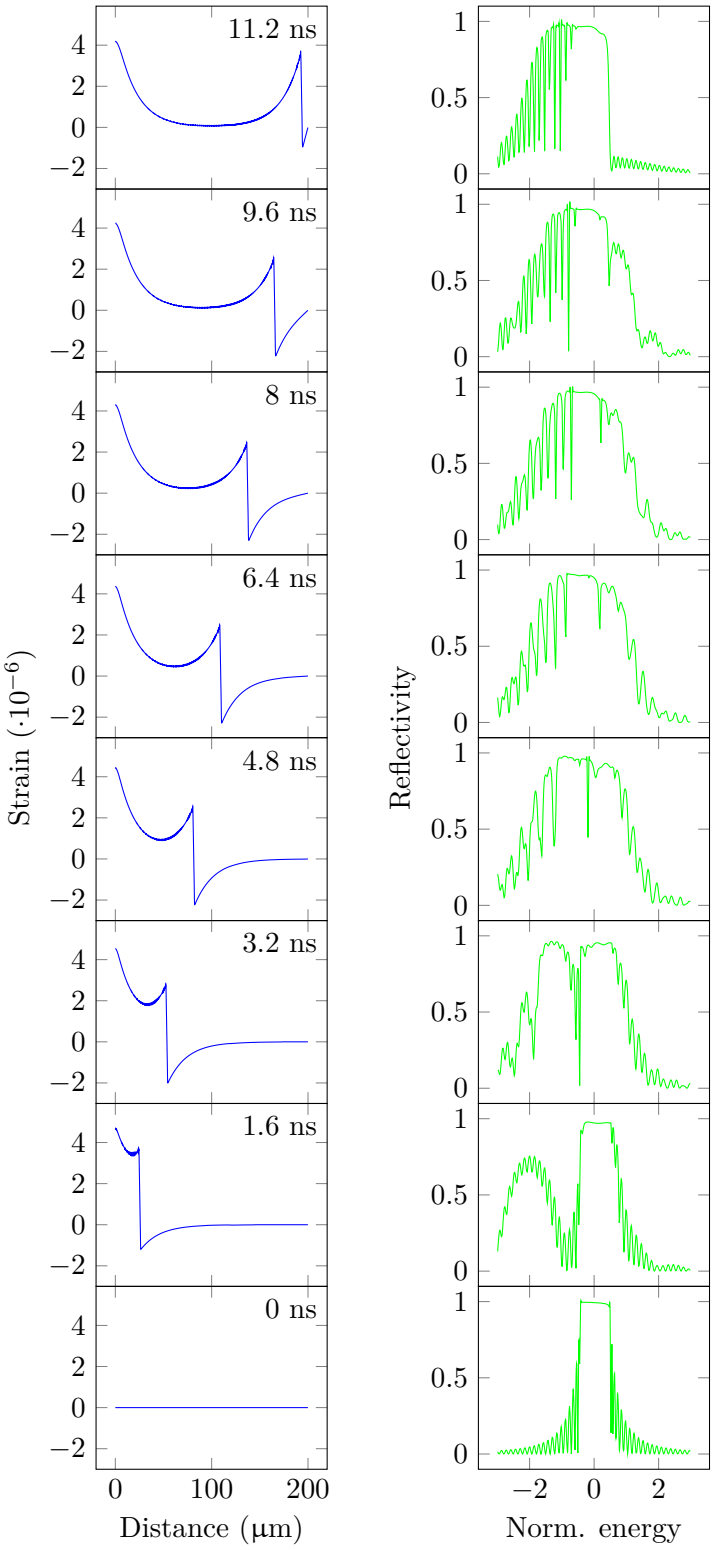

Figure 4.8: Same as in fig. 4.7 but with a 200 µm crystal and a ref. FWHM of 21 meV.

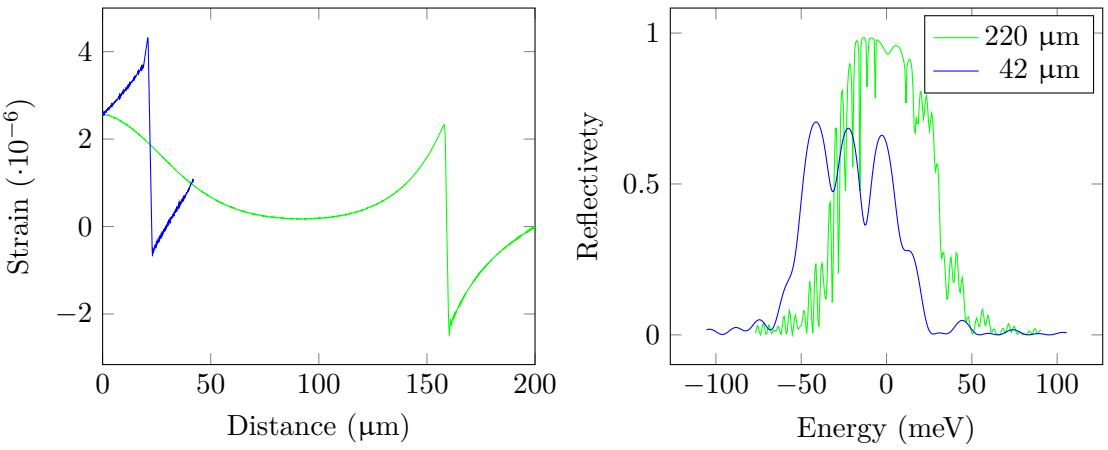

Figure 4.9: Comparison of the strain profile and the related Bragg reflectivity between a 42 and the 200 µm thick crystal 220 ns after the arrival of a short x-ray pulse. Both plots show a snapshot after 220 ns when the generated strain pulse has circulated several times within the crystal. The left plot shows the crossplane strain profile and the right plot shows the respective Bragg reflectivity curve for the 42 and a 200 µm thick crystal. The parameters of the simulation are shown in table 4.3.

surface of the crystal are generated and start to propagate in opposite directions into the crystal. The small strain front at the back of the crystal is generated by the fraction of radiation transmitting the mirror. In the thin crystal, basically exist two strain states, the unstrained state where $\eta \approx 0$ and the strained state, where $\eta \approx 4 \cdot 10^{-6}$. It can be seen, that one of the two different Bragg peaks develop depending on the dominating stress state. The 200 µm crystal (results shown in figure 4.8) has a strain profile very similar to that of the analytic solution of the problem discussed in section 3.3. The Bragg reflectivity curve shows rather a broadening instead of the flipping behavior as in the case of the thin crystal. Because of the larger thickness compared to the penetration depth of the x-rays there is always a region in the crystal with low strain. Hence the reflectivity curve of the unstrained crystal is always present as a component in the over all reflectivity curve.

Because of the importance of the mirror condition just before the arrival of the next x-ray pulse the conditions of both the 42 and the 200 µm crystal are shown separately in figure 4.9 at $t = 220$ ns. It can be seen that the thermal strain is decreased by about 50% of its original value whereas the elastic strain remained constant. Furthermore it can be seen, that the heat diffused deeper in the crystal, which resulted in a spatial spread of the thermal strain. The Bragg reflectivity curves are broadened by a factor of about two and their shape is severely distorted compared to the curve of an unstrained crystal. In

addition, the peak reflectivity of both curves is deteriorated. This is especially true for the 42 µm crystal, which peak reflectivity is reduced from 93% to 70%.

4.3.3 Discussion of the Strain Generation at Cryogenic Temperatures

A good measure for the generated strain is the initial surface strain η_0 defined by equation (3.19) in combination with the absorption coefficient κ_ν defined by equation (3.15).[42] In this context the absorption coefficient is determined by the inverse of the extinction length of the respective Bragg reflection. The extinction length has only a weak temperature dependence, described by the Debye-Waller factor, and can therefore assumed to be constant. The initial surface strain η_0 depends among others on the coefficient of thermal expansion β and the specific heat C_p. Both have a strong temperature dependence and both change about orders of magnitude between 1 and 300 K. Therefore one could argue, that in general also the strain generated from a certain amount of absorbed energy will probably change over orders of magnitude from 1 to 300 K. This issue can be resolved in a very general way when equation (3.13) from the section about thermal expansion is inserted into the equation for η_0 (eq. (3.19)), which yields

$$\eta_0 = \frac{\gamma \kappa_\nu (1-R) E_\mathrm{p}}{{v_\mathrm{s}}^2 A}, \tag{4.4}$$

where A represents the irradiated area, E_p the laser pulse energy, R the fraction of reflected energy and γ the Grüneisen parameter. Since γ is a material constant, which has only a slight temperature dependence, η_0 can be assumed as approximately temperature independent. This is an important result when considering the ideal base temperature for an XFELO mirror. In case of the thermal strain it is favorable to go to cryogenic base temperatures because of the high thermal diffusivity and low thermal expansion at cryogenic temperatures. This leads to a fast decay of the temperature and the remaining temperature offset does only have a small effect on the strain because of the low thermal expansion. As stated by equation (3.26) the damping of the elastic strain is even lower at low temperatures. According to that equation the acoustic absorption coefficient for a pulse considered here is lower by about four order of magnitude at 50 K compared to 300 K. That means, that going to cryogenic temperatures is not favorable in terms of the influence of the elastic strain on the Bragg reflection upon the arrival of the subsequent x-ray pulse.

[42] See section 3.3 for further details.

Note that equation (4.4) assumes an instantaneous and localized conversion from electromagnetic to thermal energy (a local thermal equilibrium of the phonons). However when the mean free path of the heat carriers become of the order of the absorption length of the radiation this assumption is not justified anymore. The prediction of this effect is difficult because in the conversion process electrons with their own energy dependent mean free path distribution and phonons are involved establishing the local thermal equilibrium. In chapter 5 measurements are presented, which addresses this issue among others.

4.3.4 Conclusion

In this study it could be shown, that the application of the strain generation model discussed in section 4.3.1 and section 3.3 yields results, considerably different from previous studies [Zemella et al., 2012], where only a constant thermal and no elastic strain was assumed. The model of the previous studies only predicted an energy shift of the unstrained reflectivity curves as the response on pulsed laser irradiation (cf. fig. 4.7 and 4.8 at 0 ns for the unstrained reflectivity curve). On the considered timescale these results do not only differ from the previous ones in the initial phase of the simulation and then converge to the results of the previous study. As shown in figure 4.9 the Bragg reflectivity curve just before the arrival of the subsequent x-ray pulse differs significantly from an unstrained and only energy-shifted curve. The results of this study imply also that all FEL simulations which model the effect of strain generation by just energy-shifting the reflectivity curve of an unstrained crystal should be questioned. Therefore new simulations are required which incorporate the thermomechanical behaviour of diamond Bragg mirrors.

Furthermore it could be shown that (as long as the applied model is valid) going to cryogenic temperatures does not weaken the strain generation, and because of the lower damping at lower temperatures the elastic strain component takes even longer at low temperatures to be damped. While thick diamond crystals could theoretically be cut in a way that the strain pulses are deflected away, these results especially questions the concept of a thin crystal to couple out the radiation. Therefore the alternative outcoupling of the radiation by means of a “three-beam-case” [Authier, 2001, pp. 225–236] should be studied concerning the effect of strain generation.

If the predicted mechanical strain pulses cannot be diminished technically the saturation energy of an XFELO assumed to be acceptable must be reduced considerably to maintain the nominal bandwidth and pulse to pulse stability expected for an XFELO

with ideal Bragg mirrors. However, as discussed at the end of section 4.3.3, the prediction of the generated strain at cryogenic temperatures is questionable. Because of the significant implications of this issue measurements are required, which elucidate the generation and dissipation of mechanical strain in diamond crystals due to pulsed laser irradiation. In chapter 5 measurements are presented, which among others addresses the strain generation.

5 Measurements

As outlined in section 3.5 a reliable prediction of the thermalization dynamics in a solid under ballistic heat transport is only possible for well known materials under well known conditions (e.g. temperature, geometry, surface conditions). Since the material of interest in this work – diamond at cryogenic temperatures – is not well known in terms of its heat carrier thermalization dynamics a measurement scheme was developed, in which the thermal load of a Bragg-mirror used in an XFELO can be simulated. The main objective of this chapter is to describe the measurement scheme developed, present the results of the first measurements performed with this setup and to evaluate the results in terms of the applicability of diamond crystals as future Bragg mirrors for an XFELO.

Another objective of this chapter is to experimentally verify two different heat equations with regard to the future modeling of XFELO mirrors – the classical heat equation (HE) and the hyperbolic heat equation (HHE). Both equations are generally understood to correctly describe transient heat transfer problems in the regime of diffusive heat transport and to fail in the regime of ballistic heat transport [Maassen and Lundstrom, 2016]. In section 3.4.3.1 both the HE and HHE are derived from the Boltzmann transport equation under the assumption of diffusive heat transfer. There, the HE was shown to be a special case of the HHE which assumes the mean phonon relaxation time to be much shorter than the timescale of interest. Hence the HHE can be regarded as a modified version of the HE, which captures finite phonon propagation velocity instead of the unphysical infinite phonon velocity assumed by the HE.

Due to the mechanism described in section 3.4.3.2 and illustrated in figure 3.12 the HE is assumed to fail when the characteristic length scale of the transient heat transfer problem approaches the average mean free path of the phonons [Wilson and Cahill, 2014, 2015]. Because the HE is the standard tool for analyzing heat transfer problems, in this chapter it is intended to show whether and, if so, how the HE fails to describe the thermalization dynamics in the case of an XFELO Bragg mirror at room and cryogenic temperatures. As a measure for this failure the apparent thermal conductivity normalized to the bulk thermal conductivity is used. The apparent thermal conductivity is the conductivity a system appears to possess when a certain model, which has the thermal conductivity as a free parameter, is used to describe the behavior of the system. If the

thermal model fails, the apparent thermal conductivity differs from the bulk thermal conductivity.

As discussed in section 3.4.3.2 it was recently shown, that the HHE can be rewritten as the McKelvey-Schockley flux equations. The McKelvey-Schockley flux equations were originally developed to treat electron transport and recently they were reformulated to describe phonon- and thus heat-transport in insulators and semiconductors [Maassen and Lundstrom, 2015]. Without restricting to diffusive heat transport the McKelvey-Schockley flux equations can be derived under certain simplifying assumptions from the Boltzmann transport equation. For that reason the McKelvey-Schockley flux equations and the equivalent hyperbolic heat equation are valid on all length and time scales where the Boltzmann transport equation is applicable (cf. sec 3.4.3). Due to these recent theoretical results, the hyperbolic heat equation is used for analyzing the measured data to verify experimentally its predictive power from the diffusive to the ballistic heat conduction regime. In this analysis the required (average) phonon mean free path was obtained by its relation (eq. (3.39)) to the thermal conductivity. Although the results of the McKelvey-Schockley flux equations were validated by results of the Boltzmann transport equation [Maassen and Lundstrom, 2015], it remains to be demonstrated experimentally if the assumption of a constant phonon velocity and mean free path is valid for diamond at cryogenic temperatures and if extracting the phonon mean free path from the bulk thermal conductivity yields correct results for different problems. Here again it is taken as a measure of the equations validity how well the bulk thermal conductivity is reproduced when fitting the model based on the HHE to the measured data.

5.1 Method of the Measurement

The measurement method developed in this work is based on the time domain thermoreflectance method. The thermoreflectance method utilizes the temperature dependence of the optical reflectivity ($\Delta R/\Delta T$), which is typically of the order of $(10^{-2}...10^{-5})R$.

In a typical thermoreflectance experiment in the time domain [Cahill et al., 2002] a short laser pulse of about 1 ps is split into a pump and a probe beam which can be shifted against each other in time. Then the pump pulse excites the sample and the probe pulse samples the excitation at different times by delaying the probe pulse relative to the pump pulse. Typically the pump pulse is modulated leading to a modulation of the probe pulse, which can then be detected with a photo diode connected to a log-in amplifier. With this data acquisition scheme good signal-to-noise ratios are routinely achieved. The thermal properties of a sample being measured can be obtained by fitting a heat transfer model

to the data, where the thermal conductivity, heat capacity or interface conductance are treated as free parameters. When probing transparent materials the sample is usually coated with a thin metal film (70-80 nm) which acts as a transducer from optical to thermal energy. The usage of a transducer usually imposes more free parameters to the heat transfer model because the interface conductance and the thermal conductivity of the transducer is usually unknown. Furthermore ballistic effects can also occur in the transducer which can lead to a corruption of the heat transfer model and thus wrong results, even if the material of interest is modeled properly [Wilson et al., 2013; Wilson and Cahill, 2014].

Since the experimental results of this work are intended to be applicable to the Bragg-mirrors in an XFELO the typical time domain thermoreflectance scheme, described above, is not appropriate. There are two reasons for this: firstly, in order to simulate the heat load of an x-ray pulse the absorption length of the laser radiation in the crystal should be as close as possible to the extinction length of a Bragg reflection[43], which is about 20 µm for a diamond (4 4 4)-reflection near normal incidence. For that reason no transducer could be used and in order to obtain the right absorption characteristics in the diamond crystal an UV laser was chosen as the pump laser.

Secondly, as discussed in section 3.1.1 the condition of the Bragg-mirrors at the arrival of the subsequent x-ray pulse is essential for the reflectance of that subsequent pulse. Therefore the temporal range in which the temperature change can be measured should at least cover one full pulse cycle, which is about 220 ns in the case of an XFELO driven by the Europen XFEL LINAC. This required 220 ns delay would result in a delay line of about 66 m which is hard to achieve especially with UV lasers. As the solution to this problem a second 532 nm CW laser was included into the setup as the probe laser. This could be done because the required temporal resolution of about 1 ns (discussed in section 3.1.1) is relatively low and hence fast photo diodes are adequate to resolve the reflectivity change of the CW signal.

With this setup a fast oscilloscope, triggered by a fraction of the pump beam, can sample a whole pulse cycle. In order to achieve a reasonable signal-to-noise ratio many pulse cycles are averaged to compose the final measurement result.

5.1.1 Optical Measurement of Crystal Properties

As outlined in chapter 3 the absorption of laser pulses causes a time dependent distortion of the temperature and strain field inside a solid. Since the optical properties of a solid are

[43] As discussed in section 3.4.3.2 the temperature gradient in the crystal can influence the predictive power of the heat equation.

influenced by its temperature and its strain profile, the temperature or strain of a solid can be investigated by measuring the optical properties of this solid. A measure for the optical properties of a solid is the complex dielectric function $\tilde{\epsilon}$ and the complex refractive index $\tilde{n}$, respectively. They are related by $\tilde{n}^2 = \tilde{\epsilon}$. If a crystal plate is considered which has a gradient of temperature or strain only in the x-direction (cross-plane) the optical functions $\tilde{\epsilon}$ and $\tilde{n}$ can be expressed as

$$\tilde{\epsilon}(x,t) = \tilde{\epsilon} + \Delta\tilde{\epsilon}(x,t) = \left[\tilde{n} + \Delta\tilde{n}(x,t)\right]^2, \ \Delta\tilde{n}(x,t) = \frac{\partial\tilde{n}}{\partial Z} Z(x,t), \tag{5.1}$$

where Z represents the change in temperature or the strain field in the crystal and $\partial\tilde{n}/\partial Z$ is the thermo-optical or acousto-optical constant. In this work the optical functions are probed by means of a reflectivity measurement. With this method a change in reflectivity can be related by

$$\frac{\Delta R}{R} = \frac{4(n'^2 - n''^2 - 1)\Delta n' + 8n'n''\Delta n''}{[(n'+1)^2 + n''^2][(n'-1)^2 + n''^2]} \approx \left(\frac{1}{R}\frac{\partial R}{\partial Z}\right) Z = \kappa_Z Z \tag{5.2}$$

to a change in the refractive index (in the case of normal incidence) and thus to a change of the temperature or strain. Here the n' and n'' are defined as $\tilde{n} = n' + \mathrm{i}n''$. Equation (5.2) is derived from the Fresnel equations. The relationship between $\Delta R/R$ and Z is usually quite linear so that the linear approximation in equation (5.2) is usually quite accurate for temperature changes of only some degree. With the knowledge of κ_Z the value of Z at a certain position of a sample can then be determined by measuring the reflectivity at that position. The interest in this work focuses on samples, which have characteristic length scales of some µm to hundreds of µm. In particular the focus is on the thermalization dynamics of absorbed short laser pulses on that length scales. Under such conditions very fast transients occur which can hardly be measured by other means than optical techniques. In general the light reflected from a sample which has a cross-plane temperature gradient and thus a gradient in $\tilde{n}$, consists of two components. The light reflected at the sample interface and the internal reflected light, which originates from the gradient in $\tilde{n}$. As pointed out in section 3.3, a short laser pulse absorbed in a sample always generates a heated region in the sample and a running strain pulse caused by the thermal expansion of the heated region. This causes a strain profile, shown in figure 3.3, and thus a respective modulation of $\tilde{n}$. Following a method suggested by [Thomsen et al., 1986] the reflected light can be calculated from the temperature and strain profile in the sample. This calculations show that in the case of the heated area the internal light reflection is inhibited because the temperature gradients are small

compared to the light wavelength. The running strain pulse in turn causes a Doppler shifted internal reflection, which interferes with the light, reflected at the interface, and thus causes a beat in the overall reflected signal with a frequency of about 160 GHz. In the measurements presented in this chapter a 532 nm CW laser is used to probe thin diamond plates. Because diamond is transparent at that wavelength the internal reflection of the light at the running strain pulse is present for its whole lifetime. However the detection of the reflected light is done by a photo diode and a connected oscilloscope which have a system bandwidth of about 2 GHz. This detection scheme results in a low pass filtering of the signal which in turn smoothes out the 160 GHz beat caused by the interference of the internal reflection with the interface reflection. For that reason the change of reflectivity measured with the oscilloscope is directly proportional to the temperature at the surface (interface) of the sample.

5.2 Experimental Setup

The measurements presented in this chapter are so-called optical pump-probe measurements. The experimental setup is shown in figure 5.1 and the parameters of the laser system can be found in table 5.1. A UV pump laser emits pulses with a duration of 1 ns. A small fraction of the pump beam is coupled out and directed on to a fast photo diode to trigger the measurement while the major part of the pump beam is focused on the sample (diamond crystal). The pulses are then absorbed by the sample within an absorption length of about 3.5 µm. The absorbed radiation energy is then converted to thermal energy as described in section 3.1. The resulting local temperature jump and the subsequent exponential temperature decay to the base temperature can be measured by the CW probe laser. This can be done by measuring the change in reflected power over time, which is proportional to the change in temperature. To increase the signal to noise ratio, the probe beam is split into a reference beam and an actual probe beam. The probe beam is reflected at the sample's point of interest and both, the reference and the probe beam are detected with a balanced detector, where the two signals are subtracted and thus the noise of the laser source itself is canceled out. By means of a delay line the reference beam can be shifted against the actual probe beam to synchronize the beams and thus optimize the noise cancellation. The entrance of the balanced detector is covered with a band pass filter, which only transmits the probe wavelength to ensure the stray light of the pump laser not to distort the measurement signal. The measurement signal generated at the balanced detector is detected with a fast oscilloscope which is triggered by the signal of the fast photo diode. Because the relative signal change is

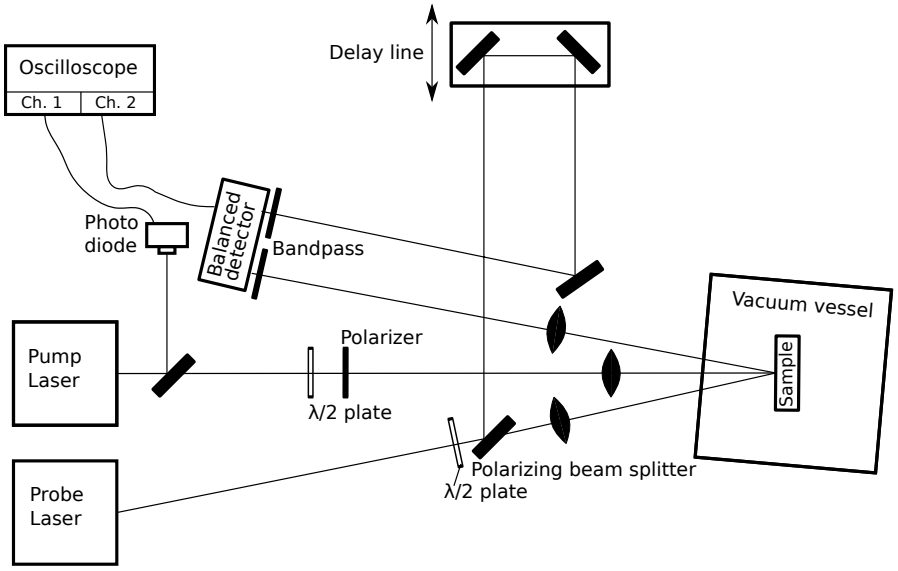

Figure 5.1: Scheme of the experimental setup developed to measure the thermal response of diamond to pulsed laser irradiation. The initial pump beam is split into a small fraction which triggers the measurement and the actual pump beam. The actual pump beam can be attenuated by the arrangement of a $\lambda/2$ waveplate and a linear polarizer and is then focused on the sample. The probe beam is variably split into an actual probe beam and a reference beam. The actual probe beam is then focused on the sample and subtracted from the reference beam by the balanced detector. The variable beam splitter and the delay line are adjusted in a way that the balanced detector receives a copy of the unperturbed (without the influence of the pump beam) probe beam.

Table 5.1: Parameters of the laser system

Parameter	**Unit**	**Value**
Pump wavelength	m	$213 \cdot 10^{-9}$
Pump spot radius (2σ)	m	$200 \cdot 10^{-6}$
Pump pulse duration	s	$1.00 \cdot 10^{-9}$
Pump pulse energy	J	$1.00 \cdot 10^{-6}$
Pump pulse rep. rate	Hz	$1.00 \cdot 10^{3}$
Probe wavelength	m	$532 \cdot 10^{-9}$
Probe spot radius (2σ)	m	$40.0 \cdot 10^{-6}$

only of the order of 10^{-5} the measured signal has to be averaged over tens of thousands of pump pulses to yield a reasonable signal to noise ratio. In order to investigate the properties of the sample at cryogenic temperatures the sample is placed into a vacuum vessel. The vacuum is necessary to inhibit convective and conductive heat transport thought the air and to minimize adsorption of water, oil or other contaminations at the sample surface.

5.3 Analysis of the Data

During the first analysis of the data the probe signal turned out to consist of two components. A fast decaying and a slow decaying component. The first and fast decaying component represents the signal of interest, proportional to the temperature and the second component is caused by some long lifetime electronic states which are exited by the UV pump laser [Thomsen et al., 1986]. These states originate from lattice defects or impurities such as nitrogen [Khan et al., 2009]. Because of the long lifetime of these electronic states this two components can be separated from each other without any appreciable degradation of the temperature signal quality. In figure 5.2 the raw signal is shown over 200 µs. At $t = 0$ the pump pulse arrives and a fast decay of hundreds of nanoseconds is superimposed by a slowly decaying signal. In the analysis of the data this slowly decaying signal U_{el} is modeled as an exponential function with an offset of the form

$$U_{\mathrm{el}}(t) = U_{\mathrm{el}}^{(0)} + U_{\mathrm{el}}^{(1)} \cdot \exp\left(\frac{t}{\tau_{\mathrm{el}}}\right). \tag{5.3}$$

The parameters of the electronic component of the probe signal $U_{\mathrm{el}}^{(0)}$, $U_{\mathrm{el}}^{(1)}$ and τ_{el} can be measured by performing a fit of the model (5.3) to the long term signal shown in fig. 5.2. To exclude the influence of the thermal component from that fit and hence to obtain

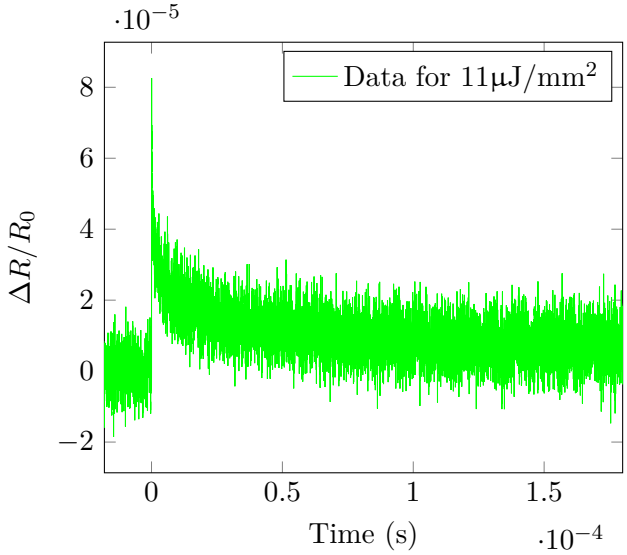

Figure 5.2: Decay of the background signal.

the proper values for $U_{\mathrm{el}}^{(0)}$, $U_{\mathrm{el}}^{(1)}$ and τ_{el} only the data $t \gtrsim 2$ µs are used for the fit. This could be done because under the existing conditions even with a thermal conductivity much worse than that of diamond at room temperature the thermal component of the probe signal is almost completely decayed at about 2 µs and hence can be neglected afterwards. When $U_{\mathrm{el}}(t)$ is known, it can be incorporated into the final model $U_{\mathrm{pr}}(t)$ for the probe signal. The probe signal can then be modeled as

$$U_{\mathrm{pr}}(t) = U_{\mathrm{el}}(t) + U_{\mathrm{th}}(t), \tag{5.4}$$

where U_{th} represents the model function for the thermal component of the probe signal. The thermal component of the probe signal in turn is a function of the applied thermal model T_{mod}. In this thermal model the apparent thermal conductivity λ_{ap} is left as a free parameter because this is the quantity of interest in the measurements presented in this chapter. The model function for the probe signal can then be expressed as

$$U_{\mathrm{pr}}(\kappa_{\mathrm{th}}, \lambda_{\mathrm{ap}}, t) = U_{\mathrm{el}}(t) + U_{\mathrm{th}}(\kappa_{\mathrm{th}}, T_{\mathrm{mod}}(\lambda_{\mathrm{ap}}, t)), \tag{5.5}$$

where κ_{th} is the thermoreflectance calibration coefficient. By fitting the model U_{pr} to the measured probe data a value for λ_{ap} can be obtained. In this work two different model functions, which are presented below in section 5.3.1, are used to fit to the data.

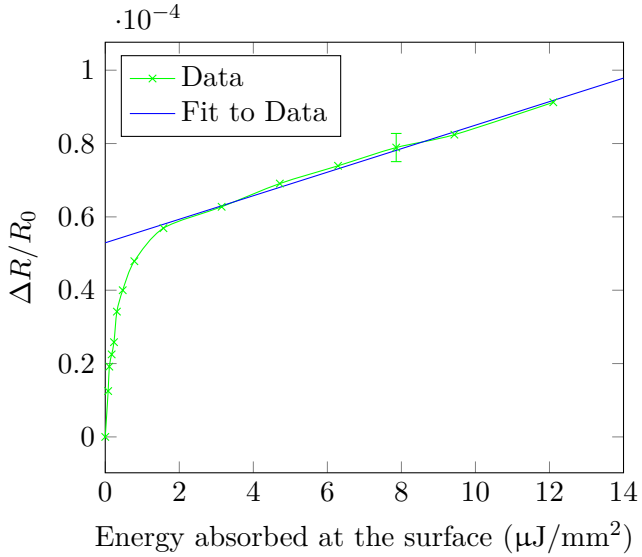

Figure 5.3: Peak signal as a function of the pump pulse energy absorbed at the surface. The error bar shown applies to all data points. The linear fit displays the linear relationship between thermal component of the signal and the pump laser pulse energy. The green interpolating line is plotted to guide the eye.

To show the proportionality between the pump energy and the probe signal and thus to validate the measurement method the relation between input (pump) and output (probe) was measured and is shown in figure 5.3. The pump pulse energy was varied and the resulting probe signal jump (the peak signal) was measured. Here again the influence of the two signal components can be seen. Below 1 μJ/mm^2 the signal increase is dominated by the long lifetime signal. Above 1 μJ/mm^2 the long lifetime signal starts to saturate and above 2 μJ/mm^2 the signal increase is dominated by the thermal short lifetime signal. A linear fit starting above 2 μJ/mm^2 was done, which is indicated by the blue line in figure 5.3. Comparing the line with the data above 2 μJ/mm^2 shows a good proportionality of the thermal component between pump and probe beam, when the y-intercept of the line (the long lifetime component) is subtracted from the data.

5.3.1 Thermal Models

There are two thermal models used to analyze the measured data. The first model is based on the classical heat equation (HE) and the second is based on the hyperbolic heat

equation.[44] It is generally understood that both the HE and the HHE are only valid for diffusive heat transport. The reason for the first model to be used is to investigate the assumed failure of the classical heat equation in case of ballistic phonon heat transport (cf. sec. 3.4.3.2). The reason for the second model to be used is to experimentally demonstrate the validity of the hyperbolic heat equation for transient ballistic thermal transport. Even though the HHE is known for decades [Cattaneo, 1958] this issue still remains to be investigated because only recently it was shown theoretically [Maassen and Lundstrom, 2015], that the HHE covers ballistic to diffusive transient heat transport. Both models represent a solution of the HE and HHE respectively in time and one spatial dimension. In both cases the spatial dimension is the cross-plane direction of the sample, which is assumed to be semi-infinite. The simplification to the one spatial dimension and to the semi-infinite sample in this dimension is valid because in the experiment the penetration depth of the radiation is much less than the pump beam radius and the thickness of the used sample. Furthermore the thickness of the sample is required to be large compared to the mean free path of the phonons.

The first model used is an entirely analytic solution of the classical heat equation [Yilbas and Al-Aqeeli, 2004]. With the mass density ρ, the specific heat C_p, the thermal diffusivity α and the absorption coefficient of the laser radiation κ_ν the model is given by

$$T(0,t) = \frac{I_1\kappa_\nu}{\rho C_\mathrm{p}} \left\{ \frac{(\gamma-\beta)\exp(\alpha\kappa_\nu^2 t)}{(\beta+\alpha\kappa_\nu^2)\,(\gamma+\alpha\kappa_\nu^2)} \operatorname{erfc}\!\left(\kappa_\nu\sqrt{\alpha t}\right) - \left[\frac{\exp\left(-\beta t\right)}{\beta+\alpha\kappa_\nu^2} - \frac{\exp\left(-\gamma t\right)}{\gamma+\alpha\kappa_\nu^2}\right] \right.$$
$$\left. +2\kappa_\nu\sqrt{\frac{\alpha}{\pi\beta}}\frac{\mathrm{F}(\sqrt{\beta t})}{\beta+\alpha\kappa_\nu^2} - 2\kappa_\nu\sqrt{\frac{\alpha}{\pi\gamma}}\frac{\mathrm{F}(\sqrt{\gamma t})}{\gamma+\alpha\kappa_\nu^2} \right\}. \quad (5.6)$$

Here $\mathrm{F}(x)$ is the Dawson's integral and β, γ, I_1 and κ_ν are parameters characterizing the volumetric heat source, which determines the absorbed radiation power of the laser pulse. The respective heat source is described by

$$P_V(x,t) = I_1\kappa_\nu\left[\exp(-\beta t) - \exp(-\gamma t)\right]\exp(-\kappa_\nu x), \quad (5.7)$$

where P_V is the absorbed volumetric radiation power density of the laser pulse.[45]

[44] Both heat equations are derived from the BTE in section 3.4.3.1 and the difference between the HE and the HHE is shown in equation (3.55).

[45] The expression (5.7) describes the temporal end spatial distribution of the absorbed power in the crystal, as assumed by the model (5.6). The expression in the square brackets is proportional to the power of the laser pulse and the exponential function outside the square brackets represents the absorption characteristic of the laser radiation as a function of the distance x from the surface.

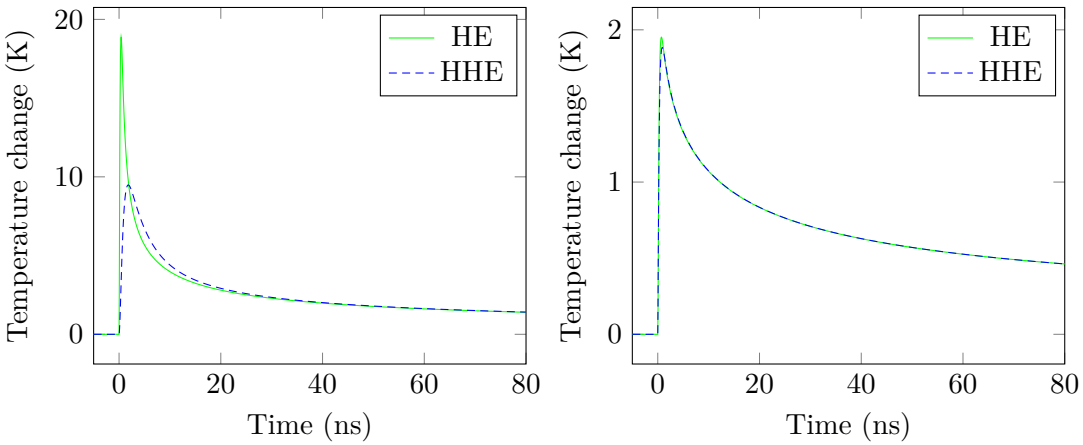

Figure 5.4: Surface temperature of a laser irradiated diamond crystal at 100 K (left) and 300 K (right) as predicted by the HE and HHE. The respective laser parameters are taken to be the same as in the experimental setup and can be found in table 5.1.

The second model represents a semi-analytic solution of the hyperbolic heat equation [Yilbas et al., 2011], which is given by

$$U(s,t) = \sqrt{\frac{2}{\pi}} \frac{I_1 \kappa_\nu}{(\kappa_\nu^2 + s^2)(A\beta^2 - B\beta + s^2)} \cdot \left[\exp(-\beta t) - \exp\left(-\frac{Bt}{2A}\right) \right.$$
$$\left. \cosh\left(\frac{t\sqrt{B^2 - 4As^2}}{2A}\right) + \frac{2A\beta - B}{\sqrt{B^2 - 4As^2}} \exp\left(-\frac{Bt}{2A}\right) \sinh\left(\frac{t\sqrt{B^2 - 4As^2}}{2A}\right) \right], \quad (5.8)$$

where the constants A and B and the volumetric heat source are defined by

$$A = \frac{1}{v_x^2}, \qquad B = \frac{\rho C_\mathrm{p}}{\lambda_\mathrm{th}} = \frac{1}{\alpha}, \qquad P_V(x,t) = I_1 \kappa_\nu \exp(-\beta t) \exp(-\kappa_\nu x). \quad (5.9)$$

Here the nomenclature is identical to that of the first model. The only additional parameter is the angle averaged phonon velocity in x-direction v_x. In contrast to the classical use of the HHE, v_x is related to the sound velocity by $v_x = v_\mathrm{s}/2$ instead of $v_x^2 = v_\mathrm{s}^2/3$ as in the classical case. The final solution can be obtained by an inverse Fourier-cos transform, which yields

$$T(x,t) = \sqrt{\frac{2}{\pi}} \int_0^\infty U(s,t) \cos(sx)\, \mathrm{d}s. \quad (5.10)$$

For this integral no analytic expression can be found and hence numerical methods were applied to solve that equation.

In figure 5.4 the solution of the classical heat equation and the hyperbolic heat equation at 100 K and 300 K is compared. The figures compare the predicted temperature evolution at the surface of a diamond crystal irradiated by a laser pulse. It can be seen that the equations yield almost the same results at 300 K. The reason for this is that the HE can be considered as a special case of the HHE. The difference between both equations is the $\tau(\partial^2 T/\partial t^2)$ term (cf. eq. (3.55)), which becomes very small when the phonon relaxation time τ approaches zero (cf. sec. 3.4.3.1). This is practically the case[46] at room temperature. At 100 K, where the phonon relaxation time is of the order of the time scale of interest, the HE deviates significantly from the HHE only in the early phase after arrival of the laser pulse. After the initial deviation the solution of the HHE converges to the solution of the HE. This happens because the $(\partial^2 T/\partial t^2)$ term of the HHE starts to approach zero after some time and thus the two solutions start to become equivalent. In figure 5.5 the solution of the HE and HHE is shown as a function of the distance from the surface. The different plots represent the cases for 100 K and 300 K at two different points in time each. Here again at 300 K the solutions of HE and HHE are almost identical. At 100 K the HHE shows a wavefront which propagates with $v_\mathrm{s}/2$ into the crystal. The reason for this unphysical wavefront is the assumed angle discretisation of the phonons into a forward and backward stream with a single x-projected phonon velocity and mean free path (cf. eq. (3.61)). In a solution of the full phonon Boltzmann transport equation this wavefront would be smoothed out because of the different phonon angles, which would result in different x-projected mean free paths. At 100 K and 3 ns the HE shows an unphysical fast phonon propagation. This unphysical behavior is always present but in most cases negligible. Resolving this issue was the original reason to derive the HHE [Cattaneo, 1958], which reduces the infinite heat propagation velocity to the more realistic average x-projected velocity of the phonons.

5.4 Results of the Measurement

The pump-probe measurements were performed with a single crystal CVD diamond plate of type IIa [Element Six, 2017] with a thickness of 300 µm at different temperatures ranging from 340 K down to 100 K. The measurement data represent an average of thousands of single pump-probe measurements, taken with the setup described in section 5.2. The averaging is required to achieve a reasonable signal to noise ratio, which is proportional to the square-root of the number of single measurements. In figure 5.6

[46] In relation to the time scale of interest.

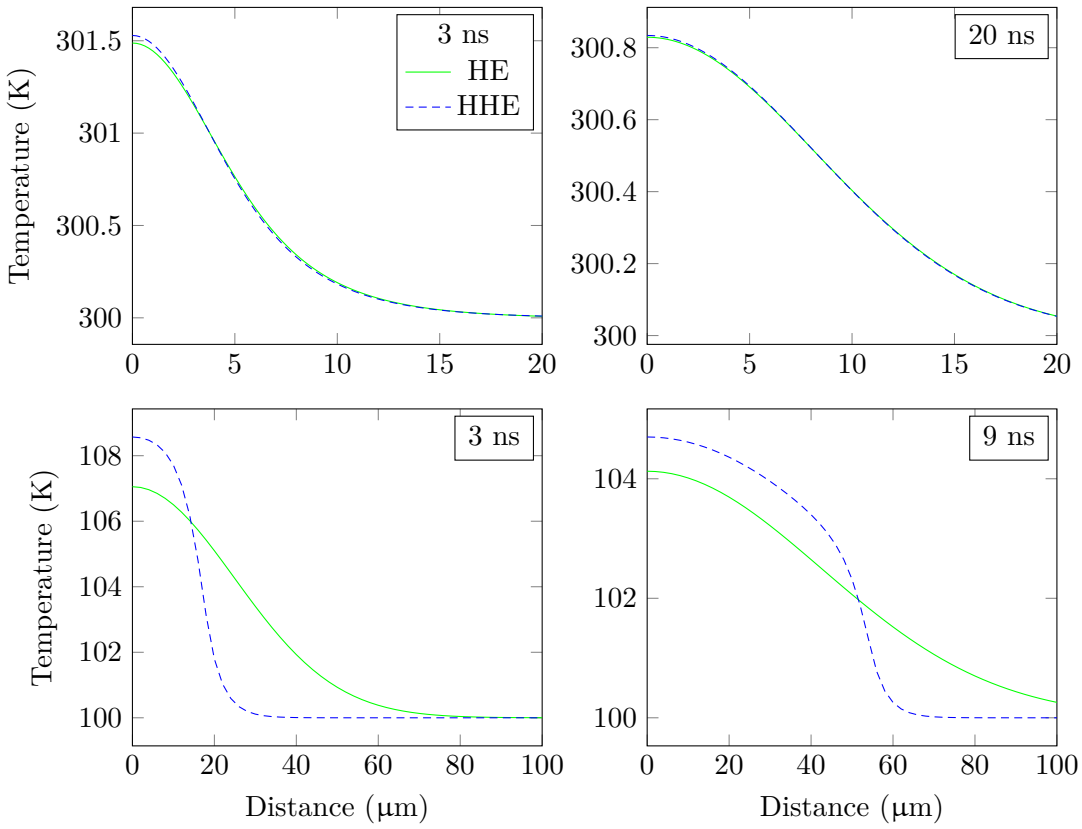

Figure 5.5: Comparison of the HE and HHE applied to a laser irradiated diamond crystal at 100 K (bottom row) and 300 K (top row). The x-axis represents the distance from the surface of the crystal. The respective laser parameter are taken to be the same as in the experimental setup and can be found in table 5.1.

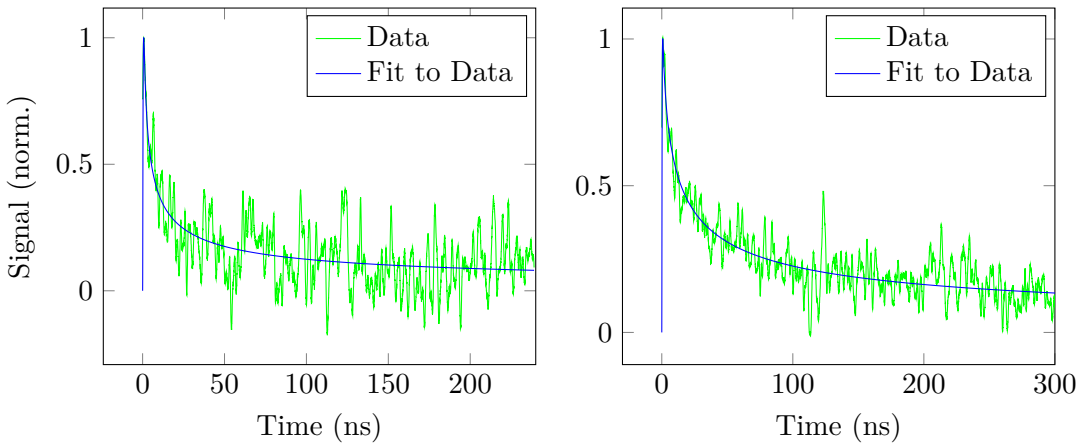

Figure 5.6: Comparison of a pump-probe measurement at 150 K (left) and 297 K (right). The fit to the data is based on the classical heat equation.

measurements[47] at 150 K and 297 K are compared. The fit to the data also shown is based on the classical heat equation (Model (5.6)). It can be seen that the temperature decay at the crystal surface is considerably more rapid at 150 K than at 297 K. The reason for this is the increased thermal diffusivity α at lower temperatures[48], which in turn is attributed to the increased thermal conductivity and the decreased specific heat at lower temperatures (cf. sec. 3.4.1 and 3.4.2).

5.4.1 Failure of the Classical Heat Equation

As described above the apparent thermal conductivity of a system can be obtained by fitting a thermal model, which has the (apparent) thermal conductivity as a free parameter, to a respective set of data. This was done for the whole data set which included pump-probe measurements at temperatures ranging from 340 K down to 100 K. The thermal model (5.6) based on the classical heat equation was used in this section to fit the data. Figure 5.7 shows a comparison of the extracted (apparent) thermal conductivity and the literature bulk thermal conductivity of a single crystal CVD diamond sample. The literature values and the fit to the literature values are taken from [Element Six, 2017] and [Wiedemann, 2017]. It can be seen that at temperatures from 340 K down to 250 K the bulk values are almost equal to the measured apparent thermal conductivity. From 250 K towards lower temperatures the apparent thermal conductivity starts to

[47] Shown is only the thermal component of the signal (see section 5.3 for details).
[48] See equation (5.9) for the definition of α.

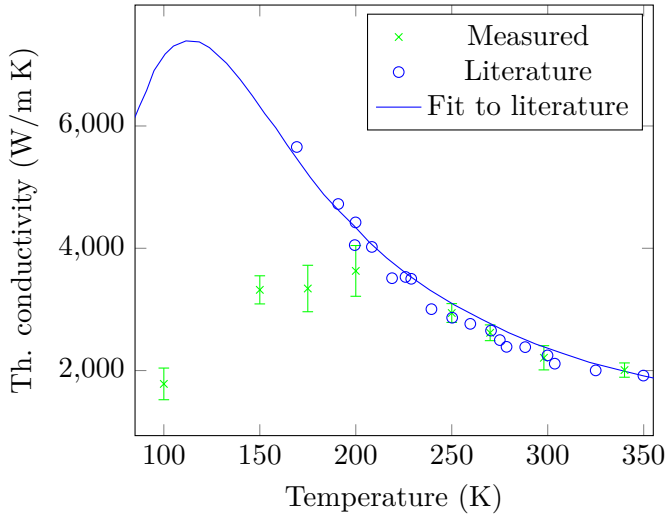

Figure 5.7: Bulk thermal conductivity compared to measured (apparent) thermal conductivity of diamond. The apparent thermal conductivity was obtained by fitting the model (5.6), which is based on the classical heat equation, to the measured data. The bulk thermal conductivity and the respective fit to the data are taken from literature [Element Six, 2017; Wiedemann, 2017].

differ more and more from the bulk values. At 100 K the apparent thermal conductivity is only about 20% of its bulk value. In figure 5.8 (left) the same issue is depicted in a different way. The figure shows the apparent thermal conductivity normalized to the bulk values as a function of temperature. Here the normalized apparent thermal conductivity is used as a measure for the degree of deviation from the bulk values. This deviation occurs because of a failure of the classical heat equation (where the applied fit model is based on) and therefore the normalized apparent thermal conductivity can be interpreted as a measure for the validity of the classical heat equation or as a measure for the degree of ballistic heat conduction effects. The classical heat equation is valid and the heat conduction is purely diffusive, if the normalized apparent thermal conductivity is about 1, otherwise it is not. The reason for the failure at low temperatures is the increasing mean free path (MFP) of the phonons with decreasing temperature (cf. fig. 3.7), which causes the classical heat equation to fail when the MFP reaches the order of the characteristic length scale of the system. In the present case the characteristic length scale is the absorption length of the pump laser radiation, which is about 3.5 µm. The failure mechanism is most likely the so called gradient effect described in section 3.4.3.2 and illustrated in figures 3.11 and 3.12. A good evidence for the gradient effect

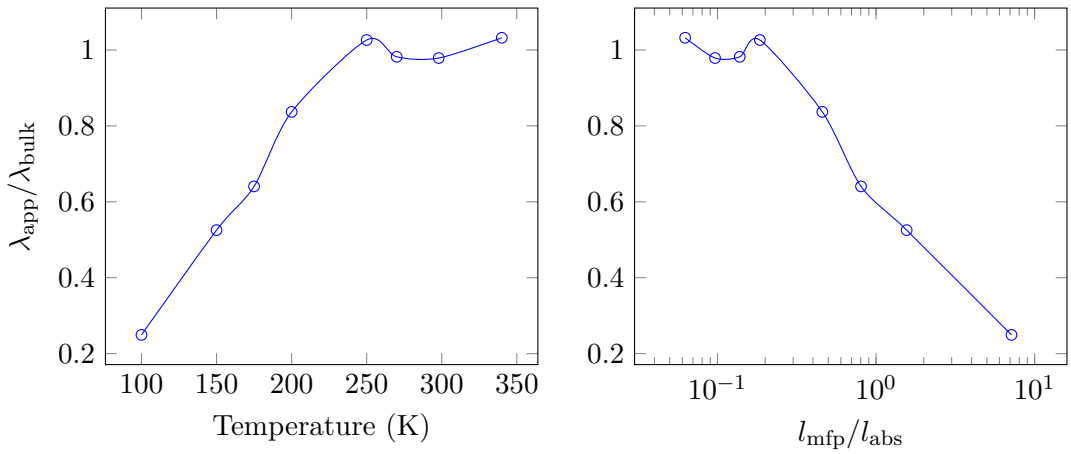

Figure 5.8: Apparent thermal conductivity normalized on the bulk values as a function of temperature (left). Apparent thermal conductivity normalized to the bulk values as a function of the phonon mean free path normalized to the characteristic length scale of the system (right). In this case the characteristic length scale of the system is identified as the absorption length of the pump radiation, which is about 3.5 µm. The interpolating lines are plotted to guide the eye.

as the failure mechanism is shown in figure 5.8 (right), which shows the normalized apparent thermal conductivity versus the absorption length of the pump laser radiation normalized to the average MFP of the phonons.[49] It can be seen that the classical heat equation starts to fail when the MFP of the phonons reach the absorption length of the crystal. This result confirms the original hypotheses in terms of the failure of the classical heat equation in diamond and quantizes its failure.

5.4.2 Fitting the HHE to the Data

The results reported in this section are obtained by applying the same procedure as in the previous section to the same set of data but in the present case the model (5.8), which is based on the hyperbolic heat equation was used to fit to the data. Figure 5.9 shows – like figure 5.7 – a comparison between the bulk thermal conductivity and the measured (apparent) thermal conductivity. The bulk thermal conductivity and the respective fit to the data shown in figure 5.9 are taken from literature [Element Six, 2017; Wiedemann, 2017]. Even though the data set is identical to the results presented

[49] The mean free path as a function of temperature was calculated from equation (3.39) and is shown for two different diamond crystals in figure 3.7.

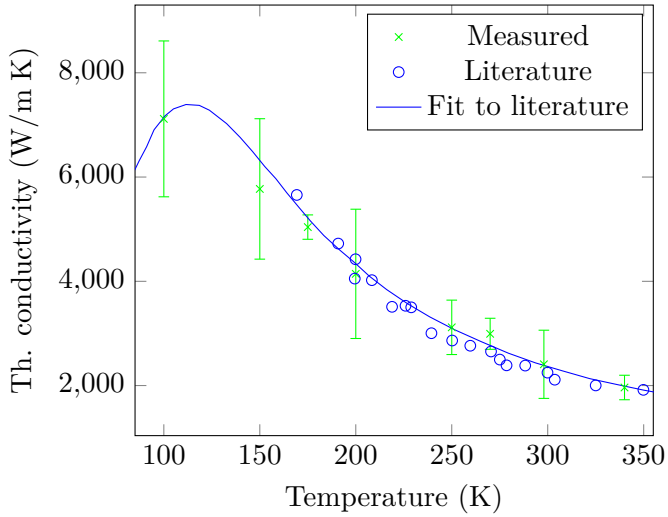

Figure 5.9: Bulk thermal conductivity compared to measured (apparent) thermal conductivity of diamond. The apparent thermal conductivity was obtained by fitting the model (5.8), which is based on the hyperbolic heat equation, to the measured data. The bulk thermal conductivity and the respective fit to the data are taken from literature [Element Six, 2017; Wiedemann, 2017].

in figure 5.7 the uncertainty of the measurement (the error bars) is significantly larger. The reason for this is that the model based on the HHE is more sensitive to changes in the (apparent) thermal conductivity because the thermal conductivity also determines the relaxation time τ of the phonons – a parameter which is not existent in the classical heat eqation. In figure 5.9 it is also shown, that within the uncertainty of the measurement the bulk thermal conductivity is completely reproduced by the measured (apparent) thermal conductivity. Following the argumentation of the previous sections this means, that the applied thermal model is valid for the investigated heat transfer problem from the ballistic to the diffusive regime. Even though it was recently shown, that the HHE can be written as a simplification of the Boltzmann transport equation (BTE) this is not an obvious result because here the HHE is additionally just used in the gray approximation.[50] The gray approximation was required because the temperature dependent mean free path spectrum of diamond is unknown. Thus the measurements also show, that the severe simplifications made (compared to the full BTE) are still not oversimplifying the present problem.

[50] A single, mode independent phonon velocity and relaxation time.

5.4.3 Revaluation of the Strain Generation at Cryogenic Temperatures

In section 4.3.3 it was shown, that under the assumption of an instantaneous and localized conversion from electromagnetic to thermal energy the generated initial surface strain does only have a weak dependence on the base temperature (the initial Temperature before the radiation was absorbed). However in the previous section 5.4.2 it could be shown, that the hyperbolic heat equation reproduces the measurements at all base temperatures. Comparing the left and right plot of figure 5.4 shows that in the ballistic heat conduction regime the temperature rise predicted by the HHE is much less and delayed compared to the temperature rise predicted by the classical heat equation. Therefore according to the measurements the peak temperature and thus the generated peak strain at cryogenic temperatures are considerably less than predicted by equation (3.19) and (4.4), which do not even consider heat conduction.

5.5 Conclusion

In this chapter the development of a measurement setup, which can serve as a basis for future XFELO diamond optics development, was presented. In addition first measurement results were shown and the data have been used to evaluate two different heat transfer models – the classical heat equation and the hyperbolic heat equation. The evaluation of the classical heat transfer model (based on Fourier's law) resulted in a confirmation of its failure in a particular situation and a quantification of that failure. The assumed failure mechanism could be supported by comparing the temperature dependent average mean free path of the phonons with the degree of failure. The evaluation of the model based on the hyperbolic heat equation showed, that this model reproduces the measurements for all temperatures. Both model evaluations are very valuable for future modeling of XFELO mirrors. However the hyperbolic heat equation should be tested in various situations – as close as possible to the real XFELO conditions and with a lower measurement uncertainty – before used routinely for the modeling of ballistic heat conduction effects in an XFELO cavity mirror. For example the effect of boundary scattering, described in section 3.4.3.2, was not investigated in this study but can in principle also be covered by the hyperbolic heat equation. The boundary scattering becomes potentially important for thin crystals at low temperature. Those crystals can be used to couple the radiation out of the cavity.

Another important result is that the heat transfer equation applied in earlier heat transfer simulations [Zemella et al., 2012] could be validated for the considered problem

by the measurement results. Even though the simplifying assumption of an uniform radiation absorption in the crystal is questionable the applied heat equation was shown to be appropriate on the considered timescale. The earlier studies were based on the classical heat equation and addressed the effect of accumulating x-ray pulses within a bunch train. The simulations focused on the moment just before the absorption of the subsequent x-ray pulse, which implies a time scale of hundreds of ns. Since the validated hyperbolic heat equation converges after a fraction of that time scale to the classical heat equation (cf. fig. 5.4 and 5.5) the applied heat equation in the simulations by [Zemella et al., 2012] which focus on the moment just before the absorption of the subsequent x-ray pulse can be assumed to be validated as well.

6 Conclusion

In this work different aspects of an XFELO were considered, but the focus was clearly on the investigation of the influence of absorbed x-ray power on the Bragg reflection.

In section 4.1 a magnetic chicane was developed to couple the electron beam into the XFELO cavity. The results show that an appropriate chicane and focusing section can be built within a beam line length of about 35 m using normal conducting standard magnets already used in the linear accelerator of the European XFEL.

In section 4.2 the influence of electron bunch arrival time jitter on the XFELO process was studied. It turned out that the levels of arrival time jitter which can be achieved with today's technology are low enough to allow stable XFELO operation for all electron bunch lengths. Furthermore, by means of the simultaneous simulation of arrival time jitter, angular jitter and positional jitter it was shown that it should be possible to run an XFELO under electron bunch jitter conditions expected for the European XFEL.

In section 4.3 the thermal and elastic strain generated by a typical XFELO laser pulse in a diamond Bragg mirror was simulated. In addition the effect of the obtained time-dependent strain profile on the Bragg reflection was simulated. In this study it could be shown, that a typical XFELO pulse considerably distorts, broadens and shifts the Bragg reflectivity curve. The current results are considerably different from the results of previous studies, which used a model apparently oversimplifying the problem, because in the previous studies only a constant thermal and no elastic strain was assumed. Another important outcome is, that the strain generated by a laser pulse is independent (to first order) of the crystal base temperature, if heat conduction effects can be neglected.

In chapter 5 the development of a pump-probe measurement setup, which can serve as a basis for future XFELO diamond optics development, was presented. First measurements were shown, which confirmed the method of the measurement. A method for analyzing the data was developed which enabled the extraction of the apparent thermal conductivity from the data. Pump-probe Measurements at crystal base temperatures from 100 K to 340 K were performed and the apparent thermal conductivity for two different heat transport equations – the classical heat equation and the hyperbolic heat equation – were extracted. By comparing the apparent thermal conductivity with the bulk thermal conductivity it could be shown that the classical heat equation fails below

about 200 K. Furthermore it could be shown that the apparent thermal conductivity extracted from the hyperbolic heat equation reproduce (within the uncertainty of the measurement) the bulk thermal conductivity for all temperatures from 100 K to 340 K. This means that the hyperbolic heat equation has been validated for the whole temperature range of the measurement for the given heat transfer problem, which makes that equation a promising candidate for future heat transfer modeling of cryogenic XFELO mirrors.

6.1 Outlook

The results presented in this work constitute a solid basis for future development in the field of pulsed heat load subjected Bragg mirrors. The results are valuable for both, the refinement of numerical simulations and further experimental studies.

On the basis of the numerical studies presented in section 4.3 the effect of the cumulated absorption of several laser pulses on the Bragg reflection should be studied, in extension to the single pulse case considered in section 4.3. Furthermore the Doppler shift of the x-rays reflected from the running strain pulse should be considered in future simulations. In addition it should be studied if the running strain pulse in the crystal can be technically damped or deflected away from the zone, where the x-ray beam interacts with the crystal.

The experimental results presented in chapter 5 should be reproduced with a better signal-to-noise ratio to reduce the uncertainty of the measurement. This is especially important for the fit of the model, based on the hyperbolic heat equation, to the data. The signal-to-noise ratio can be improved by averaging over more single measurements, as it was done so far. Moreover, with the experimental setup further ballistic heat conduction effects can be studied, including the boundary scattering effect and the transversal gradient effect, which occurs when the mean free path of the phonons is of the order of the laser beam radius. In addition to these heat conduction studies the experimental setup can probably be modified to detect the generated elastic train pulses as well. This could be done by adding a spectrometer with a sufficient resolution in front of the balanced detector. With this setup the signal of the running strain in the crystal could be separated from the signal of the thermal strain due do the Doppler shift of the radiation reflected at the running strain pulse.

Acronyms

BTE	Boltzmann transport equation
CVD	Chemical vapor deposition
CW	Continuous wave
DC	Direct current
DESY	Deutsches Elektronen-Synchrotron
FEL	Free electron laser
FELO	Free electron laser oscillator
FLASH	Free-Electron LASer in Hamburg
HE	Heat equation
HGHG	High-gain harmonic generation
HHE	Hyperbolic heat equation
IR	Infrared
laser	Light amplification by stimulated emission of radiation
LCLS	Linear Coherent Light Source
LINAC	Linear accelerator
MFP	Mean free path
MSM	McKelvey-Schockley flux method
RF	Radio frequency
RMS	Root-mean-square

SASE . . . . . Self-amplified spontaneous emission

SRF . . . . . Superconducting radio frequency

UV . . . . . Ultra violet

XFEL . . . . . X-ray free electron laser

XFELO . . . . . X-ray free electron laser oscillator

Notation

a	Lattice constant
A	Irradiated area
$\boldsymbol{B}$	Magnetic induction
B_0	Peak magnetic field of undulator
B	Incompressibility modulus
c	Speed of light
c_l	Contribution of the normal mode $\boldsymbol{k}$,p to the heat capacity
c_v	Specific heat at constant volume
C_l	Lattice heat capacity
C_p	Specific heat capacity
C	Elasticity tensor
d_H	Distance between lattice planes
d	Differential
D	Number of modes per unit volume
$\boldsymbol{e}_y$	Unit vector in y direction
e	Elementary charge
E	Magnitude of the electric field
E_p	Laser pulse energy
$\boldsymbol{F}$	Force

F . . . . . Phonon flux along $\pm x$

G . . . . . Gain

$\hbar$ . . . . . Reduced Planck constant

$\boldsymbol{H}$ . . . . . Reciprocal lattice vector

i . . . . . Imaginary unit

I_ω . . . . . Radiative intensity of the mode ω

I_ω^0 . . . . . Radiative intensity at thermal equilibrium

J . . . . . Bessel functions

k_u . . . . . Undulator wave number

k_l . . . . . Wave number of FEL radiation

$\boldsymbol{k}$ . . . . . Wavevector

k_B . . . . . Boltzmann constant

K . . . . . Undulator parameter

$\hat{K}$ . . . . . Modified undulator parameter

K . . . . . Spring constants

Kn . . . . . Knudsen number

k . . . . . Magnitude of the medium wave vector

l_ext . . . . . Extinction length of the radiation

l . . . . . Mean free path between collisions

l_pp . . . . . Mean free path between phonon - phonon collisions

l_b . . . . . Bulk mean free path

l_x . . . . . Mean free path for back-scattering along x

L_g0 . . . . . Power gain length (idealized for 1D)

L . . . . . Characteristic size of a medium

m_e . . . . . Electron mass

M . . . . . Mass of individual atom

n_e . . . . . Electron density

n_ω^0 . . . . . Equilibrium distribution of Ph. with angular frequency ω

n_ω . . . . . Average number of phonons with angular frequency ω

$\tilde{n}$ . . . . . Complex index of refraction

n' . . . . . Real part of complex index of refraction

n'' . . . . . Imaginary part of complex index of refraction

N_u . . . . . Number of undulator periods

N . . . . . Number of atoms in a crystal

p . . . . . Polarization index of the mode

P_sp . . . . . Total power of spontaneous und. radiation

P . . . . . Power

P . . . . . Pressure

$\boldsymbol{q}$ . . . . . Heat current

q_x . . . . . x-component of heat current

$\boldsymbol{q}_\mathrm{NL}$ . . . . . Nonlocal heat current

r_b . . . . . Electron beam radius

$\boldsymbol{r}$ . . . . . Position vector in real space

R . . . . . Radius of curvature

R . . . . . Reflectance

$\Re$ . . . . . Real part of a complex number

$\boldsymbol{s}$ . . . . . Unit vector

t . . . . . Time

T	Temperature
T_{avg}	Average temperatu
T_{mod}	Thermal model
u	Mechanical displacement
u_{l}	Specific internal energy
U_{l}	Total internal energy
$U_{\mathrm{l}}^{\mathrm{eq}}$	Potential energy of the static equilibrium position
U_{el}	Electronic contribution of the probe signal
$U_{\mathrm{el}}^{(0)}$	Constant electronic contribution of the probe signal
$U_{\mathrm{el}}^{(1)}$	Amplitude of electronic contribution of the probe signal
U_{pr}	Probe signal
U_{th}	Thermal signal
$\bar{v}$	Magnitude of average velocity
$\boldsymbol{v}$	Velocity
v	Magnitude of the velocity
v_{s}	Speed of sound
v_ω	Group velocity of phonons with angular frequency ω
v_k	Group velocity of phonons with wavevektor $\boldsymbol{k}$
v_x	Group velocity of phonons along x
V	Volume
W	Energy
W_{r}	Resonance electron energy
W_{l}	Energy of light wave
x	x-component of coordinate system

y . . . . . y-component of coordinate system

z . . . . . z-component of coordinate system

α . . . . . Thermal diffusivity

β . . . . . Thermal expansion coefficient

δ . . . . . Kronecker delta

ϵ_B . . . . . Rel. spectral width of the Bragg reflection

η . . . . . Mechanical strain

ϵ_0 . . . . . Vacuum permittivity

η_0 . . . . . Amplitude of induced strain

ϵ . . . . . Phonon energy

$\tilde{\epsilon}$ . . . . . Complex dielectric function

γ . . . . . Lorentz factor

γ_r . . . . . Lorentz factor of resonance electron energy

γ . . . . . Grüneisen parameter

$\gamma_{\boldsymbol{k}p}$ . . . . . Grueneisen parameter for the mode $\boldsymbol{k}$,p

Γ . . . . . FEL gain parameter

Γ . . . . . Heaviside step function

κ_ν . . . . . Optical absorption coefficient

κ_ac . . . . . Acoustic absorption coefficient

κ_th . . . . . Thermoreflectance calibration coefficient

λ_B . . . . . Bragg wavelength

λ_u . . . . . undulator period

λ_l . . . . . Wavelength of undulator / FEL radiation

λ_th . . . . . Heat conductivity

λ_{eff} . . . . . Effective heat conductivity

λ_{b} . . . . . Bulk heat conductivity

$\lambda^{0}_{\mathrm{th}}$ . . . . . Heat conductivity of diffusive phonons

λ_{ap} . . . . . Apparent thermal conductivity

μ_0 . . . . . Vacuum permeability

μ . . . . . Cosine between ray and x-axis

ω_{c} . . . . . Critical frequency

ω_{u} . . . . . Undulator angular frequency

ω . . . . . Angular frequency

ω_{l} . . . . . Angular frequency of light

ω_{D} . . . . . Debye angular frequency

π . . . . . Circular constant

ψ_0 . . . . . Zero phase

ψ . . . . . Pondermotive phase

ϕ . . . . . Angle between ray and x-axis

ρ . . . . . Mass density

σ_θ . . . . . RMS opening angle of emission cone

σ . . . . . Mechanical stress

τ . . . . . Time constant

τ_ω . . . . . Average time between collisions

τ_{el} . . . . . Time constant of electronic probe contribution

θ_{B} . . . . . Bragg angle

θ_{cone} . . . . . Opening angle of radiation emission

θ . . . . . Emission angle of the radiation

θ_{D} . . . . . Debye temperature

ξ . . . . . Frequency deviation

Bibliography

Ackermann, S., Azima, A., Bajt, S., Bödewadt, J., Curbis, F., Dachraoui, H., Delsim-Hashemi, H., Drescher, M., Düsterer, S., Faatz, B., Felber, M., Feldhaus, J., Hass, E., Hipp, U., Honkavaara, K., Ischebeck, R., Khan, S., Laarmann, T., Lechner, C., Maltezopoulos, T., Miltchev, V., Mittenzwey, M., Rehders, M., Rönsch-Schulenburg, J., Rossbach, J., Schlarb, H., Schreiber, S., Schroedter, L., Schulz, M., Schulz, S., Tarkeshian, R., Tischer, M., Wacker, V., and Wieland, M. (2013). Generation of coherent 19- and 38-nm radiation at a free-electron laser directly seeded at 38 nm. *Phys. Rev. Lett.*, 111:114801. 2.1.1

Adams, B. W. and Kim, K.-J. (2015). X-ray comb generation from nuclear-resonance-stabilized x-ray free-electron laser oscillator for fundamental physics and precision metrology. *Phys. Rev. ST Accel. Beams*, 18:030711. 1.1

Allaria, E., Appio, R., Badano, L., Barletta, W. A., Bassanese, S., Biedron, S. G., Borga, A., Busetto, E., Castronovo, D., Cinquegrana, P., Cleva, S., Cocco, D., Cornacchia, M., Craievich, P., Cudin, I., D'Auria, G., Dal Forno, M., Danailov, M. B., De Monte, R., De Ninno, G., Delgiusto, P., Demidovich, A., Di Mitri, S., Diviacco, B., Fabris, A., Fabris, R., Fawley, W., Ferianis, M., Ferrari, E., Ferry, S., Froehlich, L., Furlan, P., Gaio, G., Gelmetti, F., Giannessi, L., Giannini, M., Gobessi, R., Ivanov, R., Karantzoulis, E., Lonza, M., Lutman, A., Mahieu, B., Milloch, M., Milton, S. V., Musardo, M., Nikolov, I., Noe, S., Parmigiani, F., Penco, G., Petronio, M., Pivetta, L., Predonzani, M., Rossi, F., Rumiz, L., Salom, A., Scafuri, C., Serpico, C., Sigalotti, P., Spampinati, S., Spezzani, C., Svandrlik, M., Svetina, C., Tazzari, S., Trovo, M., Umer, R., Vascotto, A., Veronese, M., Visintini, R., Zaccaria, M., Zangrando, D., and Zangrando, M. (2012). Highly coherent and stable pulses from the fermi seeded free-electron laser in the extreme ultraviolet. *Nat Photon*, 6(10):699–704. 2.1.1

Als-Nielsen, J., Freund, A., Wulff, M., Hanfland, M., and HÃ¤usermann, D. (1994). Performance of diamond as x-ray monochromator under very high heat flux in a

synchrotron beam. *Nuclear Instruments and Methods in Physics Research Section B: Beam Interactions with Materials and Atoms*, 94(3):348 – 350. 1

Altarelli, M., Brinkmann, R., Chergui, M., Decking, W., Dobson, B., Düsterer, S., Grübel, G., Graeff, W., Graafsma, H., Hajdu, J., et al. (2007). The technical design report of the european xfel. Technical report, European XFEL GmbH. 4.2

Amann, J., Berg, W., Blank, V., Decker, F.-J., Ding, Y., Emma, P., Feng, Y., Frisch, J., Fritz, D., Hastings, J., Huang, Z., Krzywinski, J., Lindberg, R., Loos, H., Lutman, A., Nuhn, H.-D., Ratner, D., Rzepiela, J., Shu, D., Shvydko, Y., Spampinati, S., Stoupin, S., Terentyev, S., Trakhtenberg, E., Walz, D., Welch, J., Wu, J., Zholents, A., and Zhu, D. (2012). Demonstration of self-seeding in a hard-x-ray free-electron laser. *Nat Photon*, 6(10):693–698. 2.1.2

Ashcroft, N. and Mermin, D. (2005a). *Festkörperphysik*. Oldenbourg Wissenschaftsverlag. 3.2, 3.4.1

Ashcroft, N. and Mermin, D. (2005b). *Waermeleitfaehigkeit eines Metalls*, pages 25–30. Oldenbourg Wissenschaftsverlag. 3.4.3.2

Authier, A. (2001). *Dynamical Theory of X-ray Diffraction*. IUCr Crystallographic Symposia Series. Oxford University Press. 1.2.1, 4.3.4

Ayvazyan, V., Baboi, N., BÃ¤hr, J., Balandin, V., Beutner, B., Brandt I., A., Bohnet, I., Bolzmann, A., Brinkmann, R., Brovko, O., Carneiro, J.-P., Casalbuoni, S., Castellano, M., Castro, P., Catani, L., Chiadroni, E., Choroba, S., Cianchi, A., Delsim-Hashemi, H., and Zapfe, K. (2005). First operation of a free-electron laser generating gw power radiation at 32 nm wavelength. 37:297. 1

Berman, R. (1992). Thermal conductivity of isotopically enriched diamonds. *Phys. Rev. B*, 45:5726–5728. 3.4.2

Borland, M. (2004). *User's Manual for elegant*. Advanced Photon Source. 4.1.2

Cahill, D. G., Goodson, K., and Majumdar, A. (2002). Thermometry and thermal transport in micro/nanoscale solid-state devices and structures. *Journal of Heat Transfer*, 124(2):223–241. 3.4.3.2, 5.1

Carminati, R., Volz, S., Chantrenne, P., Dilhaire, S., Gomez, S., Trannoy, N., and Tessier, G. (2006a). *Investigation of Short-Time Heat Transfer Effects by an Optical Pump-Probe Method*, pages 333–359. Springer Berlin Heidelberg. 3.3

Carminati, R., Volz, S., Chantrenne, P., Dilhaire, S., Gomez, S., Trannoy, N., and Tessier, G. (2006b). *Microscale and Nanoscale Heat Transfer*. Topics in Applied Physics. Springer Berlin Heidelberg. 3.4.3.1

Casimir, H. (1938). Note on the conduction of heat in crystals. *Physica*, 5(6):495 – 500. 3.4.3.2

Cattaneo, C. (1958). A form of heat conduction equation which eliminates the paradox of instantaneous propagation. *Compte Rendus*, 247(4):431–433. 3.4.3.1, 5.3.1, 5.3.1

Chin, A. H., Schoenlein, R. W., Glover, T. E., Balling, P., Leemans, W. P., and Shank, C. V. (1999). Ultrafast structural dynamics in insb probed by time-resolved x-ray diffraction. *Phys. Rev. Lett.*, 83:336–339. 3.1.1

Chou, F.-C., Lukes, J., Liang, X.-G., Takahashi, K., and Tien, C.-L. (1999). Molecular dynamics in microscale thermophysical engineering. *Annual Review of Heat Transfer*, 10(10). 3

Colella, R. and Luccio, A. (1984). Proposal for a free electron laser in the x-ray region. *AIP Conference Proceedings*, 118(1):179–188. 2.1.3

Curbis, F., Allaria, E., Danailov, M., De Ninno, G., Diviacco, B., Marsi, M., Trovò, M., Coreno, M., Günster, S., and Ristau, D. (2005). Operation of the european fel at elettra below 190 nm: A tunable laser source for vuv spectroscopy. In *Free Electron Laser Conference*, pages 473–475. 2.1.3

Deacon, D. A. G., Elias, L. R., Madey, J. M. J., Ramian, G. J., Schwettman, H. A., and Smith, T. I. (1977). First operation of a free-electron laser. *Phys. Rev. Lett.*, 38:892–894. 2

Decking, W. and Weise, H. (2017). Commissioning of the european xfel accelerator. 2.1.3

Element Six (accessed Nov. 2017). *THE ELEMENT SIX CVD DIAMOND HANDBOOK*. Element Six Technologies. https://e6cvd.com/media/wysiwyg/pdf/E6_CVD_Diamond_Handbook_A5_v10X.pdf. 5.4, 5.4.1, 5.7, 5.4.2, 5.9

Emma, P., Akre, R., Arthur, J., Bionta, R., Bostedt, C., Bozek, J., Brachmann, A., Bucksbaum, P., Coffee, R., Decker, F.-J., Ding, Y., Dowell, D., Edstrom, S., Fisher, A., Frisch, J., Gilevich, S., Hastings, J., Hays, G., Hering, P., Huang, Z., Iverson, R., Loos, H., Messerschmidt, M., Miahnahri, A., Moeller, S., Nuhn, H.-D., Pile, G., Ratner, D., Rzepiela, J., Schultz, D., Smith, T., Stefan, P., Tompkins, H., Turner, J.,

Welch, J., White, W., Wu, J., Yocky, G., and Galayda, J. (2010). First lasing and operation of an angstrom-wavelength free-electron laser. *Nat Photon*, 4(9):641–647. 1, 2.1.2

Flik, M. I. and Tien, C. L. (1990). Size effect on the thermal conductivity. of high-f thin-film superconductors. *Journal of Heat Transfer*, 112(4):872–881. 3.4.3.2, 33

Graebner, J. E. (1995). *Thermal Conductivity of Diamond*, pages 285–318. Springer US, Boston, MA. 3.9

Huang, Z. and Kim, K.-J. (2007). Review of x-ray free-electron laser theory. *Phys. Rev. ST Accel. Beams*, 10:034801. 2.2.2, 2.2.3

Jaeschke, E., Khan, S., Schneider, J., and Hastings, J. (2015). *Synchrotron Light Sources and Free-Electron Lasers: Accelerator Physics, Instrumentation and Science Applications*. Springer International Publishing. 4.1.1

Joseph, D. D. and Preziosi, L. (1989). Heat waves. *Rev. Mod. Phys.*, 61:41–73. 3.4.3.1

Joshi, A. A. and Majumdar, A. (1993). Transient ballistic and diffusive phonon heat transport in thin films. *Journal of Applied Physics*, 74(1):31–39. 3.4.3.1

Käding, O. W., Skurk, H., Maznev, A. A., and Matthias, E. (1995). Transient thermal gratings at surfaces for thermal characterization of bulk materials and thin films. *Applied Physics A*, 61(3):253–261. 3.4.3.2

Kaviany, M. (2014a). *Absorbtion of Ultrasound Waves in Solids*, pages 275–276. Cambridge University Press. 3.3

Kaviany, M. (2014b). *Debye and Other Phonon DOS Models*, pages 184–186. Cambridge University Press. 3.4.1

Khan, R. U. A., Martineau, P. M., Cann, B. L., Newton, M. E., and Twitchen, D. J. (2009). Charge transfer effects, thermoÂ and photochromism in single crystal cvd synthetic diamond. *Journal of Physics: Condensed Matter*, 21(36):364214. 5.3

Kim, K.-J., Shvyd'ko, Y., and Reiche, S. (2008). A proposal for an x-ray free-electron laser oscillator with an energy-recovery linac. *Phys. Rev. Lett.*, 100:244802. 1.1, 2.1.3

Kim, K.-J. and Shvyd'ko, Y. V. (2009). Tunable optical cavity for an x-ray free-electron-laser oscillator. *Physical Review Special Topics-Accelerators and Beams*, 12(3):030703. 1.2

Kittel, C. (2004). *Introduction to Solid State Physics*. Wiley. 1.2.1, 3.4.1, 3.4.2, 3.4.3.1

Klitsner, T., VanCleve, J., Fischer, H. E., and Pohl, R. (1988). Phonon radiative heat transfer and surface scattering. *Physical Review B*, 38(11):7576. 3

Kojima, S., Liu, K.-Y., Kudo, Y., Kawado, S., Ishikawa, T., and Matsushita, T. (1994). Time-resolved x-ray diffraction measurement of silicon surface during laser irradiation under grazing-incidence conditions. *Japanese Journal of Applied Physics*, 33(10R):5612. 3.1.1

Kondratenko, A. and Saldin, E. (1980). Generating of coherent radiation by a relativistic electron beam in an ondulator. *Part. Accel.*, 10:207–216. 1

Konorova, E. A., Kozlov, S. F., and Vavilov, V. S. (1966). Ionization currents in diamonds during irradiation with 500 - 1000 key electrons. *Sov. Phys. - Solid State*, 8(1). 3.1

Kozak, M., Trojanek, F., and Maly, P. (2015). Hot-carrier transport in diamond controlled by femtosecond laser pulses. *New Journal of Physics*, 17(5):053027. 3.1.1

Leo, W. R. (2012). *Techniques for nuclear and particle physics experiments: a how-to approach*. Springer Science & Business Media. 3.1

Li, H.-T., Jia, Q.-K., Zhang, S.-C., Wang, L., and Yang, Y.-L. (2017). Design of felichem, the first infrared free-electron laser user facility in china. *Chinese Physics C*, 41(1):018102. 2.1.3

Lindberg, R. R., Kim, K.-J., Shvyd'ko, Y., and Fawley, W. M. (2011). Performance of the x-ray free-electron laser oscillator with crystal cavity. *Phys. Rev. ST Accel. Beams*, 14:010701. 1.1

Lindenberg, A. M., Kang, I., Johnson, S. L., Missalla, T., Heimann, P. A., Chang, Z., Larsson, J., Bucksbaum, P. H., Kapteyn, H. C., Padmore, H. A., Lee, R. W., Wark, J. S., and Falcone, R. W. (2000). Time-resolved x-ray diffraction from coherent phonons during a laser-induced phase transition. *Phys. Rev. Lett.*, 84:111–114. 39

Maag, C., Zemella, J., and Rossbach, J. (2012). Electron optics and magnetic chicane for matching an xfel-oscillator cavity into a beamline at the european xfel laboratory. In *Proceedings of the 34th International Free Electron Laser Conference*. 4

Maag, C., Zemella, J., and Rossbach, J. (2015). Numerical studies of the influence of the electron bunch arrival time jitter on the gain process of an xfel-oscillator for the

european xfel. In *Proceedings of the 37th International Free Electron Laser Conference*. 3, 4

Maassen, J. and Lundstrom, M. (2014). Steady-state heat transport: Ballistic-to-diffusive with fourier's law. *Journal of Applied Physics*, 117(3):035104. 3.4.3.2, 3.4.3.2

Maassen, J. and Lundstrom, M. (2015). A simple boltzmann transport equation for ballistic to diffusive transient heat transport. *Journal of Applied Physics*, 117(13):135102. 3.4.3.2, 3.4.3.2, 5, 5.3.1

Maassen, J. and Lundstrom, M. (2016). Modeling ballistic effects in frequency-dependent transient thermal transport using diffusion equations. *Journal of Applied Physics*, 119(9):095102. 3.4.3.2, 3.4.3.2, 5

Madey, J. M. J. (1971). Stimulated emission of bremsstrahlung in a periodic magnetic field. *Journal of Applied Physics*, 42(5):1906–1913. 1, 2, 2.2.2

Madey, J. M. J. (1979). Relationship between mean radiated energy, mean squared radiated energy and spontaneous power spectrum in a power series expansion of the equations of motion in a free-electron laser. *Il Nuovo Cimento B (1971-1996)*, 50(1):64–88. 2.2.2

Majumdar, A. (1993). Microscale heat conduction in dielectric thin films. *Journal of Heat Transfer*, 115(1):7–16. 3.4, 3.4.3.1, 3.4.3.2, 33, 3.4.3.2

Majumdar, A. (1998). Microscale energy transport in solids. *Microscale Energy Transport*, pages 1–94. 2

Maldovan, M. (2012). Transition between ballistic and diffusive heat transport regimes in silicon materials. *Applied Physics Letters*, 101(11):113110. 3.4.3.2

Martellucci, S. and Chester, A. (1983). *Free electron lasers*. Ettore Majorana international science series: Physical sciences. Plenum Press. 2.2.2

Matsuda, O., Larciprete, M. C., Voti, R. L., and Wright, O. B. (2015). Fundamentals of picosecond laser ultrasonics. *Ultrasonics*, 56:3 – 20. 21, 3.3

McGaughey, A. J. H., Landry, E. S., Sellan, D. P., and Amon, C. H. (2011). Size-dependent model for thin film and nanowire thermal conductivity. *Applied Physics Letters*, 99(13):131904. 33, 3.4.3.2

Minnich, A. J., Johnson, J. A., Schmidt, A. J., Esfarjani, K., Dresselhaus, M. S., Nelson, K. A., and Chen, G. (2011). Thermal conductivity spectroscopy technique to measure phonon mean free paths. *Phys. Rev. Lett.*, 107:095901. 3.4.2, 3.4.3.2

Murphy, J. B. and Wang, X. (2008). Laser-seeded free-electron lasers at the nsls. *Synchrotron Radiation News*, 21(1):41–44. 2.1.1

Regner, K. T., McGaughey, A. J. H., and Malen, J. A. (2014). Analytical interpretation of nondiffusive phonon transport in thermoreflectance thermal conductivity measurements. *Phys. Rev. B*, 90:064302. 3.4.3.2

Reiche, S. (2004). *User's Manual for GENESIS 1.3*. http://genesis.web.psi.ch/download/documentation/genesis_manual.pdf. 4.2

Reis, D. A., DeCamp, M. F., Bucksbaum, P. H., Clarke, R., Dufresne, E., Hertlein, M., Merlin, R., Falcone, R., Kapteyn, H., Murnane, M. M., Larsson, J., Missalla, T., and Wark, J. S. (2001). Probing impulsive strain propagation with x-ray pulses. *Phys. Rev. Lett.*, 86:3072–3075. 39

Rhew, J.-H. and Lundstrom, M. S. (2002). Drift-diffusion equation for ballistic transport in nanoscale metal-oxide-semiconductor field effect transistors. *Journal of Applied Physics*, 92(9):5196–5202. 3.4.3.2

Schmueser, P., Dohlus, M., Rossbach, J., and Behrens, C. (2014). *Free-Electron Lasers in the Ultraviolet and X-Ray Regime: Physical Principles, Experimental Results, Technical Realization*. Springer Tracts in Modern Physics. Springer International Publishing. 2.2.1, 2.2.3, 2.2.3

Schulz, S., Grguraš, I., Behrens, C., Bromberger, H., Costello, J., Czwalinna, M., Felber, M., Hoffmann, M., Ilchen, M., Liu, H., et al. (2015). Femtosecond all-optical synchronization of an x-ray free-electron laser. *Nature communications*, 6. 4.2

Sellan, D. P., Turney, J. E., McGaughey, A. J. H., and Amon, C. H. (2010). Cross-plane phonon transport in thin films. *Journal of Applied Physics*, 108(11):113524. 3.4.3.2

Shin, T., Teitelbaum, S. W., Wolfson, J., Kandyla, M., and Nelson, K. A. (2015). Extended two-temperature model for ultrafast thermal response of band gap materials upon impulsive optical excitation. *The Journal of Chemical Physics*, 143(19):194705. 3.1.1

Shvyd'ko, Y. (2004). *X-Ray Optics: High-Energy-Resolution Applications*. Optical Sciences. Springer. 1.2.1

Shvyd'ko, Y., Stoupin, S., Blank, V., and Terentyev, S. (2011). Near-100 percent bragg reflectivity of x-rays. *Nat Photon*, 5(9):539–542. 1, 2.1.3

Sinn, H. (2007). Heat load estimates for xfel beamline optics. HASYLAB Annual Report 2007. 1.1

Sokolowski-Tinten, K. and von der Linde, D. (2004). Ultrafast phase transitions and lattice dynamics probed using laser-produced x-ray pulses. *Journal of Physics: Condensed Matter*, 16(49):R1517. 20

Stein, J., Shankland, T. J., and Nitsan, U. (1981). Radiative thermal conductivity in obsidian and estimates of heat transfer in magma bodies. *Journal of Geophysical Research: Solid Earth*, 86(B5):3684–3688. 3.4

Stepanov, S. A. (accessed Oct. 2017). *GID_SL on the Web*. http://sergey.gmca.aps.anl.gov/GID_sl.html. 4.3.1

Stepanov, S. A., Kondrashkina, E. A., Köhler, R., Novikov, D. V., Materlik, G., and Durbin, S. M. (1998). Dynamical x-ray diffraction of multilayers and superlattices: Recursion matrix extension to grazing angles. *Phys. Rev. B*, 57:4829–4841. 4.3, 4.3.1

Stoupin, S., Lenkszus, F., Laird, R., Goetze, K., Kim, K.-J., and Shvyd'ko, Y. (2010). Nanoradian angular stabilization of x-ray optical components. *Review of Scientific Instruments*, 81(5):055108. 3

Stoupin, S., March, A. M., Wen, H., Walko, D. A., Li, Y., Dufresne, E. M., Stepanov, S. A., Kim, K.-J., Shvyd'ko, Y. V., Blank, V. D., and Terentyev, S. A. (2012). Direct observation of dynamics of thermal expansion using pump-probe high-energy-resolution x-ray diffraction. *Phys. Rev. B*, 86:054301. 4, 3.1.1

Stoupin, S. and Shvyd'ko, Y. V. (2011). Ultraprecise studies of the thermal expansion coefficient of diamond using backscattering x-ray diffraction. *Phys. Rev. B*, 83:104102. 1.1, 3.2

Tamura, S.-i., Tanaka, Y., and Maris, H. J. (1999). Phonon group velocity and thermal conduction in superlattices. *Physical Review B*, 60(4):2627. 3

Telichko, A., Sorokin, B., and Kvashnin, G. (2015). Uhf acoustic attenuation and quality parameter limits in the diamond based hbar. In *2015 Joint Conference of the IEEE International Frequency Control Symposium the European Frequency and Time Forum*, pages 94–99. 3.4

Thomsen, C., Grahn, H. T., Maris, H. J., and Tauc, J. (1986). Surface generation and detection of phonons by picosecond light pulses. *Phys. Rev. B*, 34:4129–4138. 4, 3.3, 21, 5.1.1, 5.3

Van der Wiel, M. J. and Van Amersfoort, P. W. (1993). Felix: from laser to user facility. *Nuclear Instruments and Methods in Physics Research Section A: Accelerators, Spectrometers, Detectors and Associated Equipment*, 331(1):ABS30–ABS33. 2.1.3

Wei, L., Kuo, P. K., Thomas, R. L., Anthony, T. R., and Banholzer, W. F. (1993). Thermal conductivity of isotopically modified single crystal diamond. *Phys. Rev. Lett.*, 70:3764–3767. 3.4.2

Wiedemann, H. (2007). *Particle accelerator physics; 3rd ed.* Springer, Berlin. 2.2.1, 4.1.2, 4.1.2

Wiedemann, S. (2017). privare communication. Element Six synthetic industrial diamonds. 5.4.1, 5.7, 5.4.2, 5.9

Wille, K. (1992). *Physik der Teilchenbeschleuniger und Synchrotronstrahlungsquellen: Eine Einführung.* Teubner Verlag. 2.1, 2.2.1, 2.2.2

Wilson, R. and Cahill, D. G. (2014). Anisotropic failure of fourier theory in time-domain thermoreflectance experiments. *Nature communications*, 5. 3.4.3.2, 3.4.3.2, 37, 3.12, 5, 5.1

Wilson, R. and Cahill, D. G. (2015). Limits to fourier theory in high thermal conductivity single crystals. *Applied Physics Letters*, 107(20):203112. 3.4.2, 3.4.3.2, 3.4.3.2, 5

Wilson, R. B., Feser, J. P., Hohensee, G. T., and Cahill, D. G. (2013). Two-channel model for nonequilibrium thermal transport in pump-probe experiments. *Phys. Rev. B*, 88:144305. 5.1

Woodruff, T. O. and Ehrenreich, H. (1961). Absorption of sound in insulators. *Phys. Rev.*, 123:1553–1559. 3.3

Yilbas, B. and Al-Aqeeli, N. (2004). Thermal stresses due to time exponentially decaying laser pulse: elasto-plastic wave propagations. *International Journal of Mechanical Sciences*, 46(1):57 – 80. 5.3.1

Yilbas, B., Al-Dweik, A., and Mansour, S. B. (2011). Analytical solution of hyperbolic heat conduction equation in relation to laser short-pulse heating. *Physica B: Condensed Matter*, 406(8):1550 – 1555. 31, 3.4.3.1, 5.3.1

Zemella, J. (2013). *Untersuchungen zu einem Freie-Elektronen-Laser-Oszillator im Röntgen-Wellenlaengenbereich für den European XFEL*. Dissertation, University of Hamburg. 1.2, 1.2, 1.3, 2.2, 4.2.1, 4.3.1

Zemella, J., Novikov, D., Tolkiehn, M., Rossbach, J., and Sinn, H. (2011). Study of a silicon based xfelo for the european xfel. In *Proceedings of the 33th International Free Electron Laser Conference*, volume 11. 1.1

Zemella, J., Rossbach, J., Maag, C., Sinn, H., and Tolkiehn, M. (2012). Numerical simulations of an xfelo for the european xfel driven by a spent beam. In *Proceedings of the 34th International Free Electron Laser Conference*. 1.1, 3, 4.1.2, 4.3, 4.3.4, 5.5

Zhang, Y. (2007). Nano/microscale heat transfer. 33

Ziaja, B., Medvedev, N., Tkachenko, V., Maltezopoulos, T., and Wurth, W. (2015). Time-resolved observation of band-gap shrinking and electron-latticethermalization within x-ray excited gallium arsenide. *Scientific Reports*, 5:18068–. 3.1, 3.1

Ziman, J. (1960a). *Size and Surface Effects*, pages 451–482. International series of monographs on physics. OUP Oxford. 3.4.3.2

Ziman, J. (1960b). *Thermal conduction in insulators*, pages 288–292. International series of monographs on physics. OUP Oxford. 3.4.2

Eidesstattliche Versicherung / Declaration on oath

Hiermit versichere ich an Eides statt, die vorliegende Dissertationsschrift selbst verfasst und keine anderen als die angegebenen Hilfsmittel und Quellen benutzt zu haben.

Die eingereichte schriftliche Fassung entspricht der auf dem elektronischen Speichermedium.

Die Dissertation wurde in der vorgelegten oder einer ähnlichen Form nicht schon einmal in einem früheren Promotionsverfahren angenommen oder als ungenügend beurteilt.

Hamburg, den 6. August 2018

Christoph Maag